Long-term analysis of aerodynamic effects within a real-scale CSP heliostat field

Master Thesis

at Hof University

Engineering Department

Master Mechanical Engineering

Submitted to

Prof. Dr. Tobias Plessing

Alfons-Goppel-Platz 1

95028 Hof

Germany

Submitted by

Laura Paulus

Calle Manuel Gongora 3

04007 Almeria

Spain

Hof, 1st May 2024

Master Thesis

for the award of the academic degree
Master of Engineering (M.Eng.)

Date of Issue	1st December 2023
Date of Submission:	1st May 2024
Author:	Laura Paulus
Degree Programme:	Master Mechanical Engineering (M.Eng.)
University:	University of Applied Sciences Alfons-Goppel-Platz 1 95028 Hof Germany
Conducted at:	German Aerospace Center (DLR) Institute of Solar Research Calle Doctor Carracido 42 04005 Almeria Spain
Advisor:	Dr. Rer. Nat. Natalie Hanrieder
First Examiner:	Prof. Dr. Ing. Tobias Plessing
Second Examiner:	Prof. Dr. Rer. Nat. Robert Honke

Declaration of Authenticity

I hereby certify that I have written this thesis independently and without the use of any sources other than those stated. To the best of my knowledge, it does not contain any material previously published or written by another person where due reference is not made in the text. The ideas taken directly or indirectly from external sources are labelled as such and the respective origin is cited. This also applies to graphic representations as well as drawings and sketches.

I certify that, to the best of my knowledge and belief, this thesis has not been previously submitted in the same or a similar form to any other examining authority for an academic degree or diploma; and that it furthermore has not yet been published.

Almeria, May 1st, 2024

place and date

L. Paulus

signature

Abstract

This master thesis presents a comprehensive analysis of wind speed measurements in a heliostat field of a concentrating solar tower power plant. The measurement campaign utilized high-resolution ultrasonic anemometers installed in three different heights above ground (4 m, 7 m and 10 m) at four wind masts mounted at different locations outside and inside the CESA-1 heliostat field of CIEMATs' Plataforma Solar de Almería (Spain) over three and a half months between February 15th and May 31st 2023. The study evaluates wind speed, direction, gust as well as turbulence intensity and turbulence spectra. Additionally, two dimensional wind data acquired with two LiDAR scanners for the complete heliostat field is compared with the anemometer data. Data preprocessing and validation are conducted to ensure data quality for the analysis. Further, the surface area of each heliostat within the field dependent on the orientation of the heliostat perpendicular to the wind is derived using self-designed Matlab algorithms. Consecutively, the impact of the heliostat orientation on wind pattern within the heliostat field can be analysed.

It can be found, that the average wind speed and gust decreased inside the heliostat field in comparison to measurements outside of the field. The turbulence intensity increased inside the heliostat field. The effect is more pronounced in 4 m height than in 7 m height. This can be explained as the base height of the heliostats is around 4 m in stow position (aligned horizontally) and the heliostats' upper edge is in around 7 m when they are aligned vertically. Therefore, the effect of the heliostat orientation on wind pattern is more pronounced in 7 m height. It can also be seen that the outer heliostat rows have a more pronounced effect on wind pattern than the inner rows.

Comparisons between anemometer and LiDAR data show good agreement at the specific locations of the wind masts. The two dimensional LiDAR data enables an understanding of wind flow dynamics within the heliostat field and identifying wind shadow effects from nearby structures outside of the heliostat field. Overall, this study provides valuable insights into aerodynamic effects within concentrate heliostat fields. The results of this thesis contribute to an optimization of heliostat designs to tackle investment cost savings in solar tower power plants.

Kurzzusammenfassung

Die vorliegende Masterarbeit präsentiert eine umfassende Analyse der Windgeschwindigkeitsmessungen in einem Heliostatenfeld eines konzentrierenden Solarturmkraftwerks. Für die Messkampagne werden hochaufgelöste Ultraschallanemometer verwendet, die in drei verschiedenen Höhen über dem Boden (4 m, 7 m und 10 m) an vier Windmasten außerhalb und innerhalb des Heliostatenfeldes CESA-1 der Plataforma Solar de Almería (Spanien) über dreieinhalb Monate zwischen dem 15. Februar und dem 31. Mai 2023 angebracht waren. Im Rahmen der Studie werden Windgeschwindigkeit, -richtung, -böen sowie Turbulenzintensität und Turbulenzspektren ausgewertet. Zusätzlich werden zweidimensionale Winddaten, die mit zwei LiDAR-Scannern für das gesamte Heliostatenfeld erfasst wurden, mit den Anemometerdaten verglichen. Die Daten werden vorverarbeitet und validiert, um die Datenqualität für die Analyse sicherzustellen. Außerdem wird die Fläche jedes Heliostaten innerhalb des Feldes in Abhängigkeit von der Ausrichtung des Heliostaten senkrecht zum Wind mithilfe selbst entwickelter Matlab-Algorithmen abgeleitet. Anschließend kann der Einfluss der Heliostatenausrichtung auf das Windmuster innerhalb des Heliostatenfeldes analysiert werden.

Es kann festgestellt werden, dass die durchschnittliche Windgeschwindigkeit und die Böen innerhalb des Heliostatenfeldes im Vergleich zu Messungen außerhalb des Feldes abnehmen. Die Turbulenzintensität nimmt innerhalb des Heliostatenfeldes zu. Der Effekt ist in 4 m Höhe stärker ausgeprägt als in 7 m Höhe. Dies lässt sich dadurch erklären, dass die Basishöhe der Heliostaten in Ruheposition (horizontal ausgerichtet) etwa 4 m beträgt, während die Oberkante der Heliostaten bei vertikaler Ausrichtung etwa 7 m beträgt. Daher ist die Auswirkung der Heliostatenausrichtung auf das Windmuster in 7 m Höhe stärker ausgeprägt. Es ist zudem zu erkennen, dass die äußeren Heliostatenreihen einen stärkeren Einfluss auf das Windmuster haben als die inneren Reihen.

Vergleiche zwischen Anemometer- und LiDAR-Daten zeigen eine gute Übereinstimmung an den spezifischen Standorten der Windmasten. Die zweidimensionalen LiDAR-Daten ermöglichen ein Verständnis der Windströmungsdynamik innerhalb des Heliostatenfeldes und die Identifizierung von Windschatteneffekten durch nahe gelegene Strukturen außerhalb des Heliostatenfeldes. Insgesamt liefert diese Studie wertvolle Erkenntnisse über aerodynamische Effekte innerhalb von CSP-Heliostatenfeldern. Die Ergebnisse dieser Arbeit tragen zur Optimierung von Heliostatendesigns bei, um Investitionskosteneinsparungen bei Solarturmkraftwerken zu realisieren.

Contents

List of Symbols and Abbreviations

Table 0.1: List of characters, symbols and indices used for calculations in this thesis.

Abbreviation	Explanation	Unit
α	Azimuth	°
β	Wind direction	°
ε	Elevation	°
κ	von Kármán constant (0.4)	[–]
Υ	Impact of heliostats on wind pattern	$\%m^{-2}$
ρ	Air density	kgm^{-3}
σ	Standard Deviation	
τ_0	Wall Shear Stress	
abs	absolute	
av	average	
azi	Azimuth	[–]
c	speed of light	ms^{-1}
c_p	phase velocity	ms^{-1}
ele	Elevation	[–]
F	Force	$kgms^{-2}$
f	Frequency	Hz
f_0	Frequency emitted by LiDAR signal	Hz
f_Q	Vector of frequencies corresponding to the PSD vector	Hz
F_S	Sampling Rate	Hz
FFT	Fast Fourier Transformation	
i	Number of Timestamps	[–]
I	Turbulence Intensity	%
j	Number of Heliostats	[–]
k	Number of Data Points	[–]
MA / ma	Moving Average	
m_i	Innermost Windmast	[–]
m_o	Outermost Windmast	[–]
NBS	Number of Samples per Block	[–]
NFFT	Number of Bins for FFT	[–]
N_S	Number of Samples	[–]
Q	Input Signal Vector for PSD	
r^i	Innermost Heliostat Row	[–]
r^o	Outermost Heliostat Row	[–]
ref	reference	
S_Q	Power Spectral Density Vector	$m^2s^{-2}Hz^{-1}$

Table 0.1: List of characters, symbols and indices used for calculations in this thesis.

Abbreviation	**Explanation**	**Unit**
sca	Scalar	
t	Time	s
$TA_{\%}$	Target Area as Percentage of mirror surface	%
TA_B	Basic Target Area of a heliostat without mirrors	m^2
TA_{ML}	Basic Target Area of a heliostat without mirrors	m^2
TA_{total}	Target Area as Absolute mirror surface	m^2
T_f	Block Length	s
u	Horizontal wind component N–S	ms^{-1}
u_r	Radial velocity	ms^{-1}
u_τ	Friction velocity	ms^{-1}
U	Wind speed	ms^{-1}
v	Horizontal wind component E–W	ms^{-1}
vec	Vectorial	
w	Vertical wind component	ms^{-1}
z	Reference Height	m
z_0	Roughness Height	m

Table 0.2: List of abbreviations used in this thesis.

Abbreviation	**Explanation**	**Unit**
2D	Two dimensional	
3D	Three dimensional	
ABL	Atmospheric Boundary Layer	
AMSL	Above Mean Sea Level	m
CIEMAT	Centro de Investigationes Energéticas, Medioambientales y Tecnológicas (Center for Energy, Environmental Studies and Technology)	
CSP	Concentrated Solar Power	
CST	Concentrating Solar Technologies	
CT	Central Tower	
DLR	Deutsches Zentrum für Luft- und Raumfahrt (German Aerospace Center)	
DNI	Direct Normal Irraciance	
DOE	Department of Energy	
E	East	°
G	Wind Gust	ms^{-1}
GP	Grid Point	

Table 0.2: List of abbreviations used in this thesis.

Abbreviation	**Explanation**	**Unit**
HR	Heliostat Row	
ICAO	International Civil Aviation Organization	
IEA	Inernational Energy Agency	
IRENA	Inernational Renewable Energy Agency	
ISO	International Organization for Standardization	
LCOE	Levelized Cost of Electricity	$\$kW^{-1}h^{-1}$
LiDAR	Light (Imaging) Detection and Ranging	
LOS	Line Of Sight	
MAD	Mean Absolute Deviation	
ML	Measurement Line	
N	North	°
NBS	Number of Samples per Block	
NFFT	Number of Bins for FFT	
PPI	Plan Position Indicator	
PSA	CIEMATs' Plataforma Solar de Almeria	
PSD	Power Spectral Density	
PSF	Probability Density Function	
PV	Photovoltaik	
RMSE	Root Mean Square Error	
S	South	°
SSL	Standard Sea Level (20°, 1 atm)	
STP	Solar Tower Power Plant	
TA	Target Area	
TES	Thermal Energy Storage	
W	West	°
WM	Wind Master	
WMO	World Meteorological Organization	
WS	Wind Sonic	

1 Introduction

The subject of this master thesis is the investigation of the long-term aerodynamic effects in a concentrated solar power system. In particular, the thesis deals with the assessment of the heliostats' influence based on experimental wind data taking into consideration local wind conditions. The first chapter of this thesis will present an overview of the study's background and its significance within the global energy market context. The introduction will culminate by outlining the research's purpose and the specific objectives it seeks to achieve.

1.1 Motivation

Mitigating global climate change requires collaborative efforts on a global scale. Utilizing energy from a variety of renewable sources is essential to maximize the efficient use of natural resources. According to IRENA 2019, solar and wind could together account for 60 % of the provided electricity by the year 2050 [1].
However, grid stability and demand-oriented supply might be challenged by the supplied energy provided by Photovoltaik (PV) and wind energy due to its natural fluctuations. Concentrating Solar Technology (CST) can be used to compensate for some of these shortcomings because heat is generated by concentrating mirrors which can be converted directly into electrical energy or it can be stored e.g. in tanks of molten salt. Areas with ample sunlight and favourable geographic features can economically benefit from solar thermal energy. Continuous technological progress in this sector shows promise for its seamless integration into the broader energy infrastructure. [2–4]

The critical determinant in technology adoption often revolves around cost considerations, particularly evident in the substantial cost declines observed in solar PV systems. These declines are attributed to ongoing technological advancements and economies of scale, leading to a faster rate of cost reduction compared to solar thermal systems. [5]
Despite variations in location and resource availability impacting the Levelized Cost of Electricity (LCOE) for renewable energy systems, utility-scale PV plants achieved an LCOE of 6 USD cents/kWh in 2020 as reported by the U.S. Department of Energy (DOE). In contrast, concentrating solar power (CSP) plant LCOEs decreased from 21 USD cents/kWh in 2010 to 10.3 USD cents/kWh in 2020, achieved through the integration of thermal energy storage systems with a minimum 12-hour capacity. [6, 7]

CSP plants offer advantages in supplying dispatchable electricity from intermittent solar sources via thermal storage systems, more cost-efficient than electrical storage alternatives. Future targets aim for LCOEs of 3 cents/kWh for utility PV and 5 cents/kWh for CSP by 2030, necessitating significant technological strides for CSP goals. Research focuses on engineering solutions to enhance system efficiency through higher operation temperatures exceeding 700°C, defining the concept of third-generation CSP plants [8, 9]. Promising technologies like solar power

towers undergo rigorous testing by various research entities and companies to identify optimal materials for these applications. [10]

1.2 State of the Art

As stated previously, heliostats represent with 30 – 50 % a significant portion of the overall capital costs of solar tower power plants [6]. It is therefore advisable to research for possible cost saving factors in the heliostat design.
Researchers have extensively investigated the effects of wind loads on heliostats through various methods. These investigations have predominantly relied on wind tunnel experiments using scaled-down models to replicate real conditions. [11–13] Furthermore, some studies have shifted focus towards examining single full-scale heliostats to better understand their response to wind loads. [14, 15] Additionally, researchers have explored the efficacy of utilizing heliostats as wind fences to reduce wind loads within the heliostat field, yielding positive results. [15, 16]

Peterka et al. initiated this line of inquiry by testing the hypothesis using a scaled 1:60 model of a heliostat field within a wind tunnel. Their work laid the groundwork for further investigations into the practical implications of wind load reduction by the outer heliostats. [13]

Building upon Peterka et al.'s research, Sment et al. conducted full-scale investigations to assess the wind load on heliostats in real-world conditions. Their study marked the first time such measurements were performed on a full-scale heliostat field. To characterize incoming wind conditions, Sment et al. strategically placed anemometers outside the field at different heights (4 m, 7 m, and 10 m) and utilized an array of anemometers positioned among and on the heliostats within the field. [17]
The results from Sment et al.'s investigation are promising, indicating a significant decrease in wind load on the first five rows of heliostats due to the reduced wind speeds within the heliostat field. [17]
However, Sment et al.'s study also revealed several limitations that warrant consideration. Firstly, the measurement data was limited to only four hours, which may not fully capture the variability of wind conditions over time. Secondly, measurements were taken only up to row 5 of the heliostat field, representing the outer edge rather than the middle, where wind effects may differ. Lastly, the use of only a single wind mast moved successively between rows resulted in large time gaps between data sets, and the deceleration effects over multiple rows could not be simultaneously examined. [17]

Addressing these limitations in future research provides a more comprehensive understanding of wind load dynamics within heliostat fields. Long-term measurement campaigns, expanded spatial coverage within the field, and improved methodologies for wind measurement can contribute to more accurate assessments and informed design decisions, ultimately enhancing the efficiency and cost-effectiveness of heliostats.

1.3 Objective of the Thesis

In addition to the potential cost savings resulting from efficiency improvements, another promising strategy involves optimizing the design of heliostats. The heliostat field constitutes a significant portion of the capital cost of a power tower plant, estimated at approximately 30 % (IRENA, 2021) to 50 % (Mancini, 2000) [18, 19]. According to Jones and Singhai, this high share of the overall costs of a SPT plant is mainly caused by the heliostat steel support structure [20, 21]. Sandia National Laboratories' cost reduction report confirms these findings and identifies drive and control systems, along with heliostat support structures, as main cost drivers, with azimuth drives often being overbuilt. [22]

To address this challenge and further reduce the LCOE of solar power tower plants, the AdaptedHelio project, funded by the German Federal Ministry for Economic Affairs and Climate Action in 2021, has been initiated. It is coordinated by the German Aerospace Center (DLR) in collaboration with partners sbp Sonne GmbH, Fraunhofer Institute for Energy Economics and Energy System Technology (Fraunhofer IEE) and the Spanish Center for Energy, Environmental Studies and Technology (CIEMAT).
The primary objective of this project is to identify cost-saving potential through a wind-optimized heliostat design. The field measurements conducted at CIEMATs' CESA-1 solar tower power (STP) plant at the Plataforma Solar de Almería (PSA) in Spain are object of this master thesis. Two measurement campaigns have been planned to gain insights into the wind conditions within and above the heliostat field. The main objective of this research is to capture the wind effects across the heliostat field using multiple temporally high-resolution anemometers within the field as well as two spatially high-resolution LiDAR scanners positioned outside the field.

The assumption is that the outer rows of heliostats will sufficiently slow down the wind across the field, leading to lower wind speeds and reduced wind loads for the inner heliostats. If this hypothesis is confirmed by the measurement campaign, the results can help to optimize the structural design to decrease heliostat field costs.

2 Theoretical and Mathematical Foundations

The subject of this work is a computer-aided analysis of large quantities of wind measurement data using mathematical methods. This chapter covers the essential theory and mathematics required for this thesis, providing a solid foundation for the subsequent evaluation, analysis and discussion. It introduces concentrated solar power systems and the measurement sensor equipment used for the measurement campaign. Furthermore, technical terminology used in the context of the thesis is defined and the mathematical background is given.

2.1 Importance of Wind in Concentrated Solar Power (CSP)

The chapter initiates by elaborating on the influence of wind on concentrated solar power systems. It begins with an overview of concentrated solar power, emphasizing solar tower power (STP) plants. Additionally, heliostats and their role in STP systems are explained.

2.1.1 Concentrated Solar Power (CSP)

CST, also equivalently called CSP, is a renewable energy technology that converts radiation into heat and electricity. The basic principal of CSP systems is visualized on the example of a STP plant in figure 2.1.

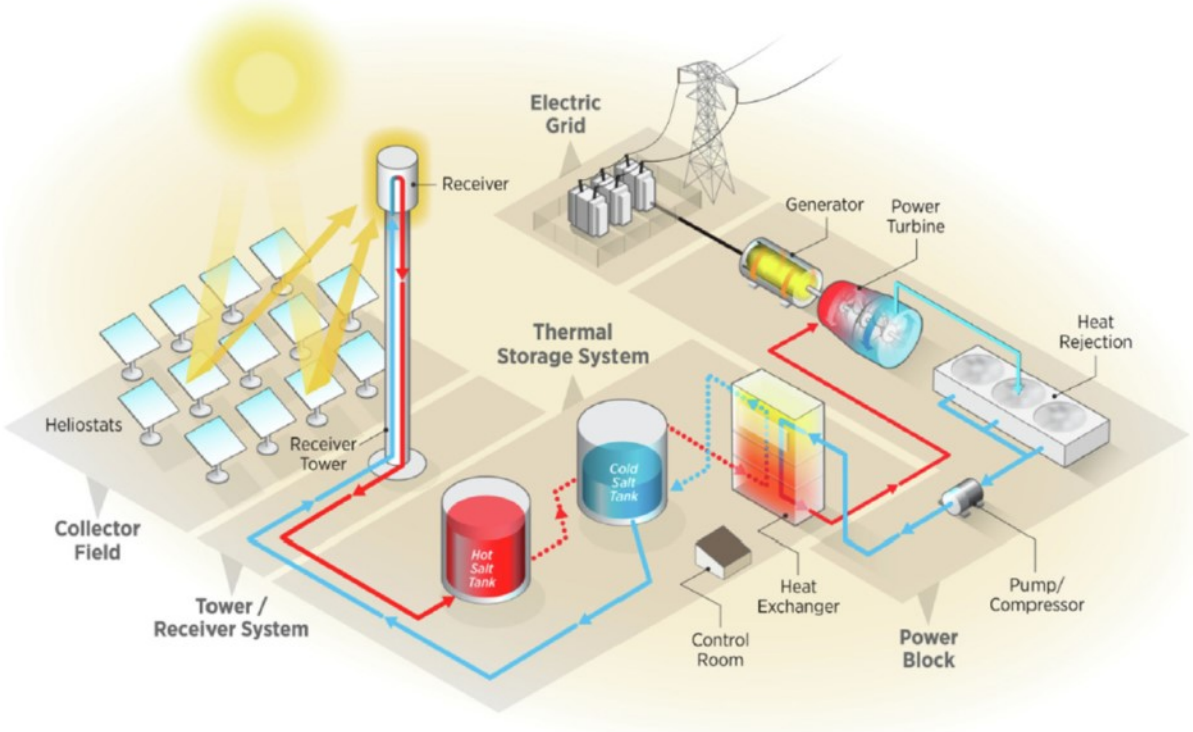

Fig. 2.1: Illustration depicting the fundamental operational principles of concentrated solar power on the example of a solar tower power plant. [5]

As described by Ding and Bauer, CSP plants consist of four major blocks - the collector field, the tower/receiver system , the thermal storage system and a power generation system (compare fig. 2.1) [8]. In the collector field, mirrors or lenses are used to concentrate sunlight onto a small area, typically a receiver, to generate high temperatures. In a second step, this concentrated light is used as a heat source for a power plant. A heat transfer fluid (molten salt, oil or water) is heated to produce steam which can then drive a turbine connected to a generator that converts the mechanical energy to electrical energy. [6, 8]

Concentrating solar technologies can be sorted into four different categories as shown in figure 2.2, each with unique designs and applications.

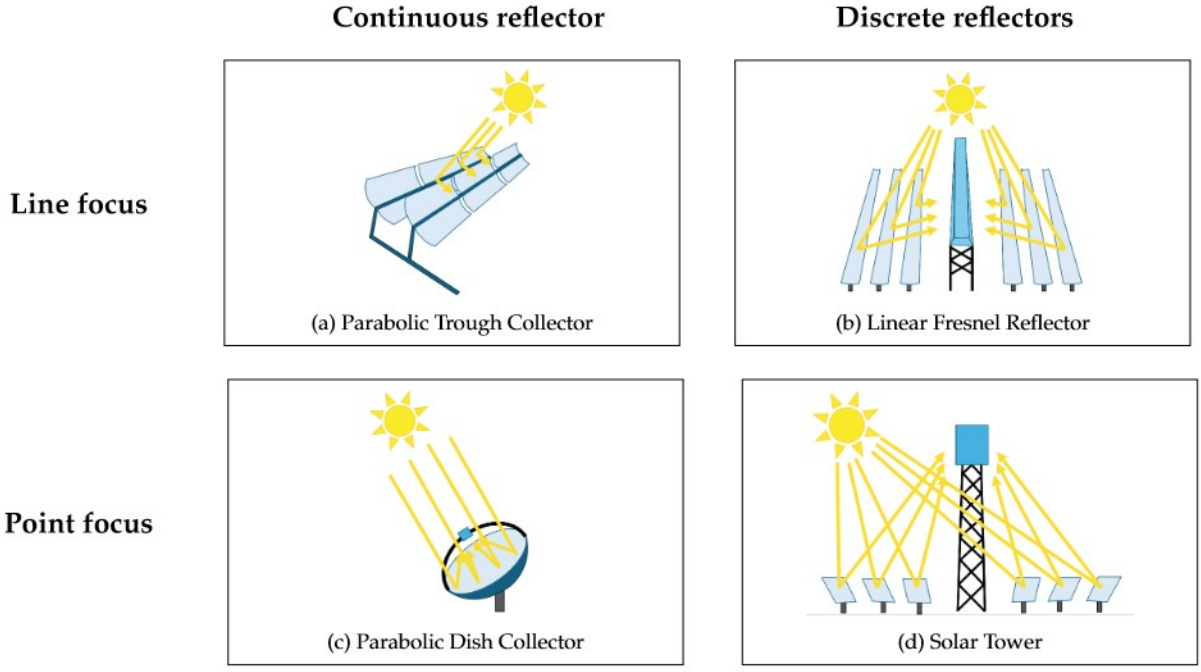

Fig. 2.2: Different types of CSP systems and their categorizations. Scheme adapted from [23].

Parabolic troughs (fig. 2.2a) and linear fresnel (fig. 2.2b) CSP systems concentrate the solar rays onto a linear receiver tube, whereas parabolic dishes (fig. 2.2c) and solar tower plants (fig. 2.2d) focus the rays onto a single point. Further, CSP systems can be distinguished between continuous reflectors, where there is only one reflector focusing sun light towards the receiver (fig. 2.2, left), and discrete reflectors, where several single reflectors are used to concentrate the light (fig. 2.2, right). [23–25]

Line focusing systems track the sun in one rotation axis, while point focusing collectors track the sun in two axes. Two-axes tracking enables higher concentration rates and therefore increased temperatures at the receiver can be achieved. [6, 23]

The potential of integrated thermal storage capacity, the third main block that is shown in figure 2.1, is one main advantage of CSP technology. It enables the provision of electricity

dependent on the actual energy demand and also during cloudy conditions or nighttime. [26] The so-called *Duck Curve* shown in figure 2.3 illustrates the aforementioned typical daily discrepancy between solar power generation and standard load demand. It visualises the imbalance between total electrical demand regardless of supply source and net load (load actually required to be supplied – system load minus load served by utility-scale variable generated from available renewable energy sources) throughout a 24-hour period [27]. [28]

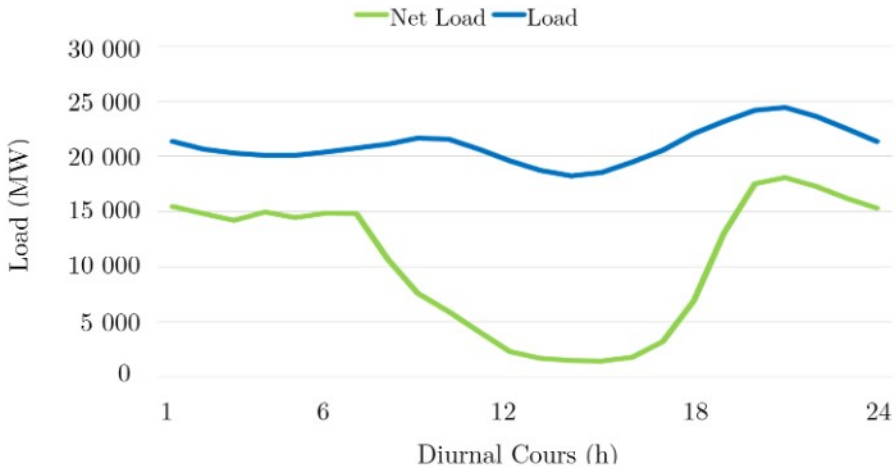

Fig. 2.3: Typical Duck Curve illustrating the Total and the Net Load over the course of a day. The graph shows data provided by California ISO for April 24th, 2021. [29]

By incorporating thermal energy storage (TES), CST can help level out the energy net load long-term. Achkari has found that integrating a TES system in a CSP plant increases the power plant's capacity factor by more than 20 % and decreases the LCOE by around 6 % by increasing electricity production [7]. Alami et al. showed that hybrid PV/Wind/CSP using TES is a practical alternative with a high capacity factor and a low LCOE, which makes it a competitive choice for nations like Jordan that have higher DNI and GHI values. Yang et al. on the other hand promote the possibilities of combining CSP systems with an electrolyzer for hydrogen production to be used as an energy storage system [30]. [26]

According to Jabari, CSP is also considered as one of the most viable options for a sustainable supply of the energy demanded by desalination systems, especially in conjunction with thermal energy storage systems [31]. This aspect is also promoted by the International Energy Agency (IEA) and International Renewable Energy Agency (IRENA) who stated that the CSP could be implemented in different high-temperature water desalination applications in arid countries [32].

CSP also faces some challenges, including high investment costs as well as land and water requirements. The latter is e. g. due to the necessity to clean the concentrating mirrors, especially in rather dry areas with only few precipitation events per year, which are in many cases well suited for the implementation of CSP systems due to generally high irradiation levels. Still,

concentrating solar technology has the potential to play a significant role in the ongoing green energy transition. It can complement other renewable energy sources such as photovoltaic and wind energy, particularly in situations requiring high temperatures. This makes it an essential component in moving towards a sustainable energy future. [6, 33]

2.1.2 Solar Tower Power Plants

In terms of spatial extent, STP plants – also commonly referred to as central tower (CT) plants – are typically the largest of four different types of CSP systems [24, 26]. They consist of a field of hundreds of mirrors, called heliostats, that are positioned in a semicircle or circle around a tower [34]. Figure 2.4 shows a picture of a typical STP plant on the example of the CESA-I power plant at the PSA, owned by the Spanish research institution CIEMAT. On the right side of the picture, the heliostat field can be seen with the heliostats orientated towards the solar tower on the left side of the picture.

Fig. 2.4: Aerial view of the CESA-I power plant located at CIEMATs' Plataforma Solar de Almeria in the South of Spain. [35]

Depending on the facilities location and capacity, the heliostats can be spread over several kilometres around the tower and focus the direct normal irradiance (DNI) throughout the day and year onto a focal point at the receiver on top of the tower. The receiver itself consists of absorber panels or tubes. These tubes are irradiated by the concentrated sunlight and absorb the incoming energy as heat, which is then transferred to the heat transfer fluid as described previously (comp. fig. 2.1). [26, 36] Alternatively, also a combination of several smaller towers and heliostat fields, so-called multi-tower solutions, can be implemented. [37].

The key advantage of the tower plant design is the possibility of its larger scale and design-based efficiency. The flux onto the receiver can be around four to six times higher than the

incoming flux at the heliostats which comes with a higher concentration ratio compared to line focusing systems and consequently higher working temperatures of the heat transfer fluid. Therefore, an increased thermodynamic efficiency as well as thermal energy storage efficiency can be achieved with solar tower plants. This leads to higher electrical output with the same system size and thus to lower costs. [6, 36, 38] Although central tower plants require more infrastructure and expenditure than other CSP technologies, under the right conditions they offer therefore some distinct advantages compared to parabolic CSP systems.

There is ongoing discussion about the ideal dimensions and designs, and there are several chances for optimization that will affect the technology's total impact and cost. These include advancements in solar receiver technology to improve heat absorption and thermal efficiency, development of innovative heat transfer fluids to enhance energy transfer and storage capabilities, optimization of heliostat design and tracking systems for improved sunlight concentration and accuracy, exploration of novel materials for tower construction to withstand high temperatures and minimize thermal losses, and refinement of control and automation systems to optimize plant operation and maintenance. [9, 36, 39] The here evaluated measurement campaign focuses on wind loads within the heliostat field which can be considered to reduce the investment costs of solar tower plants.

2.1.3 Role of Heliostats in concentrating solar power

There have been three distinct stages in the development of heliostat technology thus far. The first heliostats were typically $40\,m^2$ in size and constructed of laminated glass. The main alteration in the second generation was an increase in size ($44 - 57\,m^2$). The objective was to reduce the cost of components required for every heliostat, independent of size, in order to lower the cost per unit collection area (control mechanisms, structural support, etc.). A few fundamental criteria and guidelines were also proposed during this time to set limits on the functionality, longevity, and survivability of individual components. The recommended lifetime of thirty years has persisted as the norm. The state of the art technology currently in use, the third generation, brings considerably larger sizes (typically over $100\,m^2$) along with a wider range of research, including numerous new designs as well as much smaller heliostats ($< 1\,m^2$) [40]. [6, 36]

The two different heliostat designs which are mounted within CIEMATs' CESA-1 heliostat field vary between 2x6 and 4x6 panels. However, as could be shown by Wu, the difference of the wind load for both heliostat designs is small compared with the overall wind load on the heliostat structure and are therefore neglected for this thesis [41]. Figure 2.5 shows a sketch of a heliostat in use within CIEMATs' CESA-1 heliostat field with all relevant dimensions. All values depicted in the figure have been provided by CIEMAT and are listed in table 2.3.

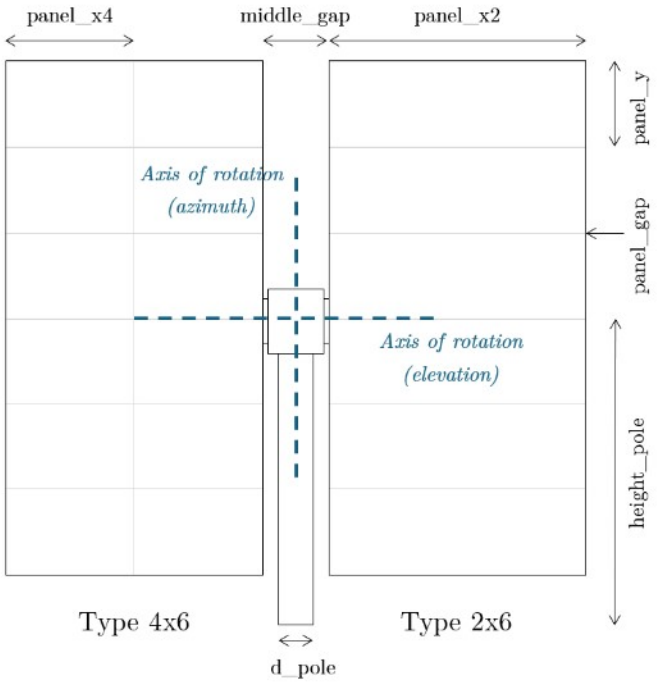

Fig. 2.5: Sketch of a typical heliostat as used at the CESA-I field. All relevant values depicted have been provided by CIEMAT and are listed in table 2.3.

Table 2.3: Relevant values of the heliostats in use at PSA's CESA-I field. Abbreviations refer to figure 2.5.

Parameter	Value	Unit
number of Facets	12 / 6	–
panel_x4	1.50	m
panel_x2	3.00	m
panel_y	1.00	m
height_pole	3.60	m
d_pole	0.40	m
middle_gap	0.75	m
panel_gap	0.01	m

Tracking of Heliostats

Each single heliostat within the field is tracked in two axis to optimally concentrate the DNI onto the central receiver at the top of the solar tower. The azimuth-elevation tracking method involves one axis of rotation pointing vertically towards the zenith (azimuth α), while the other axis is tangential to the heliostat surface (elevation ϵ). This creates rotation and tilting of each heliostat as seen from a bystander's reference frame, as shown in figure 2.6. [42]

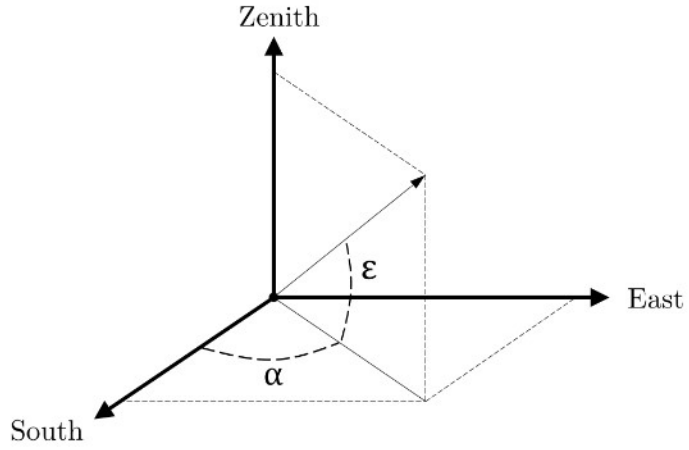

Fig. 2.6: Definition of the heliostats' tracking status by elevation (ϵ) and azimuth (α) angle.

In the following evaluation, the azimuth α is defined as 0° for the heliostat facing East, 90° for the heliostat facing South and 180° when the heliostat faces West. The elevation ϵ of the heliostat is defined as 0° for the heliostat facing down (stow position), 90° for the heliostat standing vertical above the ground and 180° when the heliostat faces upwards.

Wind load influence on heliostat design

Wind exerts a profound influence on heliostat design, necessitating robust engineering solutions to mitigate its effects on optical accuracy, structural integrity, and overall system performance. High wind speeds can induce dynamic loads on heliostat structures, leading to deflection, misalignment, and degradation of optical performance [19]. Consequently, heliostat designs must incorporate aerodynamic considerations, such as wind load analysis, structural reinforcement, and control mechanisms, to ensure reliable and accurate solar tracking under varying wind conditions. [19–21]
Several researches about wind load on heliostats have been conducted in the past, strengthening the idea of a potential costs reduction by optimizing the heliostat design in regards to individual wind conditions. Further information can be found in chapter 1.2.

2.2 Basic Definitions and Mathematical Background

The upcoming chapter lays the theoretical groundwork essential for understanding the concepts discussed in this thesis. It covers fundamental definitions along with an outline of the mathematical principles that form the basis of this work.

2.2.1 Wind speed

The wind speed U is defined as the velocity of horizontal displacement of the air particles, which is determined by measuring instruments [43]. Wind speed can be represented as a three-dimensional vector consisting of horizontal-longitudinal, horizontal-lateral, and vertical components, denoted as $\overrightarrow{u}$, $\overrightarrow{v}$, and $\overrightarrow{w}$, or simply u, v, and w respectively, as shown in figure 2.7.

The wind speed components are typically measured in meters per second (ms^{-1}), aligning with recommendations from the World Meteorological Organization and the International Civil Aviation Organization (ICAO) [43, 44]. The measurement techniques employed in this study for ascertaining wind speed are elaborated in chapter 2.3. For more comprehensive insights into the experimental setup, please refer to the corresponding chapter 3.1.

U refers in this evaluation to the two-dimensional horizontal wind speed parallel to the ground, calculated in accordance with equation 1

$$U = \sqrt{u^2 + v^2}. \tag{1}$$

2.2.2 Wind direction

The wind direction β is defined as the direction from where the wind blows. It is given in degrees from 0 to 360 measured clockwise from the geographical north. As such the wind direction is defined as $0°$ for the wind coming from the north. [43] The wind components u and v cover the horizontal plane with the wind directions $South \rightarrow North$ and $East \rightarrow West$, respectively. Wind component w is defined as upwards in its positive orientation. The relations between wind direction and cardinal directions can be seen in the following figure 2.7, also incorporating the coordinate system of the wind components.

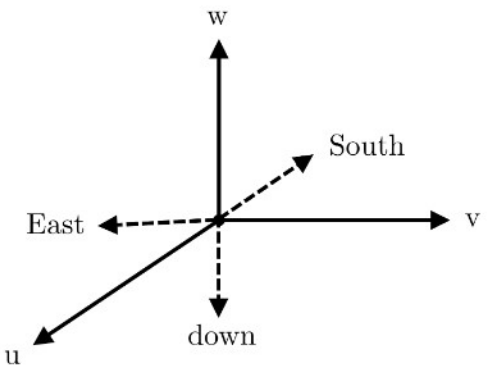

Fig. 2.7: Definition of the three dimensional wind components in regards to the cardinal directions.

The wind direction can be calculated by using the four-quadrant inverse tangent, $\arctan2(y, x)$ [45–47]. This has the distinct advantage of solving the wind angle in a single equation without the

need of case distinctions depending on the respective wind components and thus gaining the unique wind vector value located in all four quadrants [45, 48]. With the coordinate systems defined in this thesis, the wind speed is calculated from the wind components in regard to the individual coordinate systems as follows.

$$\beta = \arctan 2\,(-v, u)\,. \tag{2}$$

2.2.3 Wind Gust

Wind gusts G are defined as the maximum observed wind speed over a specified time interval. In accordance with the WMO, the moving average wind speed over three seconds has been calculated and the maximum of these moving averages represents the wind gust of the time interval. [43]

2.2.4 Turbulence Intensity

The turbulence intensity I describes the wind turbulence. It is a dimensionless parameter used to describe the fluctuation of a turbulent wind flow. It can be calculated the individual wind components u, v and w as

$$I_u(z) = \frac{\sigma_u}{U_{av}}, \qquad I_v(z) = \frac{\sigma_u}{U_{av}} \qquad \text{and} \quad I_w(z) = \frac{\sigma_u}{U_{av}}, \tag{3}$$

with x pertaining to the respective wind component, where U_av is the 10-minute averaged wind speed U and σ_U is the standard deviation, given by

$$\sigma_u = \sqrt{\frac{1}{N_S - 1} \sum_{i=1}^{N_S} (U_i + U)^2}. \tag{4}$$

with N_S being the number of data points and U_i the individual wind speed at each timestamp of the averaged time interval [43, 49]. Analogously, the turbulence intensity can also be calculated for the horizontal wind speed

$$I_U(z) = \frac{\sigma_U}{U_{av}} \tag{5}$$

Unless otherwise stated, I_U is referred to when discussing turbulence intensity I.

Variations of the turbulence intensity can be caused by a large number of influences, including but not limited to the surrounding terrain and obstacles in the way of the wind to either cause

turbulences or shelter from them. Typical values for turbulence intensity range from 8 % at the open sea, over about 13 % at flat and open grass land up to over 20 % at complex terrain. As a rule, the higher turbulence intensities occur at lower wind speeds. [43, 49]

2.2.5 Wind Speed Profile over Height and Roughness Heigh

The wind speed profile over height describes the variation of wind speed with height above the ground or a reference surface. These profiles are influenced by factors such as terrain roughness, surface features, and atmospheric conditions. Wind movement near the earth's surface experiences frictional forces that slow it down. This effect diminishes with height until it becomes insignificant at a height known as the gradient height, typically around 1000 m or about 10 % of the troposphere's height. This region below the gradient height is called the atmospheric boundary layer (ABL), and it consists of sublayers including the surface layer and a transition region. [50, 51]

The surface layer, extending up to approximately 100 m, maintains a relatively constant shearing stress and wind direction with height. Prandtl's logarithmic wind profile equation is often used to describe the wind velocity profile ($U(z)$) in this layer

$$U(z) = \frac{u_\tau}{\kappa} \ln\left(\frac{z}{z_0}\right), \tag{6}$$

where z is the height above the ground, z_0 is the roughness height, $\kappa = 0.4$ is the von Kármán constant and u_τ is the friction velocity defined by

$$u_\tau = \sqrt{\frac{\tau_0}{\rho}} \tag{7}$$

in which ρ is the air density and τ_0 is the wall shear stress. In the context of neutral stratification in the Prandtl layer, the friction velocity is considered neutral. As a result, the roughness height becomes the sole variable affecting the height profile in this scenario. [50, 51]

The roughness height (z_0) crucially depends on terrain roughness characteristics, impacting wind speeds and turbulence. Solar radiation, diurnal cycles, and seasonal variations further influence wind behaviour. [52]

Presuming constant standard deviations within the lower boundary layer, σ_u can be approximated for a homogeneous open terrain as [50, 52]

$$\sigma_u \approx 2.5 \cdot u_\tau, \qquad \sigma_u \approx 2.5 \cdot u_\tau \qquad \text{and} \quad \sigma_u \approx 2.5 \cdot u_\tau. \tag{8}$$

As such, the turbulence intensity can be approximated based on the roughness height by inferring the friction velocity u_τ from equation 6,

$$I = \frac{1}{\ln\left(\frac{z}{z_0}\right)} \tag{9}$$

or alternatively the roughness height (z_0) can be calculated from the turbulence intensity

$$z_0 = \frac{z}{\exp\left(\frac{1}{I}\right)}. \tag{10}$$

2.2.6 Turbulence Spectra

Turbulence spectra describe the statistical distribution of velocity fluctuations in the atmospheric boundary layer in correlation with individual frequencies of the turbulences. These spectra provide insights into how turbulence intensity varies with different frequencies within the flow field. Turbulence spectra are widely used in meteorology and atmospheric science to analyse and model turbulent flows, especially in studies related to wind energy, air pollution dispersion, and atmospheric dynamics. [50]

The calculation process entails performing a Fourier transform on the time series data, converting it from the time domain to the frequency domain. This transformation aids in segregating the diverse frequency components inherent in turbulence data, and the resultant frequency spectrum elucidates the energy distribution across varying frequencies within the turbulent flow. [53]
Different methods and algorithms can be used to process the data and calculate the turbulence spectra, such as the Fast Fourier Transform (FFT) algorithm. Additional, individual adjustments may be considered as needed.

Upon employing the FFT, the power spectral density (PSD) distribution S can be derived, which characterizes the frequency distribution based on the squared magnitudes of the Fourier coefficients. The integral of this distribution over the frequency domain equals the variance (squared standard deviation).

The computational implementation of the PSD calculation is detailed in chapter 3.3.4. Empirical approximations have been developed and documented in the literature to estimate the spectra of horizontal and vertical turbulence energy.[53, 54]. For the horizontal wind components u and v, Kaimal formulates the following set of normalized wind spectra [53]

$$\frac{fS_u(f)}{u_\tau^2} = \frac{200n}{(1+50n)^{\frac{5}{3}}} \tag{11}$$

$$\frac{fS_v(f)}{u_\tau^2} = \frac{15n}{(1+9.5n)^{\frac{5}{3}}} \tag{12}$$

with the friction velocity u_τ, f as the frequency in Hz and n as the non-dimensional frequency normalized by the height z and the horizontal wind speed U.

$$n = \frac{fz}{U} \tag{13}$$

Analogously, Panofsky provides the turbulence energy spectra for the vertical component w using the following approximation [54]

$$\frac{fS_w(f)}{u_\tau^2} = \frac{3.36n}{(1+10n)^{\frac{5}{3}}}. \tag{14}$$

2.2.7 Averaging

In this study, the averaging period is set at 10-minute intervals, a common practice also utilized in weather forecasting. The World Meteorological Organization (WMO) recommends this interval for wind data analysis. [43]
Shorter averaging periods, such as 1 minute, fail to adequately smooth the inherent turbulent fluctuations in wind patterns. They represent effectively extended gust periods rather than true averages. [43]

2.2.8 Vectorial and Scalar Calculation of Wind Data

Wind is a vector quantity encompassing both direction and magnitude (speed), yet it's common to analyze wind speed and direction separately as scalar quantities. Typically gathered at high frequencies, wind data is then averaged across varying time frames, from minutes to hours, with averaging methods including vector averaging, scalar averaging, or a blend of both approaches, depending on the instrumentation and intended application. [46]

For *scalar* calculation, calculations are performed using the raw data at the original captured measurement frequency and downsampled to the desired temporal resolution in a second step. For *vectorial* calculation, on the other hand, the data is first averaged to the desired temporal resolution. It was determined at the example of wind speed that both values differ only slightly from each other. With regard to processing time and computer performance, a vectorial calculation approach was used for the evaluation of the wind data in this thesis. [46]

2.3 Wind Measurement Sensor Equipment

In the context of this thesis, two different types of sensor equipment have been utilized to ascertain the wind conditions. Their measurement principles will be described in the following.

2.3.1 Ultrasonic Anemometers

Ultrasonic anemometers measure the wind speed components in two or three directions by the means of ultrasonic pulses of sound [14]. They work almost exclusively on the basis of the time-of-flight method with direct time determination, employing transmitter-receiver-pairs within the anemometer. An ultrasonic signal is emitted from one side along a measuring path and received again on the other side by using the piezoelectric and inverse piezoelectric effect, respectively. After that, a signal will also be transmitted (and received) in the opposite direction. Influenced by the wind, the signal reaches the receiver earlier in one direction than in the opposite direction. [55, 56]

At time step t_1, the transmitter emits an ultrasonic pulse with phase velocity c_p, which after a delay time Δt_1 has travelled the (fixed) distance Δx between the transmitter and receiver and is detected by the receiver. This transit time Δt_1 is the variable to be measured. [57] At the time t_1 one obtains

$$t_1 : \frac{\Delta x}{\Delta t_1} = c_p - u \tag{15}$$

Since the wind component u is opposite to the propagation direction of the pulse, the arrival of the pulse at the receiver is delayed in time. Afterwards (at t_2), the receiver itself becomes the transmitter and sends out a pulse in the opposite direction, which is received by the receiver, which was the transmitter in the previous time step. [57] This results for the time step t_2:

$$t_2 : \frac{\Delta x}{\Delta t_2} = c_p + u \tag{16}$$

By addition and subtraction of equations 15 and 16

$$(t_2 + t_1) : \frac{\Delta x}{\Delta t_2} + \frac{\Delta x}{\Delta t_1} = 2c_p \tag{17}$$

$$(t_2 - t_1) : \frac{\Delta x}{\Delta t_2} - \frac{\Delta x}{\Delta t_1} = 2u \tag{18}$$

it is shown that the wind component u can be deduced directly and independently from phase velocity c_p from equation 18. Finally, by combining two or three rotated transmitter/receiver pairs, the two dimensional horizontal wind vector or complete three-dimensional wind vector can be determined respectively. [56]

2.3.2 LiDAR Technology

LiDAR technology, an acronym for Light (Imaging) Detection and Ranging Technology, finds diverse applications in topographic mapping, urban planning, forestry management, and atmospheric research. By swiftly and precisely gauging distances through laser pulses, it has revolutionized surveying and monitoring techniques. It operates on the principle of measuring the frequency shift of scattered light by particles moving with flow velocity, using the Doppler effect to gauge velocity accurately. [58, 59]
LiDAR technology offers a non-intrusive and economical method for analysing wind patterns and turbulence in both terrestrial and atmospheric settings. Doppler LiDAR systems specifically allow accurate measurements of wind speed and direction, leading to progress in renewable energy evaluations, weather predictions, and climate modeling. [59]

The LiDAR measurement technology setup comprises two primary components: the transmitter and the receiver. The transmitter emits brief light pulses lasting from a few to several hundred nanoseconds, while the receiver includes a telescope for gathering backscattered photons. An intricate optical system within the receiver processes the return signal, converting it into an electrical signal. To minimize background radiation, an interference filter is typically positioned before the detector, allowing only the desired wavelength to pass through. [59, 60]

The LiDAR scanner determines distances using the time-of-flight principle [59]. In simplified terms, it measures the time taken for a laser beam to travel from the emitter to the receiver. Distance is then calculated using the fundamental formula of velocity, where velocity equals distance divided by time. [60]
While the time-of-flight principle calculates distances accurately, it doesn't directly provide wind speed data. To analyse wind speed, the Doppler effect comes into play. This effect gauges the wind speed of particles in the air by detecting the frequency shift resulting from their movement relative to the LiDAR scanner, as described by the following equation 19

$$f = f_0\left(1 + \frac{2u_r}{c}\right) \tag{19}$$

with f being the measured frequency of the returned signal, f_0 the frequency of the emitted signal, u_r the velocity of the particle and c the speed of light. [60]
By rearranging equation 19, the velocity can then be calculated according to equation 20

$$u_r = \frac{(f - f_0)}{2 \cdot f_0}. \tag{20}$$

However, the wind speed u_r derived from LiDAR measurements reflects the radial component along the laser's line-of-sight (LOS). This velocity accurately represents the true speed of an object only when it moves directly along the laser's propagation path. Consequently, it accounts for a fraction of the actual velocity u. Pauscher et al. demonstrated improved wind speed

accuracy by employing multiple LiDAR scanners focused on a single spatial point. Placing scanners at varied locations with distinct azimuth and elevation angles relative to incoming winds yields individual u_r equations per scanner. The resulting system of linear equations can then be analytically solved for wind speed determination. [61]

Performing plan position indicator (PPI) scans enables a higher measurement point density across a larger area of interest [58]. During PPI scans, the LiDAR beam remains fixed at a low elevation angle while sweeping across various azimuth angles. By combining the radial wind speed measurements obtained from these scans with data on wind direction from external sources like anemometers, the horizontal wind speed at each measurement point can be reconstructed (Wandinger, 2005). This technique is expanded upon by Pauscher et al. (2016), who demonstrate that employing multiple LiDAR scanners in PPI scans allows for the determination of wind speeds across a broader area. This method, known as Dual-Doppler LiDAR, typically involves two scanners to simplify the analytical solution by reducing the unknowns in the linear equation to two. [62, 63]

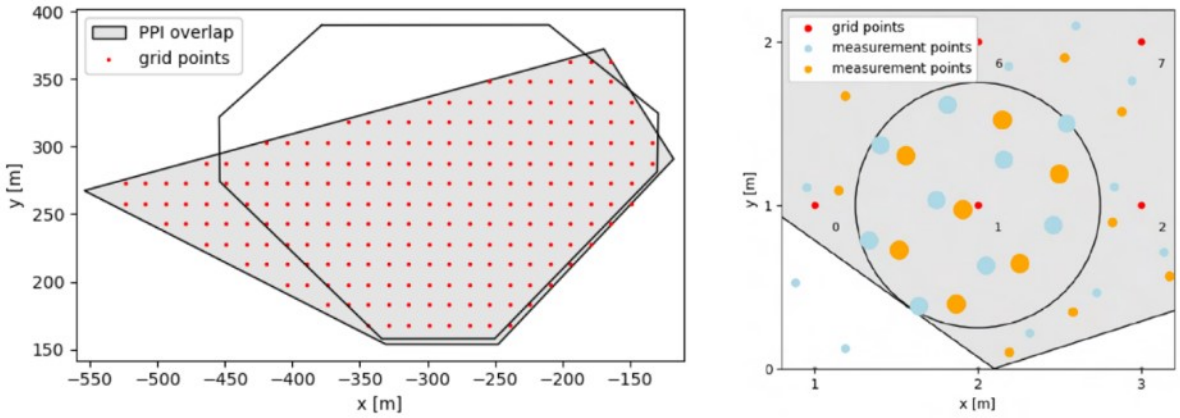

(a) (b)

Fig. 2.8: Scheme of the LiDAR measurement principle a) covering the whole field and b) showing a close up of one grid point and the underlying LiDAR measurement points. [64]

Figure 2.8 depicts the measurement principle employed by the LiDAR scanners. In Figure 2.8a, the shaded area represents the overlapping coverage of two LiDAR scanners. The approach involves assigning LiDAR measurement data to specific grid points (GPs), as illustrated by the red grid points in the figure. Figure 2.8b demonstrates how LiDAR data is allocated to each grid point by identifying the nearest neighbours among the data points.

3 Methodology

The here evaluated wind measuring campaign aims to enhance the understanding of wind load distribution across heliostat arrays through the utilization of advanced measurement techniques and data analysis methodologies.

One of the central focuses of the wind measurement campaign involves the utilization of temporally and spatially high-resolution wind data to investigate the intricate aerodynamic effects within heliostat arrays. This involves assessing the wind flow patterns and their impacts on heliostat performance across the field.
The scope of the wind measurement campaign encompasses several key phases:

1. **Deployment of Ultrasonic-Anemometer and Multi-LiDAR Measurements:** The primary objective of this phase is to gather raw wind data from a real-scale heliostat field. This involves the deployment of anemometer and multi-LiDAR systems to capture comprehensive wind measurements.

2. **Evaluation of Aerodynamic Conditions:** The next phase involves preprocessing and analysing the gathered data to assess the aerodynamic conditions within the heliostat field. This step is crucial in understanding the complex interplay between wind dynamics and heliostat performance.

3. **Interpretation of Results:** The final phase focuses on interpreting the analysed data, both independently and through comparative analysis of anemometer and multi-LiDAR measurements. This step aims to extract meaningful insights into the aerodynamic behaviour of the heliostat field.

By gaining a deeper understanding of aerodynamic dynamics, the measurement campaign aims to identify opportunities for improving heliostat performance and efficiency. In summary, the wind measurement campaign represents a concerted effort to advance scientific understanding of heliostat field aerodynamics, with the ultimate goal of enhancing design efficiency and cost-effectiveness in concentrated solar power applications.

The research entails conducting high time-resolution measurements of wind conditions within a real-scale heliostat field, utilizing ultrasonic anemometers strategically positioned at various locations within the field to capture point measurements of wind dynamics over an extended period. This approach facilitates a detailed examination of wind behaviour at specific points within the heliostat array.

Complementing the point measurements, the research employs an innovative multi-LiDAR method to investigate larger-scale flow conditions above the heliostat field. Spatially and temporally resolved measurements of wind conditions were conducted over several months, providing comprehensive insights into the broader wind dynamics impacting the entire field. This methodology enables a holistic understanding of wind patterns and their implications for

heliostat performance. The unique selling points of the wind measuring campaign are the long-term measurements which enable a detailed analysis of local wind conditions in a real-scale heliostat field.

The analysis of the wind loads on the heliostats is based on wind measurement data in the CIEMAT free field. These are very large amounts of data that have been processed, pre-processed and validated. The procedure and required mathematical principles are described below. The following chapter provides an overview of the methodology used during the research process and data interpretation. The experimental setup of the wind measurements is outlined, including a short description of the test site where the measurement campaign was carried out. Further, the methodology of the data processing is described.

3.1 Experimental Setup

This chapter introduces the analysed measurement campaign and test site. It also provides insights into the physical setup and apparatus deployed for data collection as outlined previously.

3.1.1 CESA-I at CIEMAT's Plataforma Solar de Almeria

In the context of the AdaptedHelio project, a measurement campaign was carried out at CIEMATs' *Plataforma Solar de Almeria* (PSA), located near Tabernas in the south of Spain [6] Today, the facility is Europe's largest centre for the research, development and testing of concentrating solar technology, owned by the Spanish Center for Energy, Environmental Studies and Technology (Sp.: *"Centro de Investigaciones Energeticas, Medioambientales y Tecnologicas"* – CIEMAT). [65]

The measurements were carried out at the CESA-I heliostat field. The CESA-I tower facility, that can be seen in fig. 3.1 on the left side, was built as a superheated steam system with a 1.2 MW two-stage turbine in a Rankin cycle. It is used as a test platform with the aim to decrease cost of critical components. With both first and second generation units as well as third generation facets and prototypes developed by CIEMAT and SOLUCAR, the CESA-I facility has the most extensive experience in glass-metal heliostats in the world. [66]

The direct solar radiation is collected by the 330 x 250 m south-facing field of 300 heliostats distributed in 16 rows. The heliostats have a nominal mean 90 % reflectivity, the solar tracking error on each axis is 1.2 mrad and the reflected beam image quality is 3 mrad. [66]

The maximum thermal power delivered by the field onto the receiver aperture is 7 MW at a typical design irradiance of 950 Wm^2, achieving a peak flux of 2.2 MWm^2. 99 % of the power is focused on a 4 m diameter circle and 90 % is in a 2.8 m circle. [66]

Fig. 3.1: Aerial view of CIEMAT's Plataforma Solar de Almeria including all its research facilities. On the left side, the CESA-I heliostat field, where the measurements were carried out, can be seen. Picture taken from Google Earth [67].

The 80 m high concrete tower, which has a 100 t load capacity, has four test levels. [6]

- At 80 m: A volumetric air receiver test facility at the top of the tower
- At 75 m: A multipurpose test facility for new receiver concepts
- At 60 m: A cavity with a calorimetry test bed for pressurized volumetric receivers
- At 45 m: A cavity adapted for use as a solar furnace for materials testing

3.1.2 Setup of the Ultrasonic-Anemometers

Nine anemometers have been strategically positioned along the axis of the prevailing south-west (SW) wind direction (fig. 3.2, bottom). These anemometers were affixed to four masts, three of which were situated within the field and one positioned outside (see fig. 3.2, top). Each of the wind masts 2, 3 and 4 featured a 2D anemometer (WindSonic, Gill Instruments, [68]) and a 3D anemometer (WindMaster, Gill Instruments, [69]) at heights of 4 meters and 7 meters, respectively, while wind mast 1, located in the south-west of the heliostat field also hosted

an additional 3D anemometer at a height of 10 meters above ground. The 2D anemometers provided east (u) and north (v) wind components at a 4 Hz frequency, while the 3D anemometers additionally captured the upward component (w) at a 20 Hz frequency. The locations of the masts are depicted in figure 3.2.

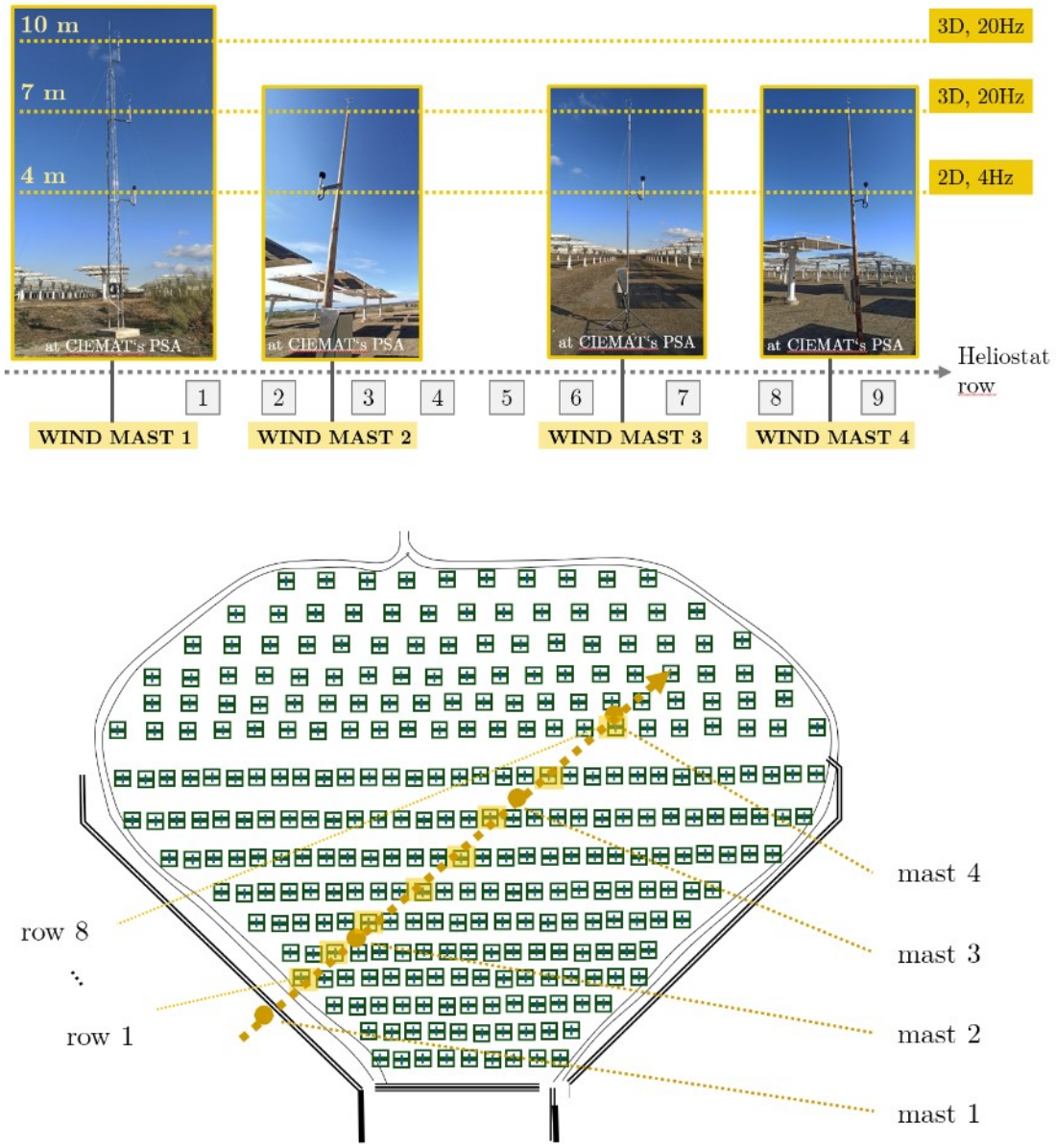

Fig. 3.2: Locations of the wind masts setup within the heliostat field. 2D anemometers are set up at a height of 4 m, 3D anemometers at 7 m at each wind mast. Additionally, a 3D anemometer is positioned at 10 m height at wind mast 1. The heliostats' rows are counted within the measurement line.

The positioning of the wind masts was determined depending on the prevailing wind direction at the test site. The prevailing winds at the site are predominantly from the south-west to the north-east. The wind masts were positioned accordingly in order to analyse a change in the wind as it enters the heliostat field. The heliostat row numbers were defined along the

measurement line for this analysis, as shown in fig. 3.2. Anemometers are positioned between rows, per this definition in row 0.5, 2.5, 6.5 and 8.5 for wind mast 1-4, respectively.

Using the provided data and the defined row numbering, the influence of the heliostat field on wind pattern dependent on the heliostat row can be derived. For a two-dimensional analysis of the wind field, two LiDAR scanners have been implemented and their setup will be detailed subsequently.

3.1.3 Setup of the LiDAR scanners

The Dual-Doppler measurement setup employed two WindCube 200s LiDAR scanners from Leosphere (now owned by Vaisala, [70]) to derive horizontal wind speeds by combining two PPI scans at low elevation angles. Scanner 1, positioned north-east atop a construction scaffold, and Scanner 2, located south-east on a building. A sketch of the positioning of both scanners in spacial relations to the heliostat field is shown in figure 3.3.

Both scanners cover an azimuth range of 42 degrees in a clockwise direction from the north and scan horizontally with an angular resolution of 1.5° per second, which leads to a rough radial resolution of 3 meters. Figure 3.3 illustrates the locations of both scanners and provides a rough outline of the scanned areas in spacial relation to heliostat field and wind masts.

Specifics such as height above sea level, beam elevation, and covered azimuth range are also recorded. They are provided in table 3.4 for reference.

Table 3.4: LiDAR Scanner elevation, beam elevation and azimuth range details per scanner [64].

	scanner elevation (AMSL)	beam elevation (°)	azimuth range (°)
scanner 1	513.0 ± 0.2	-0.27	$214 - 255$
scanner 2	508.3 ± 0.2	$+0.67$	$296 - 337$

The heliostat field is located on relatively flat terrain, ranging in elevation from 498.6 meters above sea level in the southern area to 501.3 meters in the northern region. To accommodate this height variation, Scanner 1 employs a negative elevation angle of $-0.27°$, while Scanner 2 conducts PPI scans with a positive elevation of 0.67°. However, uncertainties exist due to the lack of high-precision GPS for scanner elevation determination and the unverified accuracy of the provided heliostat field elevation profile.

The measurement points to derive the radial wind speed via the dual-doppler mode operation are spaced each 3 meters within the range of 100 to 625 meters distance from the LiDAR scanners, with range gates set at 25 meters. This arrangement yields a total of 7392 measurement points per PPI scan pass, calculated as 42 points horizontally by 176 points vertically.

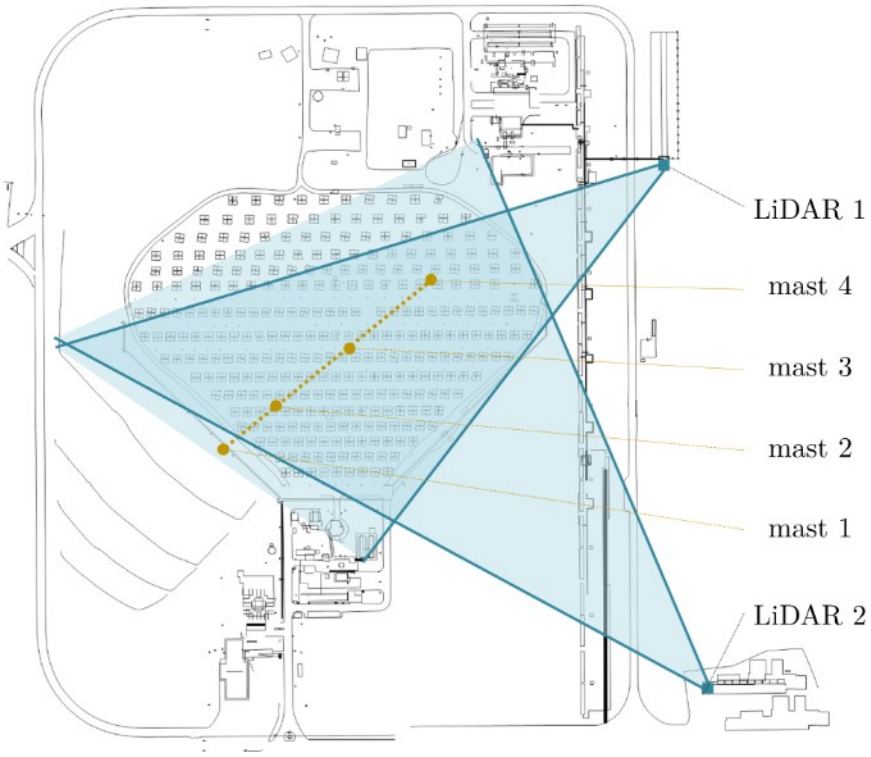

Fig. 3.3: Layout and locations of wind mast 1 – 4 and LiDAR scanners.

3.1.4 Data Aquisition

The wind masts with the anemometers measured continuously between December 2021 and June 2023. Issues arose with data acquisition from wind mast 3, though, resulting in several data gaps throughout the entire measurement campaign period. This issue also compromised the reliability of the data from wind mast 3 compared to the data collected from the other wind masts. In the following analysis, wind mast 3 has therefore been excluded from several evaluations.

The LiDAR scanners were operational between December 2022 and June 2023. Throughout this period, the scanners operated continuously, conducting uninterrupted PPI scans and synchronized Line-of-Sight (LOS) point scans.

However, necessary heliostat maintenance and dismounting of heliostat facets has been carried out until February 15th 2023. The evaluation of the measurement campaign was therefore restricted to the time interval between February 15th and May 31st 2023.

3.2 Data Preparation and Preprocessing

This section details the (pre-)processing of the acquired data. The anemometer data underwent processing using MATLAB versions R2022b and R2023a. Meanwhile, the LiDAR data pro-

cessing was entrusted to the project partner Fraunhofer IEE, who used Python programming language and provided the processed data to DLR. A short overview of the algorithms written in the context of this thesis is given in appendix A.

3.2.1 Anemometer Data

This chapter outlines essential steps necessary to ensure that the ultrasonic anemometer data is prepared for detailed analysis. These steps include the preparation of raw data for processing, which involves the extraction and conversion of wind components measured by anemometers into a usable format.

The raw data of the ultrasonic anemometers have been logged continuously during the measurement campaign by several CR1000X data loggers of Campbell Scientific in ASCII-format with a temporal resolution of 20 Hz for the 3D WindMaster and 4 Hz for the 2D WindSonic anemometers [71]. The anemometers measure the two (u, v) or three (u, v, w) wind components. The raw data have been downsampled to a 10 minutes temporal resolution as described in chapter 2.2 and stored in DLRs' data management SQL database. Further, several additional parameters have been derived from the raw data captured with the anemometers which are described in the following.

Calculation of the Wind Direction

The anemometer data was fully prepared before the commencement of this thesis, and a substantial portion of preprocessing had been completed, including the scalar calculation of wind data. However, during the original preprocessing, the wind direction was calculated wrongly, resulting in inaccuracies in the subsequent evaluation. Correcting this calculation error is a key objective of this thesis before the evaluation can be started.

This correction process faces two main challenges. Firstly, issues with the data from wind mast 3 necessitate manual correction of timestamps. In the case of a repeated downsampling, a new time correction would also be necessary, which is a labour- and time-intensive task.
Secondly, the processing time is a concern, as the repetitive downsampling procedure is time-consuming. With a needed processing time of up to six hours per wind component and 23 components overall (4x 2D anemometers and 5x 3D anemometers), re-calculating the scalar wind speed on the hardware provided would take at least several days if not weeks.
A proposed solution involves utilizing the already downsampled data from the initial preprocessing to correct the wind direction calculation. This correction entails a shift from scalar to vectorial calculation of wind direction. However, validation of this approach is imperative. A detailed analysis, to be discussed in the next section 3.4, will compare and assess the differences and influences between the scalar (β_{sca}) and vectorial (β_{vec}) calculations of wind direction.

The wind direction correction process initiates with determining the precise start and end times of the available data (from December 7th 2022 to June 2nd 2023). Following this, a custom routine is developed to systematically recalculate wind direction values for all anemometers across each mast. This involves retrieving relevant parameters per station from the SQL database, accurately computing wind direction using horizontal wind components u and v, substituting incorrect wind direction values within the comprehensive wind data structure, and subsequently saving all parameters in mat-files to maintain data format consistency.

Once the wind direction values are corrected, the updated mat-files are uploaded back into the SQL database for data integrity. To validate the accuracy of the wind direction calculations, a comparative analysis is performed against data from the HP wind mast, a measurement station from a separate project. This mast's wind direction values have been previously validated for correctness, ensuring a reliable basis for validation in this study. Further details on this validation procedure will be elaborated in the subsequent section 3.4.

Preprocessing of the Heliostat Tracking Data

The project partner CIEMAT provided for the time span of the measurement campaign the tracking data of each heliostat of the CESA-1 heliostat field in a customized text format. To assess the tracking status of the heliostats, the provided tracking data of elevation and azimuth angles for each heliostat and timestamp has to be preprocessed to ensure comparability with existing wind data. In a first step, the tracking data, available in multiple files of varying dimensions, is concatenated into a single matrix in Matlab.

In a second step, the timestamps of the heliostat tracking data have to be harmonized with the timestamps of the anemometer data. In the chosen approach for this tasks, it is assumed that during periods where no heliostat tracking data was available because the heliostats have not been moved, the heliostat elevation and azimuth angles remained the same as for the last available timestamp. With this method, the heliostat tracking angle data set has the same number of timestamps as the anemometer data.

3.2.2 LiDAR Data

The LiDAR data have been processed by the project partner Fraunhofer IEE and then provided to DLR. The data exchange between project partners was facilitated through the use of .csv files, ensuring seamless collaboration and data integration.

The LiDAR data is organized in a 2D structure comprising grid points distributed across the heliostat field. Approximately every 3three meters, there are a total of 1426 grid points (GPs) in this configuration. Each grid point contains existing data such as timestamps, wind direction, horizontal wind components u and v, and wind speed.

The LiDAR data originally used GPS data. Therefore, the data had to be transferred to Cartesian coordinates as defined by CIEMAT for the heliostat field. Thus a conversion process has been necessary due to the different coordinate systems.
For this, the coordinates of two fixed and known points (wind masts 2 and 4) are offset against each other and the LiDAR data coordinates have been corrected accordingly.

The timestamps, too, require a conversion. While the LiDAR data has been saved as UTC time, the anemometer data was recorded using the local time of UTC+1 (Spanish winter time). Also, the downsampling of the data was executed differently. The anemometer data have been downsampled towards the end of the 10 minute time frame, whereas the LiDAR data were allocated towards the beginning of the downsampled period. As such, there is a 70 minutes time difference to be taken into account when dealing with the transferred LiDAR data.

3.3 Data Evaluation

3.3.1 General Wind Effects

Strictly speaking, the calculation of the wind speed and wind direction – here classified as preprocessing and described prior in chapter 3.2.1 – is the first step of the data evaluation. After their validation, the calculation of the general wind effects as described in chapter 2.2 can be undertaken. In this context, wind gusts, turbulence intensity and roughness length are calculated. Furthermore, the frequency distributions and diurnal courses of the wind pattern are calculated and wind rose programmed from the wind data. Additionally, filters for the data set are implemented, enabling filtering for wind direction and tracking status, among others.

3.3.2 Calculation of Target Area

The Target Area (TA) is defined as the surface area of the heliostat perpendicular to the wind, depending on the wind direction and orientation of the heliostat. The reference wind direction chosen for this calculation is taken from the anemometer at 10-meter height on wind mast 1 and is performed for each heliostat in the heliostat field individually

The TA of each heliostat is specified by its azimuth and elevation angles. The calculation proceeds in three distinct steps at every timestamp (i = 25220) of the analysed data for each of the heliostats (j = 300).

First, the calculation of the heliostat's target area influenced solely by the elevation angle is performed. Since only horizontal wind direction is considered in this study, the target area (TA_{ele}) is a function of the elevation angle. With the heliostat facing downward at an elevation

angle of $\varepsilon = 0°$ and thus offering in its stow position theoretically zero target area, TA_{ele} can be calculated as following:

$$TA_{ele,ij} = |\sin\left(\varepsilon_{ij}\right)| \tag{21}$$

Next, the calculation of the heliostat's target area influenced by the azimuth angle is carried out. Variables influencing this target area (TA_{azi}) include both azimuth angle and wind direction. Therefore, the difference between the azimuth angle of each heliostat and the wind direction has to be calculated.

$$\Delta\theta_{ij} = \beta_i - \left(\alpha_{ij} + 90°\right) \tag{22}$$

The second part of the equation considers the 90° offset between azimuth and wind direction angle as revealed by their respective coordinate systems given in chapter 2. $TA_{azi,ij}$ can be calculated as follows:

$$TA_{azi,ij} = |\cos\left(\Delta\theta_{ij}\right)| \tag{23}$$

Finally, the total target area in percentage ($TA_{\%}$) for each heliostat can be derived by combining equations 21 and 23

$$TA_{\%,ij} = TA_{azi,ij} \odot TA_{ele,ij} \tag{24}$$

or alternatively expressed fully as

$$TA_{\%,ij} = |\cos\left(\beta_i - \left(\alpha_{ij} + 90°\right)\right)| \odot |\sin\left(\varepsilon_{ij}\right)|. \tag{25}$$

To obtain the absolute target area for the heliostats TA_{total}, $TA_{\%}$ is multiplied by the total area of the heliostats A_{HS}. The values for the calculation of A_{HS} can be found in table 2.3.

$$TA_{total,ij} = TA_{\%,ij} \cdot A_{HS} = TA_{\%,ij} \cdot \left(\Sigma Panel_x + \Sigma Panel_y\right) \tag{26}$$

Calculating $TA_{\%,ij}$ for a certain timestamp, the tracking status for each single heliostat can be visualized with an implemented Matlab routine. For this, a scaled-down two-dimensional plot of the heliostat field is generated using Matlab for visualization purposes. This plot allows for the depiction of the tracking status across the entire heliostat field throughout each timestamp, enabling a comprehensive visual representation of the data. An example of the 2D-field-plot can be found in chapter 3.4, where the visualization is further discussed.

3.3.3 Heliostat Tracking Status Impact on Wind Field

The objective is to quantify the influence of the heliostat tracking status on wind within the heliostat field. For this purpose, the parameter impact Υ has been defined, which describes the wind field changes dependent on target area

$$\Upsilon = \frac{\text{Difference in wind effect parameter}}{\text{Target area}} \tag{27}$$

Gamma can be calculated considering the wind speed changes within the heliostat field, but can also be used to describe changes of e.g. the turbulence intensity within the heliostat field. To ensure reliability, only instances where wind direction β aligns with the measurement line (ML) of the wind masts are considered. For that, wind mast 1 at 7 m height is chosen as the reference wind direction measurement.

The cardinal direction of the measurement line is determined using Google Earth, resulting in 232°. In a next step, times in the dataset where the wind direction is within ±5° of the direction of ML are identified. Additionally, the heliostats that are located within the measurement line are identified. Said heliostats are also shown in the sketch of the heliostat field in fig. 3.2.

Invalid data points are eliminated, retaining only instances where all wind masts have data available. After this, $k = 805$ data points remain for further evaluation. After the preparation and filtering of the data is done, the impact Υ of the summed up TA_{ML} of the heliostats which lie within ± 5° of the direction of the measurement line on the wind speed within the heliostat field between two different wind masts can be calculated as follows.

$$\Upsilon = \frac{\Delta U_{abs}}{U_{ref} \cdot \Delta\left(\Sigma TA\right)} \tag{28}$$

with ΔU_{abs} being the absolute difference between the examined fields innermost and outermost anemometer in 7 m height and U_{ref} being the examined fields outermost anemometer in 7 m height (usually at wind mast 1). $\Delta\left(\Sigma TA\right)$, further also referred to as TA_{ML} represents the difference in the total target area accumulated by the different heliostat rows over the course of the heliostat field between the innermost examined point and the outermost examined point. Additionally to the tracking status, which calculates the effective area of the heliostat mirrors, for each heliostat row that the wind passes, a basic target area TA_B is added, taking into account the steel frame of the heliostats. TA_B is approximated by the calculation of

$$TA_B = D_{pole} \cdot H_{pole}. \tag{29}$$

The relevant data for the calculation of T_B can be taken from table 2.3. Therefore, equation 28 can also be written more elaborated as

$$\Upsilon = \frac{U_{m_i,k} - U_{m_o,k}}{U_{m_o,k} \cdot \left[\sum_{r=0}^{r_i}\left(TA_{total,k}\right) - \sum_{r=}^{r_i}\left(TA_{total,k}\right) + (r_i - r_o) \cdot \left(D_{pole} \cdot H_{pole}\right)\right]} \tag{30}$$

with m_i and m_o being the innermost and outermost wind mast respectively. Analogously, r_i and r_o are the heliostat rows behind the innermost and the heliostat row before the outer most examined wind mast respectively.

Using equation 30, the impact for all 805 filtered timestamps can be calculated. With this approach, the quantification of the specific influence of heliostat tracking status on wind speed within the heliostat field is analysed. The results are discussed in chapter 4.

3.3.4 Turbulence Spectra

The turbulence spectra are calculated in Matlab with the help of the signal processing toolbox. The Matlab function `pwelch` computes the power spectral density vector and the corresponding vector of frequencies.

$$\left[S_Q, f_Q\right] = \texttt{pwelch}\left(Q, NFFT, f_S\right) \tag{31}$$

With the power spectral density vector S_Q and the corresponding vector of frequencies f_Q, Q is the input signal vector, f_S the sampling rate of the observed sensor in Hz and the number of bins for the Fast Fourier Transformation (FFT), $NFFT$ can be calculated with

$$NFFT = 2^{\texttt{nextpow2}(NBS)} = 2^{\texttt{nextpow2}\left(f_s \cdot T_f\right)} \tag{32}$$

where T_f is the block length, which can be understood as the time resolution in seconds. Therefore, when multiplicated with sampling rate f_S, NBS results in the number of samples per block. `nextpow2` is another Matlab function. It calculates the next power of 2.

The turbulence spectra for all nine anemometers and each of the 23 associated wind components as well as the horizontal wind speed U have been calculated. the sampling rate f_S have been 4 Hz and 20 Hz for the WindSonic and WindMaster anemometers, respectively. The temporal resolution of each block (block length T_f) has been set to 10 minutes.

3.3.5 Evaluation of Lidar Data

The objective of processing LiDAR data is to generate a detailed 2D field representation of wind speed (U) through scattered grid points, facilitating a comprehensive analysis of wind speed and wind direction at specific timestamps. Adding a third dimension via color coding depicts the measured wind patterns.

Initially, the Delaunay function is utilized to create an initial rough surface plot using trisurf from irregular data points. Refinement involves an interpolation step: first averaging Delaunay grid values to obtain new x, y, and z values for a smoother yet slightly coarse surface. This process repeats in a second cycle with the interpolated data (x_2, y_2, z_2), yielding a finer surface plot as depicted in the figure. This iterative method enhances the representation's detail and accuracy, crucial for analyzing wind speed data effectively.

3.4 Data Validation

This chapter shows the validation of the preprocessed data, ensuring its accuracy for subsequent evaluation and analysis. Before delving into wind dynamics across the heliostat field, it is imperative to validate both anemometer and LiDAR measurements, particularly focusing on wind speed and wind direction parameters.

The validation process begins by examining individual wind component measurements and subsequently comparing the calculated wind speed and wind direction results between the two measurement methods. Given that the LiDAR data is collected at a height of 10 meters, wind mast 1 serves as a preferred reference for anemometer data comparison. Consequently, for LiDAR data, the grid points near the 10-meter mast are averaged and evaluated.

Furthermore, this chapter investigates the impact of using vectorial calculations instead of scalar calculations for anemometer wind direction. By doing so, any resulting influences on data interpretation and analysis are assessed.

3.4.1 Wind Speed

The initial step involves validating the calculated wind speeds derived from both anemometer and LiDAR data sources. By selecting specific days, one from winter and another from summer, within a short time frame, potential errors stemming from incorrect timestamps can be rectified. The comparison of results for the 23rd of February and 13th of April, depicted in the line graph in figure 3.4, highlights the concordance between both datasets, affirming the accuracy of the measurements.

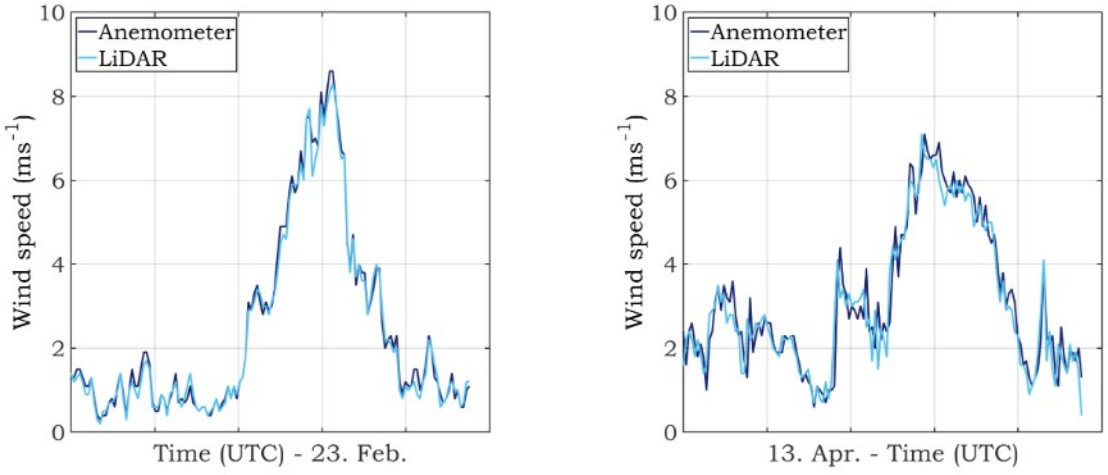

(a) (b)

Fig. 3.4: Comparison of measured anemometer wind speed and reconstructed LiDAR wind speed in a line plot. Horizontal wind speed on a) 2023-02-23 and b) 2023-04-13.

When analysing data on a larger timescale, a line graph becomes less effective for readability, prompting the use of a scatter plot to visualize the data. This scatter plot demonstrates the agreement between LiDAR and anemometer data while also displaying a trend line. Additionally, metrics such as the root mean square deviation (RMSD) and mean absolute deviation (MAD), which is less influenced by outliers, are assessed. Figure 3.5 encompasses the entire study period from February 15th to May 31st, providing a comprehensive view of the data trends and correlations.

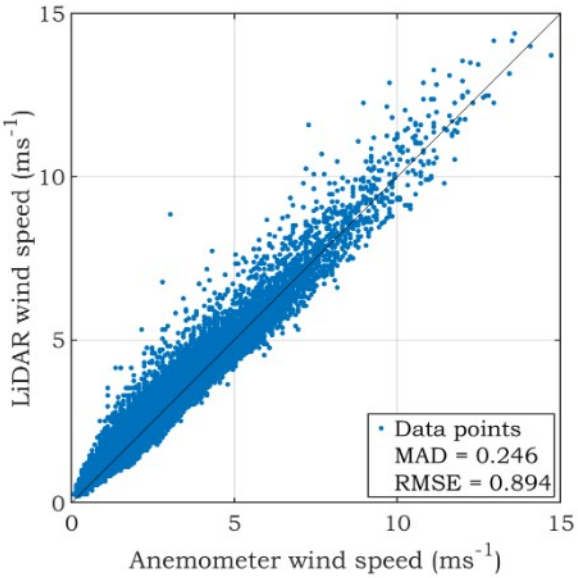

Fig. 3.5: Comparison of measured anemometer wind speed and reconstructed LiDAR wind speed in a scatter plot, showing the agreement between reconstructed LiDAR values and anemometer data for entire time frame from 2023-02-15 to 2023-05-31.

Upon visual inspection, the scatter points align closely with the trend line, showcasing a strong correlation between the datasets. Additionally, the provided MAD and RMSD values further reinforce the conclusion that both datasets exhibit a good fit and demonstrate a high degree of correlation.

3.4.2 Plausibility Check of Wind Direction Data

To confirm the plausibility of the wind direction measurements both from the anemometers as well as derived from the LiDAR measurements during the measurement campaign, the data has been compared to another anemometer reference measurement in 10 m height above ground which is mounted in the South of PSA (the so-called HP station) The comparative matrix is shown in 3.5, where the colours from light to dark blue represent the size of the angular deviation. Hereby, light blue stands for a variation of 20° – 30° , while middle blue depict variations between 5° and 15° and dark blue means a (nearly) perfect fit between wind directions with deviations of less than 5°.

Table 3.5: Comparison of the different wind directions with each other. *Outside* and *inside* cover the anemometer data. Outside refers to wind mast 1 on the outer line of the heliostat field at different heights, while inside encompasses all three other wind masts 2 – 4, since they displayed a perfect fit with each other. For the LiDAR data a point near wind mast 1 was chosen. HP is a measurement station for another project outside the proximity of the CESA-I facility with validated wind direction.

	outside, 10 m	outside, 7 m	outside, 4 m	inside, 7 m	inside, 4 m	LiDAR, 10 m	HP as ref.
M1, 10 m		20–30°	20–30°	5–15°	5–15°	10–15°	
M1, 7 m	20–30°					10–15°	20–30°
M1, 4 m	20–30°					10–15°	20–30°
M2, 7 m	5–15°						5–15°
M3, 7 m	5–15°						5–15°
M4, 7 m	5–15°						5–15°
M2, 4 m	5–15°						5–15°
M3, 4 m	5–15°						5–15°
M4, 4 m	5–15°						5–15°
LiDAR	10–15°	10–15°	10–15°				10–15°
HP as ref.		20–30°	20–30°	5–15°	5–15°	10–15°	

There is a strong correlation observed among individual wind direction measurements. The anemometer positioned at 10 meters height on wind mast 1 outside the heliostat field exhibits the closest match with the referenced HP wind mast. This may be attributed to the fact that both instruments are positioned at a height of 10 meters, enhancing their agreement in capturing wind direction accurately.
Conversely, the anemometers at heights of 4 meters and 7 meters on the same wind mast

exhibit the most significant deviations, reaching up to 30° when compared to both the 10-meter anemometer and the HP wind mast. This discrepancy suggests potential challenges in wind direction measurement accuracy at lower heights, which has to be kept in mind during the following evaluation.

The most accurate alignment is observed among the innerfield anemometers, where each height level demonstrates a nearly perfect fit. LiDAR data, even though measured in 10 m height and as such higher than most anemometers, also displays a reliable correlation overall, with minor deviations noted primarily in relation to the outer field anemometers.

To summarize the validation process, the wind direction data could be validated for all anemometer data as well as the LiDAR measurement data. Both data sets show a good fit for further evaluation prospects.

Scalar vs. Vectorial Wind Speed

To investigate the impact of scalar versus vectorial wind direction calculations, an exemplary analysis was conducted using data from wind mast 1 at a height of 10 meters. A scatter plot was generated to compare β_{sca} and β_{vec}, as depicted in Figure **??**. The plot shows a strong correlation between both data sets, displaying an overall alignment with the diagonal trend line.

The comparison of both calculation methods resulted in a RMSE of 1.878 and MBE of -0.037. It has to be noted that the discontinuity in angle transition between 0° and 360° cause higher statistic deviations of both methods.

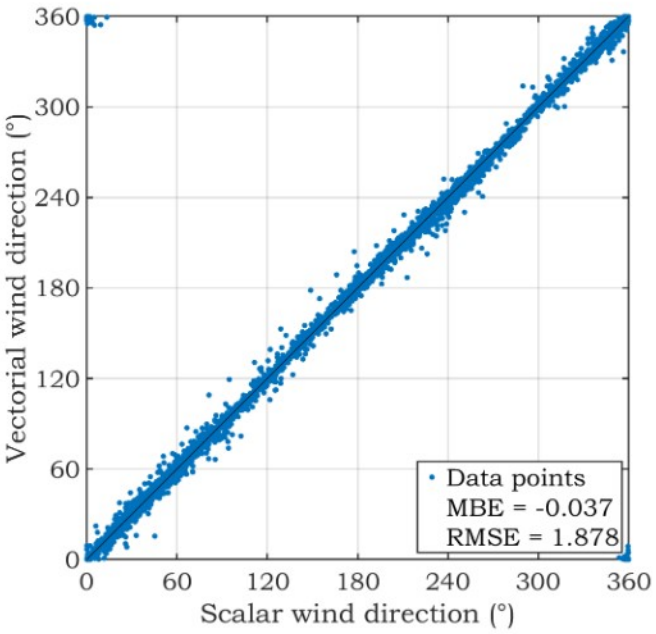

Fig. 3.6: Comparison of the scalar (β_{sca}) and vectorial (β_{vec}) calculated wind directions in a scatter plot to analyse the impact of the different way of calculation.

After addressing the transition discontinuities and mitigating outlier effects through transition correction, the residual impact on statistical values remains minimal. Therefore, is has been decided, that the vectorial calculation method is used for further evaluations within this thesis.

3.4.3 Preprocessed Tracking Data

As noted during the explanation of the preprocessing of the tracking data in chapter 3.2.1 the earlier version of the tracking data preprocessing causes artificial steps in the downsampled tracking data at times when no tracking data is available.

Figure 3.7 shows an exemplary data set of the elevation and azimuth tracking angles for one heliostat in the first half of May 2023. The original elevation and azimuth data points are shown as red dots, while the preprocessed data set for the azimuth and elevation angles is presented in a straight blue line. It can be seen, that no tracking data is available for this heliostat during several time periods, e.g. during weekends, when the CESA-1 plant has not been operated.

Like in chapter 3.2.1 described, during each data gap, it has been assumed that the elevation and azimuth angle of the heliostat correspond to the last available data point before the data gap as the conjecture is that the heliostats have not been moved in the meanwhile.

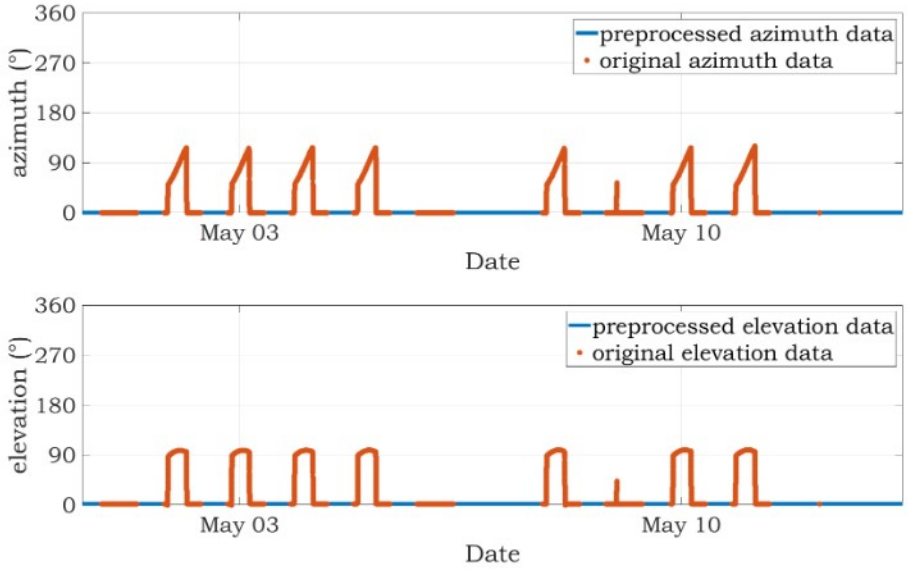

Fig. 3.7: Exemplary original and preprocessed elevation (red) and azimuth angles (blue) for the heliostat XY during May 2023. The original data points are shown with star symbols and the preprocessed data are depicted in a straight line.

As stated before, it can indeed be reasonably assumed that during those times the heliostats were in stow, as those times fall on either weekends or holidays. As such, no changes in the

heliostats' tracking status should have happened during those times and he code works as expected by substituting the missing data by value the of the last known tracking status.

For the sake of completeness, fig. 3.8 shows the preprocessed elevation and azimuth data of all heliostats during the analysed period between February 15th and May 31st 2023.

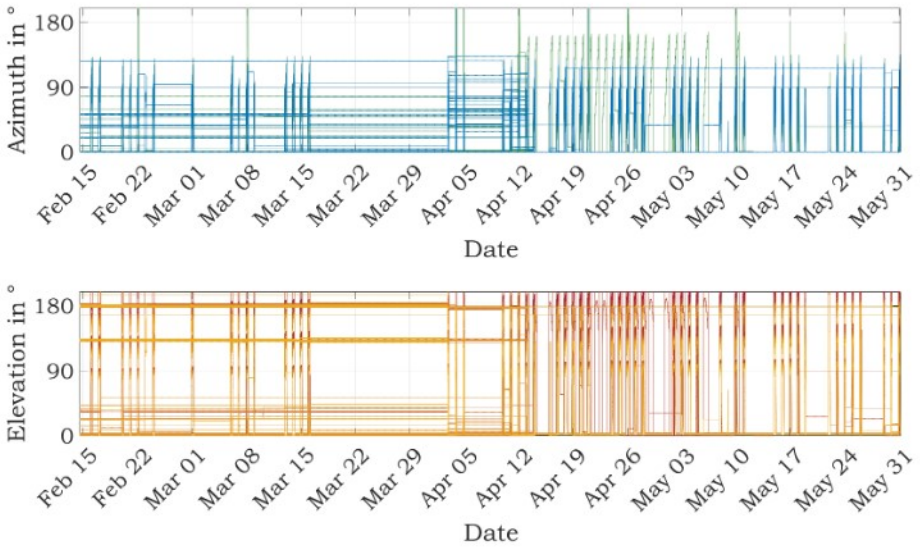

Fig. 3.8: Preprocessed elevation (blue line) and azimuth (red line) data of all heliostats of the CESA-1 heliostat field during the analysed period between Feb. 15th and May 31, 2023.

As can be seen in the figure, plotting the results in a line graph is highly impractical for more than a few different heliostats at each time – a fact that also shows in the calculation of the target area. Therefore, the previously prepared 2D field plot is assigned a colour scheme to represent the azimuth and elevation angles, combined in the form of the calculated $TA_{\%}$ for each heliostat. An example of said plot, for April 13th 2023 at 15:40 h as it will be used for later evaluation in chapter 4 can be seen in fig. 3.9.

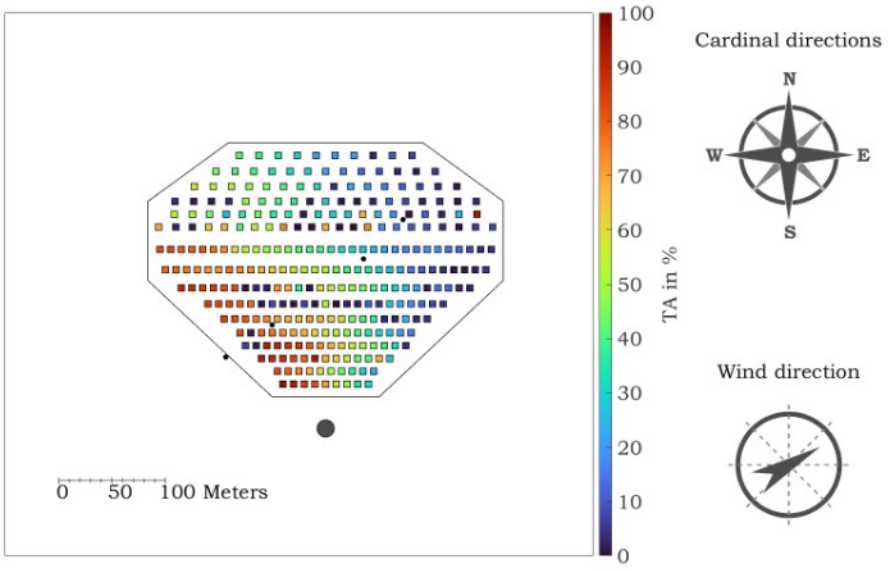

Fig. 3.9: Scaled-down drawing of the CESA-I heliostat field using Matlab with colours assigned to the heliostats representing the individual $TA_{\%}$ at the chosen time stamp (2023-04-13 15:40:00). The top right corner shows how the field align with the cardinal directions. The bottom right corner shows the prevailing wind direction for the considered timestamp.

Summary

To summarize the data validation of the wind speed, it can be affirmed that there is a good agreement between the LiDAR reconstruction data and the anemometer data. Although some larger deviations are present between the two datasets, the overall fit is deemed satisfactory for the analysis intended in this study. Given the objective of identifying broader trends across the entire field, minor mean absolute deviations are unlikely to significantly impact the resulting analysis outcomes.

The use of vectorial calculations for wind direction in anemometer data is expected to have minimal to negligible impact on the evaluation of the wind data. This expectation is supported by the high degree of correlation observed between the two datasets, indicating strong agreement and consistency in wind direction measurements.

An analysis of the heliostats tracking status preprocessing and the resulting calculation of the target area could also validate the reliable usage for further processing. The elevation and azimuth angles align with the measurement, filling out data gaps in the original tracking status. Lastly, the target area is correctly assigned to the individual heliostats across the heliostat field.

4 Results and Discussion

The presented analysis is based on unpublished data collected during the previously described measurement campaign from December 2022 to June 2023. However, due to maintenance occurring during the winter months, the evaluation period is restricted to the time between February 15th and May 31st 2023. In chapter 4, the results of the data analysis conducted in this thesis are summarized.

Chapter 4.1 presents the analysis of long-term measurements using ultrasonic anemometers positioned outside the heliostat field to minimize environmental influence. This analysis aims to establish a general understanding of the aerodynamic conditions at the test site and sets the context for further investigation. As a result, the influences of different heights on the wind effects are also analysed.

Chapter 4.2 delves into the heliostat field's impact on wind patterns. The analysis concentrates on evaluating the changes within the horizontal plane created by the set of anemometers at the same height.

Chapter 4.3 examines how the heliostat tracking status affects wind conditions within the field. Additionally, in Chapter 5.4, comparisons between 2D measurements obtained from the mounted scanning LiDAR scanners and data from anemometers are explored.

If not otherwise stated, the presented data is averaged during the analysed time frame as long as it is possible and appropriate in the context of the thesis' subject. Wind masts 1, 2, 3 and 4 are hereafter commonly referred to as M1, M2, M3 and M4, often in conjunction with the respective height at which the measurement equipment is attached (4 m, 7 m and 10 m). The data was recorded with a temporal resolution of 4 Hz or 20 Hz respectively, though only the downsampled data was further analysed. Therefore, if it is spoken about a single timestamp during the following discussion, the time frame consists of the 10-minute moving average.

4.1 Ultrasonic Anemometer Measurements outside the Heliostat Field

In the following chapter 4.1, the ultrasonic anemometer measurements during the measurement campaign are analysed to describe the wind pattern outside the heliostat field. For this analysis, all data points from February 15th until May 31st 2023 have been considered.

4.1.1 Wind Speed

Frequency Distribution

In facility design, probability density functions (PDFs) are commonly used to statistically model wind speed frequency for wind farms. This distribution is typically represented using a Weibull

distribution, as outlined in the international standard IEC 61400-1 published by the International Electrotechnical Commission (IEC) [72]. These wind speed frequency distributions aid in defining specific load cases for typical design conditions, assuming that the average wind speed over 10-minute intervals at the site follows this PDF.

To find out, whether this is also the case for the CESA-I test site, the frequency distributions for the wind speeds at all nine anemometers have been calculated. Figure 4.1 shows the measured frequency distribution at wind mast 1 of the three anemometers in different heights.

Generally, the wind speed increases with height, with an average wind speed of 2.63 ms^{-1} at 4 m height compared to 3.26 ms^{-1} at 10 m height. The frequency distribution shows a more pronounced peak at 4m height where the maximum frequency is 20 % in comparison to 13 % at 10m height. All heights have their maximum frequency at 1 ms^{-1}.

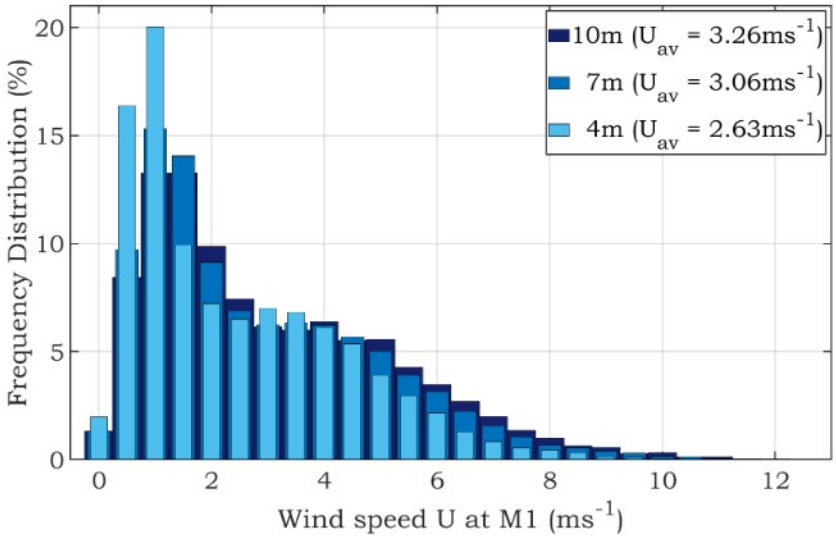

Fig. 4.1: Frequency distribution of the horizontal wind speed U at wind mast 1 for all three different heights 4 m, 7 m and 10 m during the measured period of 2023-02-15 to 2023-05-31.

Alls wind speed frequency distribution indicate two distinct occurrences representing different wind seasons, typically labelled as "low-wind" and "high-wind" seasons. However, in this case, it is more apt to describe them as "low-wind" and "medium-wind" seasons since strong winds are categorized by speeds higher than 10 m/s.

At the testing site, the majority of wind speeds (60 – 70 %) fall between 0 – 3 ms^{-1}, categorized as weak winds. Medium wind speeds are the second most frequent category, constituting nearly all other measured wind speeds. High wind speeds are only very infrequently measured at 7 m and 10 m height and no wind speed higher than 12 ms^{-1} have been measured.

Average Diurnal Course of Wind Speed

The diurnal course visualizes the wind speed variation over a 24-hour period, averaged over the complete observed time frame from February 15th to May 31st 2023. Figure 4.2 shows the averaged diurnal course of measured wind speed at wind mast 1 in 4m, 7m and 10m height, which exhibit a pronounced diurnal pattern. The pattern is is clearly depicted in fig. 4.2, reaching a minimum during the morning hours (between 1.5 ms^{-1} and 2 ms^{-1} depending on the measurement height), followed by a rapid increase afterwards with peak wind speeds typically occurring in the afternoon around 16:00 h with values of approx. 5 ms^{-1} to 5.8 ms^{-1}.

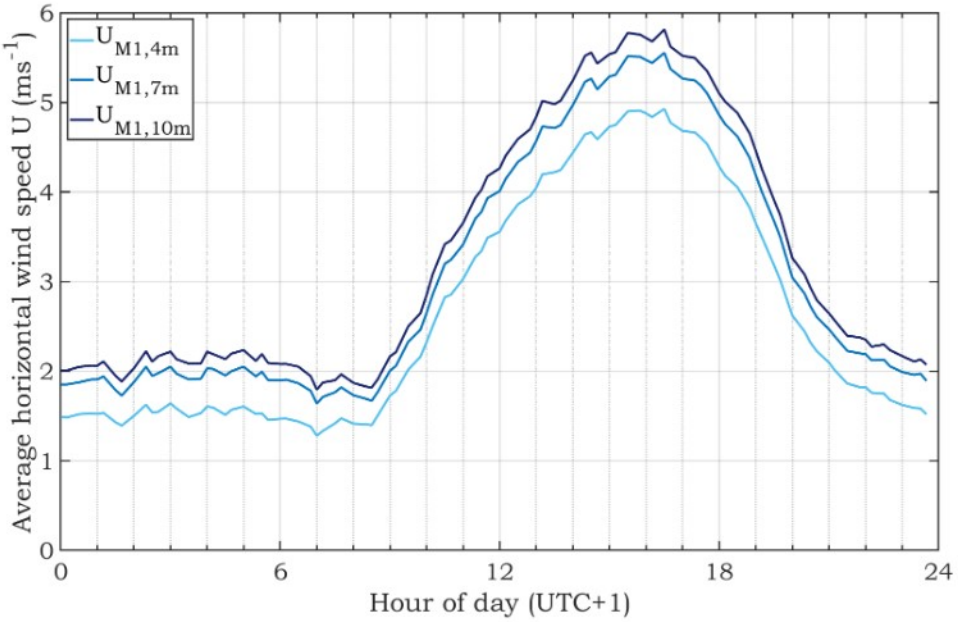

Fig. 4.2: Mean diurnal wind speed of the anemometer data at wind mast 1 in 4 m, 7 m and 10 m height for the measured period of 2023-02-15 to 2023-05-31

In the figure, all three anemometers of wind mast 1 at the different heights are juxtaposed with each other. By doing so, the typical height profile of the wind speed – the increase with increasing height – can be shown. Hereby, the three curves seem to roughly retain the same absolute distance from each other (approx. 0.5 – 0.6 ms^{-1} between 4 m and 7 m height and 0.2 – 0.3 ms^{-1} between 7 m and 10 m), regardless of the hour of the day or their wind speed.

The significant fluctuation in wind speed over time may be attributed to the geographic features surrounding the solar plant. Positioned on a plateau flanked by northern and southern mountain ranges, the plain experiences less obstruction along its east-west axis. More detailed information about the topology in form of GoogleEarth pictures are added in the annex (cf. A.1). Throughout the day, solar heating of the plain induces rising air currents or up-drafts. The rising air then leads to a balancing current from the west or east. The evaluation of the wind direction confirms that the main wind directions are east, west and south-west. The temporal

progressions of the measured wind speeds correlate with the explanatory approach described. In addition, the weather conditions at the platform site are predominantly westerly or, to a lesser extent, easterly.

4.1.2 Wind Direction

Figure 4.3 visualises the wind direction distribution of the horizontal wind speed U at wind mast 1, measured at a height of 10 meters during the time period from February 15th to May 31st 2023. The shading of the bars in the wind rose diagram corresponds to the wind speed ranges mentioned earlier. The length of the bars represents the proportion of each direction and wind speed range.

The prevailing wind direction in 10 m height ranges from the south-west to west (230° to 270°), followed closely by east to south-east (90° to 120°). Wind speeds between $4-10\,\mathrm{ms}^{-1}$ are most common in these directions. Higher wind speeds are primarily observed from the north-west. Winds originating from the south and north are uncommon, partially due to the wind shielding effect provided by the solar tower located to the south of the heliostat field.

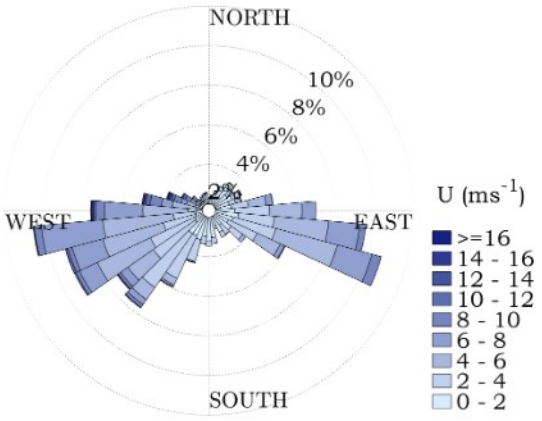

Fig. 4.3: Wind direction distribution of the horizontal wind speed U at wind mast 1 in 10 m height from 2023-02-15 to 2023-05-31.

In figure 4.4 the wind roses of the other two measured heights are depicted for the purpose of comparing the different heights with each other. Fig. 4.4a shows the wind roses for wind mast 1 data in 4 m, fig. 4.4b in 7 m height.

The horizontal wind distributions at both lower heights exhibit a slight deviation of about $20°-30°$ in wind direction toward the south compared to the 10 m anemometer data. Whereas the wind distribution between 4 m and 7 m do not vary significantly in regards to the wind direction, the horizontal wind speed distribution shows slightly higher magnitudes at 7 m height. The wind rose at 10 m height follows the trend of increased wind speeds at higher

heights by exhibiting the highest wind speed distributions and ostensibly the fewest cases of low wind speeds.

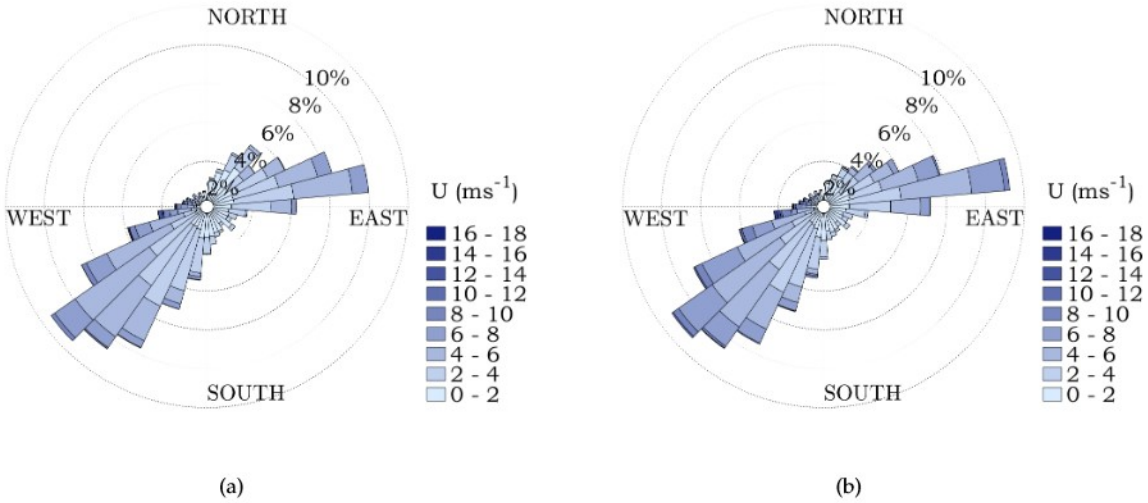

Fig. 4.4: Wind direction distribution of the horizontal wind speed U at wind mast 1 in a) 4 m and b) 7 m height from 2023-02-15 to 2023-05-31.

4.1.3 Wind Gust

To analyse the wind speed changes, wind gusts have been calculated according to the description in chapter 2.2.3 and are examined here for 10 minute resolved wind data. Figure 4.12 shows the 10-minute horizontal wind gust G in comparison to the mean wind speed U measured at wind mast 1 for all three heights (4 m, 7 m and 10 m).

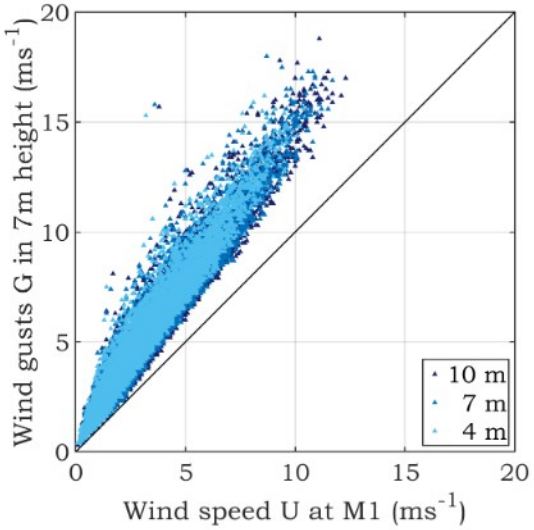

Fig. 4.5: Horizontal wind gust G versus horizontal wind speed U (10-minute resolution) for wind mast 1 at 4 m, 7 m and 10 m height for the measured period of 2023-02-15 to 2023-05-31.

The wind gusts are generally stronger than wind speeds, aligning with common expectations. Their values increase as the wind speed increases, reaching maximum values of up to 18 ms^1, which is about 61 % higher than the corresponding wind speed U. The magnitude of wind gusts remains consistent across different heights, typically ranging from approximately 41 % to 77 % stronger magnitudes of G than the average wind speed U at those heights. Moreover, there is no notable variance in this percentage between heights.

4.1.4 Turbulence Intensity

The frequency distribution of turbulence intensity I has been derived mirroring the methodology applied to wind speed distribution. Figure 4.6 shows the measured frequency distribution of the three anemometers at wind mast 1 in different heights.

It can be seen that the turbulence intensity I decreases slightly at higher heights with the average turbulence intensity being approx. 26 % at 10 m height compared to 28 % at 4 m height. The maximum frequency is at turbulence intensity of 20 % with a frequency distribution of nearly 50 % for all heights.

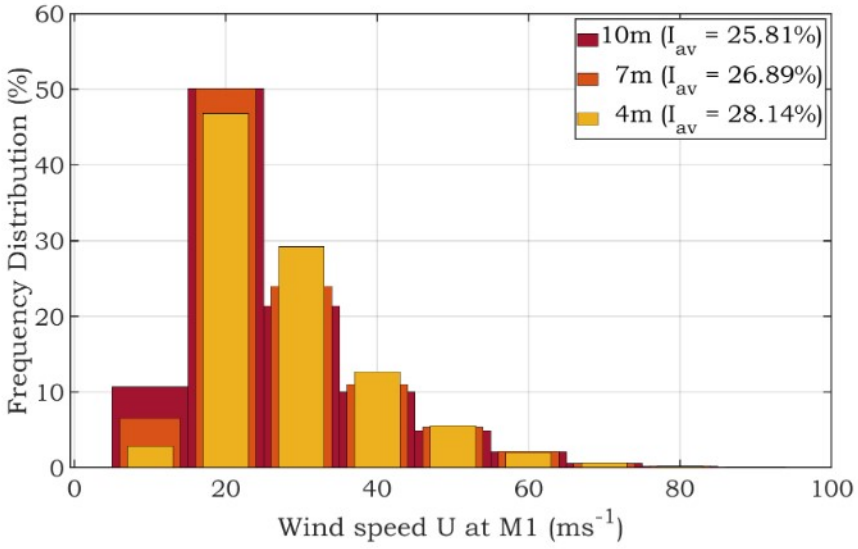

Fig. 4.6: Frequency distribution of the turbulence intensity I for wind mast 1 at 4 m, 7 m and 10 m height during the measured period of 2023-02-15 to 2023-05-31

4.1.5 Turbulence Spectra

With the help of the high temporal resolution of the ultrasonic anemometers (4 Hz for the WindSonic and 20 Hz for the WindMaster sensors, respectively), the turbulence spectra of the velocity fluctuations can be derived. The turbulence spectra can be used to describe the distribution of the velocity attributed to individual frequencies to the total variance (as discussed

in chapter 3.3.4). In this evaluation, the turbulence spectra for 10-minute intervals have been calculated for each wind component u, v and w and averaged over the complete time series from February 15th to May 31st 2023.

Additionally, empirical models from literature ([53, 54]) are used to approximate the horizontal turbulence spectra (see Kaimal and Panofski spectra in chapter 2.2.6). To approach the Kaimal and Panofski spectra as close as possible to the turbulence spectra measurements, the roughness height of the test site has to be estimated. Therefore, the roughness height z_0 was calculated from the turbulence intensity I_u for each anemometer data set. The mean roughness height derived at 10 m and 7 m heights was $z_0 = 0.2$ m each, whereas a z_0 of 0.1 m was calculated for the 4 m anemometer at wind mast 1.

The derived roughness height was used to compute and compare the Kaimal and Panofski model spectra with the turbulence spectra obtained from measurement data. Figure 4.7 compares the turbulence spectra of each height obtained from wind measurements with the model spectra defined by Kaimal and Panofski using the calculated roughness height.
To improve surveyability of the graphs, the wind speed turbulence spectrum S_U represents the combined longitudinal and latitudinal velocity fluctuations from the wind data S_u and S_v. Upon comparison, only minimal differences were observed among all three turbulence spectra, which are added for reference to the annex B.2 and B.3.

As mentioned earlier, the calculated roughness height falls within the range of 0.1 m to 0.2 m based on the wind data. Figure 4.7 (see next page) demonstrates that the Kaimal and Panofski models, using this roughness height, accurately depict the turbulence spectra. Roughness heights between $z_0 = 0.1$ m and $z_0 = 0.25$ m describe according to literature low to high crops with occasional scattered obstacles, with the actual value of z_0 depending on the frequency and height of said obstacles [53]. Based on the terrain characteristics of the site described above, the roughness height fits therefore into the expected range.

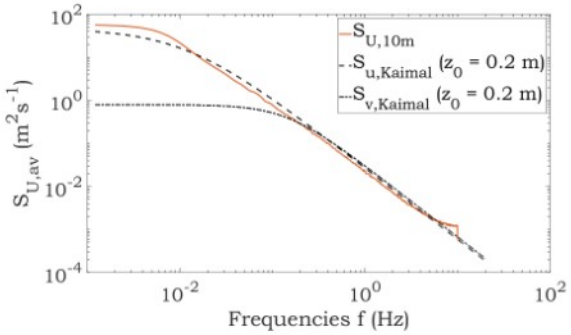

(a) cf. B.4 (annex)

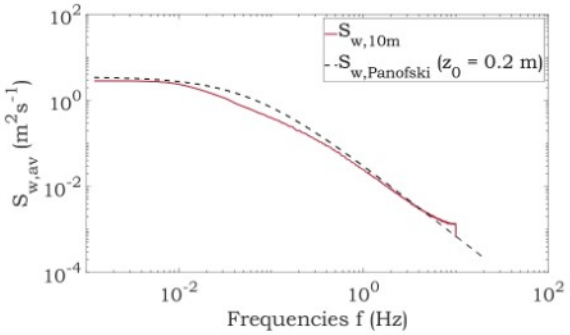

(b) cf. B.5 (annex)

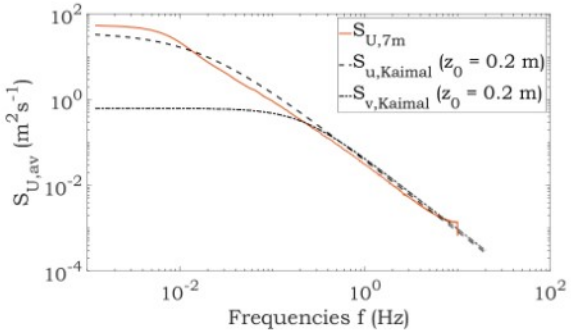

(c) cf. B.6 (annex)

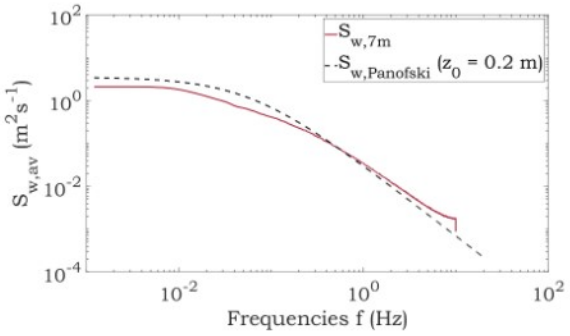

(d) cf. B.7 (annex)

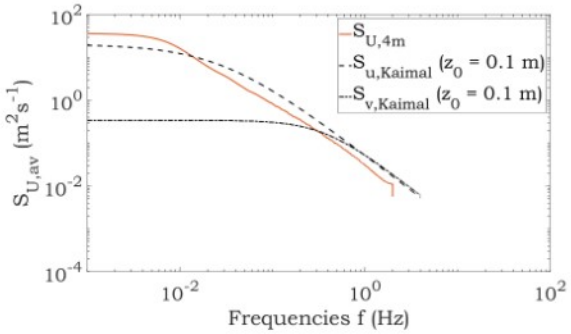

(e) cf. B.8 (annex)

Note:

Enlarged graphs for a more detailed view are added in the annex. For the electronic document, the figures are linked with each other using the references. This also goes for all following figures of turbulence spectra.

Fig. 4.7: Averaged Turbulence Spectra S for the combined horizontal wind component S_U (left: a, c and e) and vertical wind component S_w (right: b and d) in different heights 10 m (top: a and b), 7 m (middle: c and d) and 4 m (bottom: e) for the measured period of 2023-02-15 to 2023-05-31.

It is further examined how the turbulence spectra change over a variance in heights. For this, the turbulence spectra S_U and S_w of mast 1 are compared at 4 m, 7 m and 10 m heigh, as shown in figure 4.8.

At lower frequencies (up to $2 \cdot 10^{-2}$ Hz for S_U and $2 \cdot 10^{-1}$ Hz for S_w), turbulence spectra tend to be more pronounced for wind data collected at higher heights. This indicates that the wind at 10 m height exhibits larger vortexes compared to wind closer to the ground. As frequency increases, the curves begin to converge until reaching the specified inflection point. Beyond this point, turbulence spectra from lower heights show slightly higher turbulence levels than those from higher heights. This suggests that there are more smaller vortexes present at 4 m height compared to the wind at greater distances from the ground.

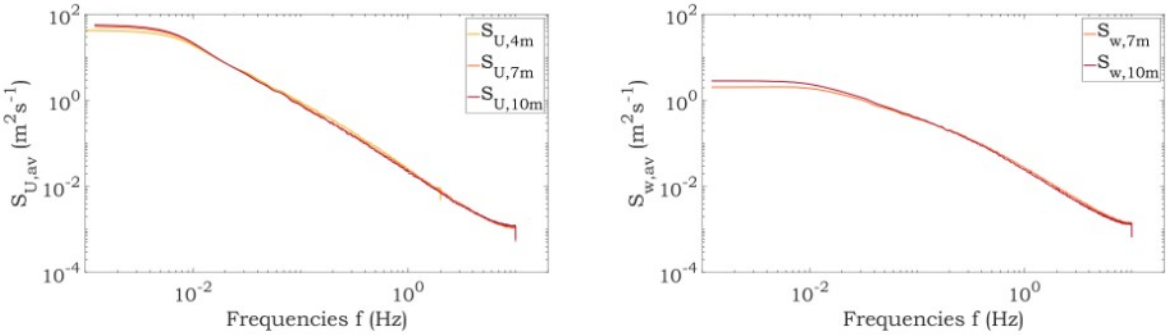

(a) cf. B.9 (annex) (b) cf. B.10 (annex)

Fig. 4.8: Averaged Turbulence Spectra S for the combined horizontal wind component S_U (a) and vertical wind component S_w (b) in different heights for the measured period of 2023-02-15 to 2023-05-31.

4.2 Impact of the Heliostat Field on Wind Patterns

To analyse the overall impact of the heliostat field on wind patterns within it, this chapter focuses on data collected between February 15th and May 31st 2023. Specifically, the analysis only includes data points where the wind direction at the reference wind mast 1, measured at a height of 10 meters above ground, falls within ± 5° of the wind mast measurement line direction as depicted in figure 3.2. Therefore, only data points with wind directions between 227° and 237° are analysed in the following subchapter.

In this context, the wind speed at the different wind masts and heights as well as their frequency distribution and diurnal curve is shown in chapter 4.2.1. In chapter 4.2.2, the wind direction measurements of the anemometers at the different positions within the heliostat field are discussed. Further, wind gusts measurements are analysed in chapter 4.2.3. The derived turbulence intensities and turbulence spectra for the different wind masts are evaluated in chapter 4.2.4 and 4.2.5.

4.2.1 Wind Speed

Frequency Distribution

Figure 4.9 shows the frequency distribution of the horizontal wind speed U at all wind masts measured in 4 m and 7 m height (fig.4.9a and fig.4.9b, respectively) during the measured period of February 15th to May 31st 2023. It visualises the change in wind pattern over the course of the field from the outermost (M1) to the innermost (M4) wind mast.

It can be seen that the frequency distribution from M1 over M2 and M3 to M4 shows a noticeable shift towards the lower wind speeds, which is more pronounced at the lower height of 4 m. This is also reflected in the average wind speeds which range from 1.86 ms^{-1} at wind mast 4 to

2.95 ms^{-1} at wind mast 1 in 4 m height and 2.69 ms^{-1} at wind mast 4 to 3.26 ms^{-1} at wind mast 1 in 7 m height .

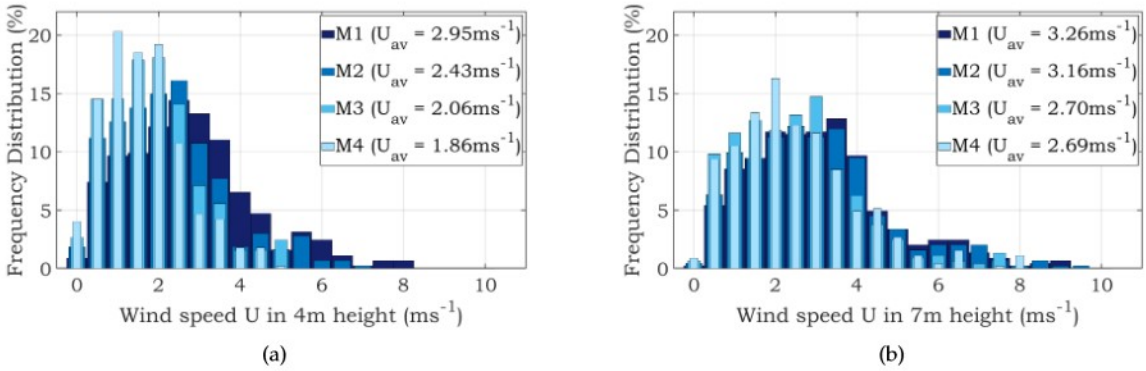

Fig. 4.9: Frequency distribution of the horizontal wind speed U at all wind masts in a) 4 m and b) 7 m height during the measured period of 2023-02-15 to 2023-05-31.

Mostly low wind speeds were measured by all eight anemometers compared in this analysis, ranging from 50 % at wind mast 1 in 7 m height to 90 % at wind mast 4 in 4 m height. In regards to the general frequency distribution of the wind speeds, a higher variance in wind speeds can be noticed at both, a higher height and a position of the wind mast further outside the field. However, the seasonal plateau noticed in the frequency distribution without the wind direction filter in the data is no longer present for wind speeds coming only from the south-west.

Average Diurnal Course of Wind Speed

Figure 4.2 shows the averaged diurnal course of the anemometer wind speed data measured during the period of February 15th to May 31st 2023. It compares all four wind masts each at height 4 m (straight line) and 7 m (dotted line).

The diurnal pattern observed in 4.1.1 is evident at all wind masts. It is driven by the fluctuation in atmospheric pressure throughout the day, primarily influenced by free convection from solar heating of the ground surface. Additionally, the surrounding terrain contributes to a shielding or wind tunneling effect. Minimum wind speeds during the night times range from 1.2 ms^{-1} to 1.8 ms^{-1} on average. Peaks are reached around 16:00 h and range from 3.8 ms^{-1} at M4 in 4 m height to 5.5 ms^{-1} at M1 in 7 m height.

Besides the already in chapter 4.1 established trend of decreasing velocity with decreasing height, it can be shown that the wind speed also decreases in the course of the heliostat field. For that, the wind masts show a slightly differently pronounced diurnal course at different heights. In 4 m height, the diurnal courses of wind mast 1 is noticeably more pronounced than those of the other wind masts, indicating that the wind speed at 4 m height decreases much more within the first part of the measurement line (between M1 and M2). At 7 m height,

the diurnal course also shows different manifestations. Here, however, the biggest impact is between M2 and M3, with the diurnal courses of the first two wind masts and the second two wind masts each showing similar features.

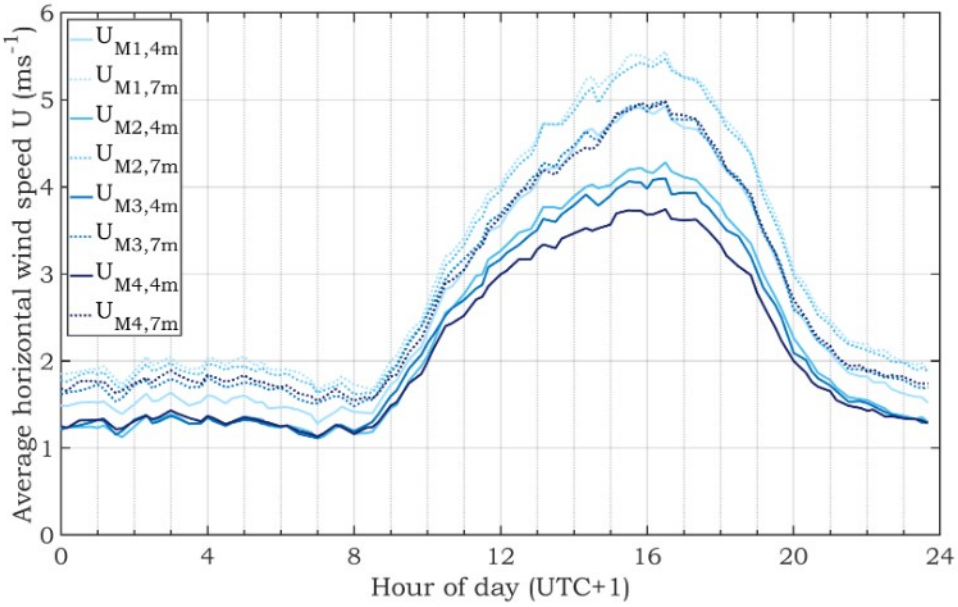

Fig. 4.10: Mean diurnal wind speed of the anemometer data at all wind masts in height 4 m and 7 m above ground for the measured period of 2023-02-15 to 2023-05-31

4.2.2 Wind Direction

Figure 4.11 visualises the wind direction distribution of the horizontal wind direction U at wind all four wind masts, measured at both 4 m height (top half: fig. 4.11a to 4.11d) and 7 m heigth (bottom half: fig. 4.11e to 4.11h). The measurement data from February 15th to May 31st 2023 is filtered for times when the wind direction at reference wind mast 1 aligns ± 5° with the wind masts' measurement line of 232°.

At wind mast 1, the wind direction distribution aligns well with the measurement line, proving the correct filtering of the data. Comparing the wind direction distribution over the course of the heliostat field, however, it shows a slight, but steady shift towards west between M1 and M4. With a maximum of 20°, said shift is less pronounced in 7 m measurement height. In 4 m height, however, changes in wind direction of up to + 40°, caused by the heliostats, can be observed. High variations in wind direction were mainly measured by wind mast 3 and wind mast 4.

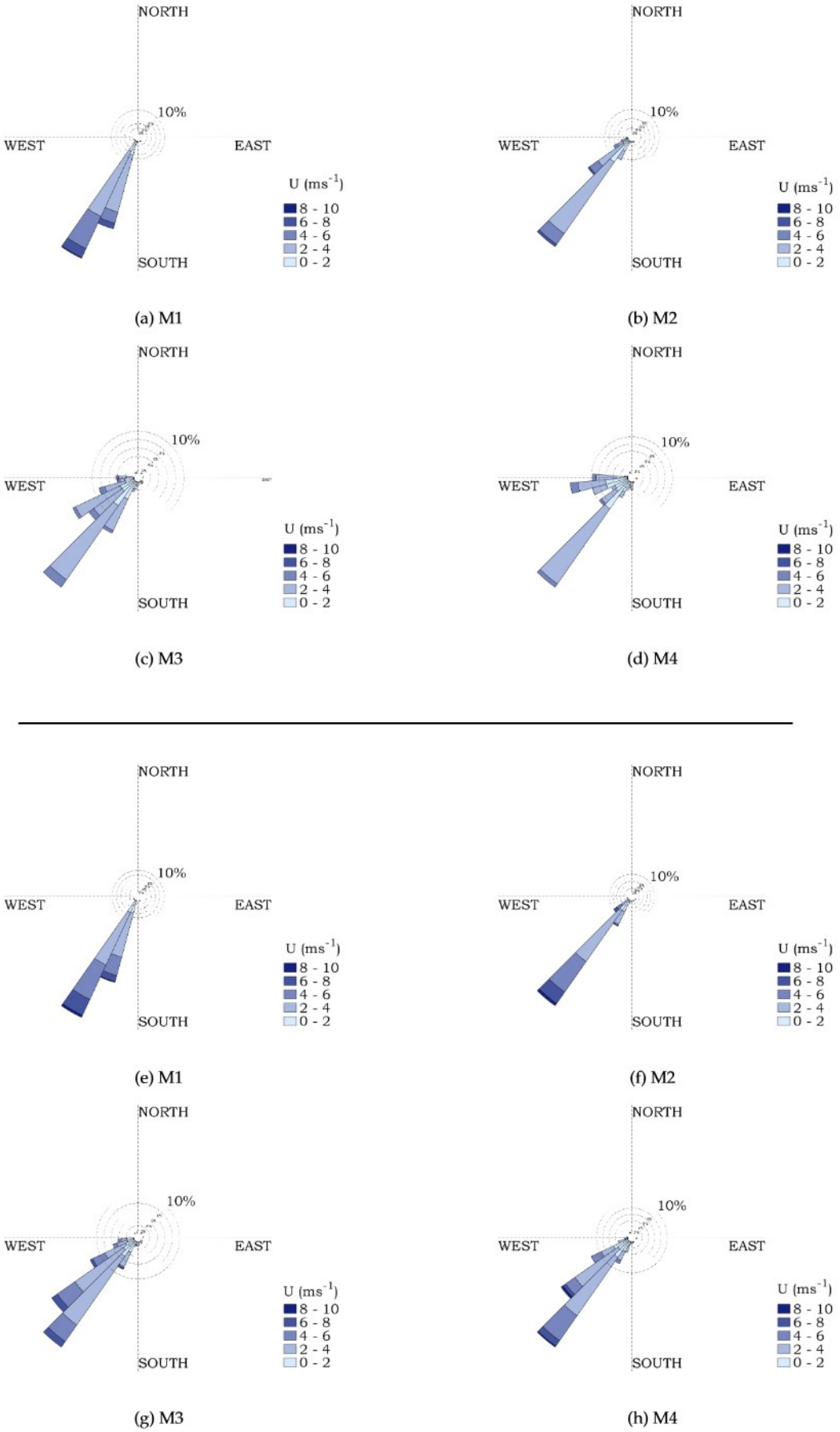

(a) M1 (b) M2

(c) M3 (d) M4

(e) M1 (f) M2

(g) M3 (h) M4

Fig. 4.11: Distribution of the horizontal wind direction at all wind masts M1 – M4 in 4 m height (top half: a – d) and 7 m heigth (bottom half: e – h). Measurement data from 2023-02-15 to 2023-05-31 filtered for times when wind direction at reference wind mast 1 aligns with measurement line (232°).

4.2.3 Wind Gust

To analyse the wind speed changes, wind gusts have been calculated according to the description in chapter 2.2.3 and are examined here for 10 minute resolved wind data. Figure 4.12 shows the 10-minute horizontal wind gust G in comparison to the mean wind speed for all four wind masts at both heights (4 m and 7 m, respectively).

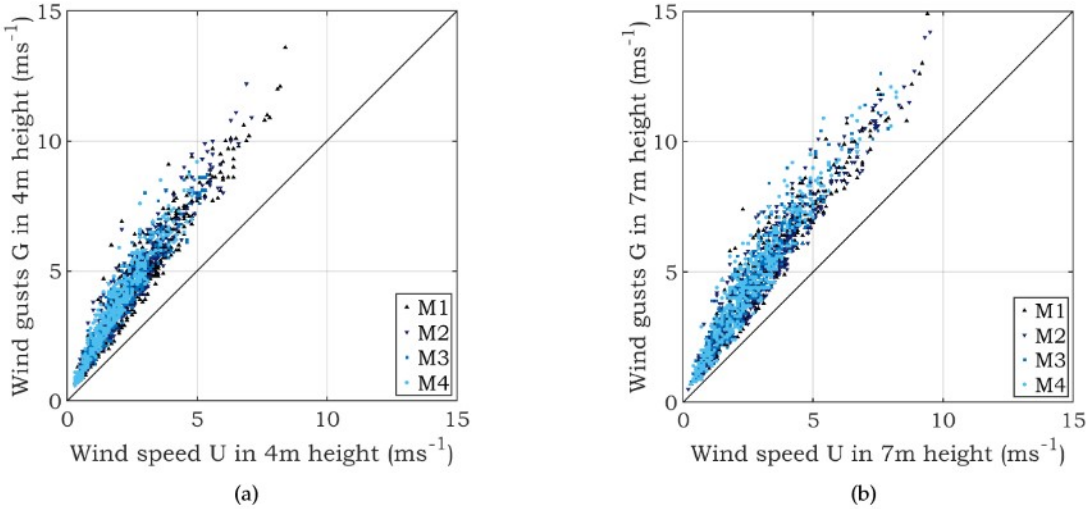

Fig. 4.12: Horizontal wind gust G versus horizontal wind speed U (10-minute resolution) for all four wind masts at a) 4 m height and b) 7 m height for the measured period of Dez. 7th 2022 to Jun. 1st 2023

Like expected and observed before in chapter 4.1.3, wind gusts are generally stronger than wind speeds. Their values increase as the wind speed increases, reaching maximum values of up to 14 ms^1 and 15 ms^1 for 4 m and 7 m height, respectively. On average, wind gusts are about 51 % to 71 % higher than the corresponding wind speed U.

Wind gusts are mainly evenly distributed along all wind masts and measurement heights. Only at wind mast 1 at 4 m height a slight shift towards stronger wind gusts could be observed. The effect is so minimal, however, that it can not be called significant and can very well be attributed to the typical variance in data, especially considering the reduced data set that was evaluated.

4.2.4 Turbulence Intensity

The frequency distribution of turbulence intensity I has been derived mirroring the methodology applied to wind speed distribution, just as it was done in the previous chapter 4.1.4. While there the frequency distribution of the turbulence intensity was discussed in regards to its change over different heights, in this chapter the horizontal change at a constant height will be discussed. Figure 4.13a and 4.13b shows the measured frequency distribution for all four wind masts at both heights (4 m and 7 m, respectively).

The trend shows an increase in turbulence intensity as the measurement locations move deeper into the heliostat field. Specifically, the average turbulence intensity at wind mast 1 in 4 m height of approx. 28.6 %, rises to 36.6 % at wind mast 4. This pattern is also reflected in the data measured at higher heights, although the absolute values are slightly lower due to the height variation and the corresponding decrease in turbulence intensity discussed previously. The maximum frequency distribution varies based on the location of the wind masts. At wind mast 1, the measurement data exhibit a maximum frequency distribution ranging around 50 % at a turbulence intensity of 20 %. Conversely, wind mast 4 shows a maximum frequency distribution ranging from 30 % to 50 % at a corresponding turbulence intensity of 30 %. The overall maximum turbulence intensity measured is 80 % at both height, with a similar frequency distribution, as said turbulence intensity very rarely occurs.

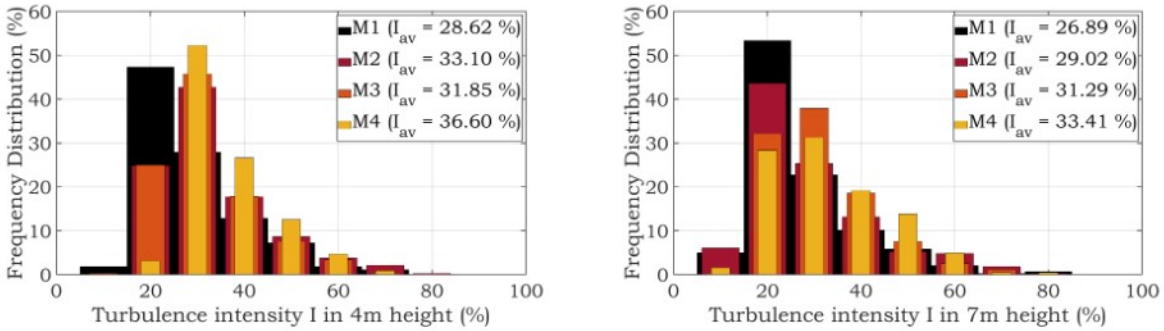

Fig. 4.13: Frequency distribution of the turbulence intensity I at all wind masts in a) 4 m and b) 7 m height during the measured period of 2023-02-15 to 2023-05-31.

In 4 m height, the average turbulence intensity at wind mast 3 is lower than at wind mast 2 and 4. This could be caused due to data logger problems at wind mast 3 which might have caused erroneous data that have not been excluded by the automatic quality control procedure.

4.2.5 Turbulence Spectra

With reference to the previous evaluation, it can be reasonably assumed, that the change of wind pattern progresses steadily over the course of the heliostat field. As such, the measurement data of the two wind masts most distant to each other should show the greatest difference from each other. Thus, or the sake of clarity, as all turbulence spectra have very similar graphs and consistent trends along the measurement line, only the turbulence spectra S_U and S_w of the outermost wind mast 1 and innermost wind mast 4 are compared in fig. 4.14 for each height that is applicable..

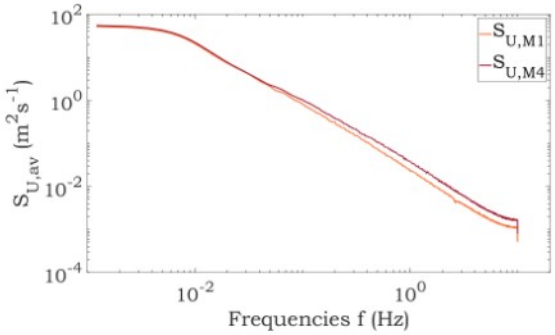

(a) cf. B.11 (annex)

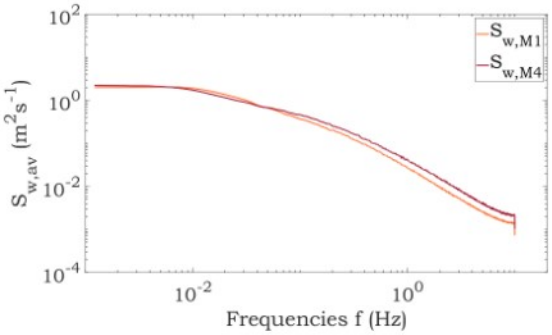

(b) cf. B.12 (annex)

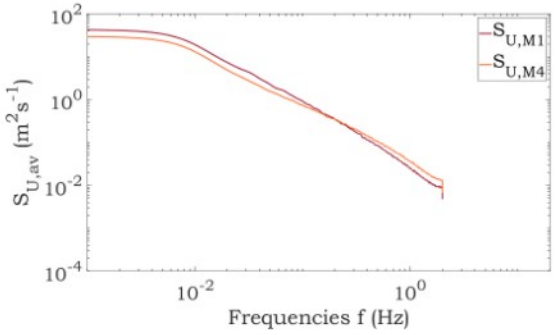

(c) cf. B.13 (annex)

Fig. 4.14: Averaged Turbulence Spectra S at wind mast 1 and wind mast 4 for the combined horizontal wind component S_U (left: a and c) and vertical wind component S_w (b) in different heights 7 m (top: a and b) and 4 m (c) for the measured period of 2023-02-15 to 2023-05-31.

If compared over the course of the heliostat field, the measurement data of the innermost wind masts tend to show generally higher frequency spectra than that of the outer ones at each height level. Up to a frequency of approx. 10^{-1}, both horizontal and vertical turbulence spectra at 7 m height show a good alignment with each other during the whole course of the field. For higher frequencies, however, the turbulence spectra measured within the field at M4 are higher, meaning that there are more turbulences with smaller vortexes inside the heliostat field than they are outside.This corresponds not only with the data observed so far, but also with the expectations of heliostats standing within the winds' direction and thus hindering its progression within the field by serving as obstacles.

This effect could also be observed by comparing the innermost and outermost turbulence spectra at a height of 4 m. In this height, though, the turbulence spectra at lower frequencies were visibly more pronounced at the outer wind mast 1, indicating that fewer larger vortexes reach the inside of the heliostat field.

4.3 Influence of Heliostat Tracking Status on Wind Pattern

To better understand how the orientation of the single heliostats influence the wind pattern within the heliostat field, the remaining data set from February 15th until May 31st 2023 with

wind directions between 227° and 237° are divided in two categories: a tracked heliostat field (the heliostats within the measurement line are not in stow position) and an untracked heliostat field (heliostats within the measurement line are considered to be in stow position). To define those two categories, the parameter TA (definition see chapter 3.3.3) has been calculated and summed up for all heliostats within the measurement line of the anemometers. In fig. 3.2 a sketch of the heliostat field has been shown in which the according heliostats are marked.

4.3.1 Influence on Wind Pattern

The direct relation between wind speed U and turbulence intensity I is evident in both horizontal and vertical directions and could be observed in the previous evaluation. The subsequent chapter will discuss these directions individually for a more detailed analysis with a special focus on the impact of the heliostat tracking status on the wind effects. The wind pattern (U, G, and I) are assessed concerning their variation across the horizontal extent of the heliostat field. The focus of this evaluation is to analyse a possible decrease or increase in U, G, and I dependent on the position of the different anemometers within the heliostat field and the heliostat tracking orientation. The measurement data is plotted against heliostat rows to visualize the spacial extent of the influence on wind pattern, with the anemometer data positioned at the wind masts location between heliostat rows.

The data is illustrated in figure 4.15 for two representative days, where the heliostats are in stow (April 15th 2023, see fig. 4.15a) and tracked (April 14th 2023, see fig. 4.15b), respectively. The data of the observed days is averaged between 9:00 h and 18:00 h. The therein depicted values are standardized to wind mast 1, positioned at the beginning of the measurement line in the south-west of the heliostat field. As mentioned before, in this analysis only data points with wind directions between 227 and 237° have been considered.

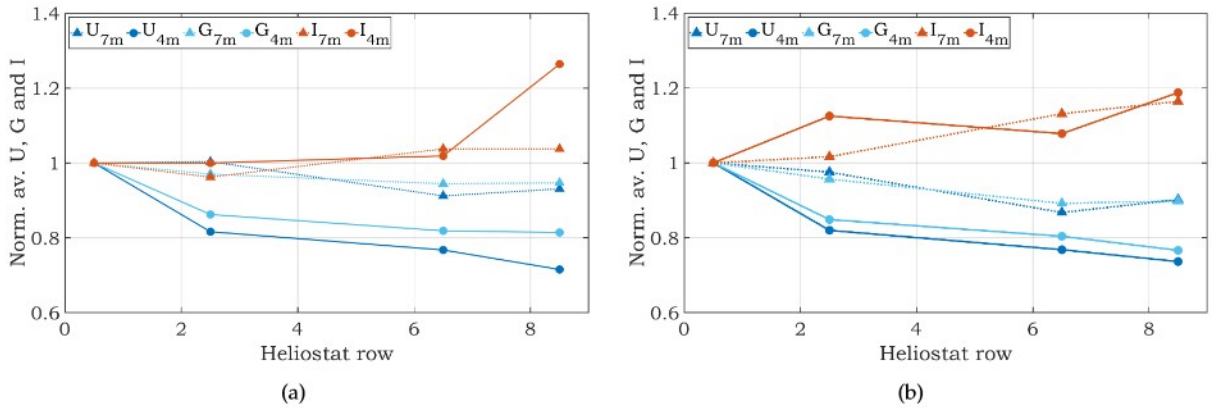

Fig. 4.15: Wind pattern (U, G, and I) measured by the anemometers at wind masts M1 to M4 in 4 m and 7 m height with a) heliostats in stow and b) tracked heliostats. The location of M1 to M4 is depicted by their positioning in-between heliostat rows. Data is averaged during the time frame selected to match the tracking status conditions (2023-04-15 09:00-18:00 (a) and 2023-04-14 09:00-18:00 (b)).

It can be seen that the wind speed and wind gust decrease over the course of the heliostat field while the turbulence intensity increases. This effect is less pronounced when the heliostats within the measurement line are in stow position (see fig. 4.15a) than when the heliostats are tracked (fig. 4.15b).

Comparing the data points during which the heliostats in the measurement line have been tracked (fig. 4.15b) to the data points when the heliostats have been in stow position (fig. 4.15a), it can be seen that the average wind speed and wind gust decrease for the latter case with the heliostat row in 4m, but showed a much lower decrease in 7m height above ground. Consistently, the turbulence intensity increased with the heliostat row in 4 m but showed a lower increase in 7m height. These results can be explained due to the fact, that the heliostat height in stow position is around 4 m while the heliostat reaches a maximum of 7 m height when it is oriented completely vertical.
Therefore, it can be seen in this analysis that there is a significant effect of the heliostat tracking on wind pattern within the heliostat field. This result also coincides with previous investigations [17].

Only the turbulence intensity in 7 m height varies noticeably from the expected and average behaviour with by showing an increase of over 20 % in fig. 4.15a between M3 and M4, and also depicting a slight increase between M2 and M3 while the heliostat field was tracked (fig. 4.15b). However, due to the fact that the data set was filtered previously for wind direction, the data quantity decreases noticeably, therefore making the results much more susceptible to variations.

4.3.2 Turbulence Spectra

During operation, heliostats oriented at various elevation angles obstruct airflow, leading to the generation of turbulent flow patterns at the edges of the mirror panel. These turbulent patterns result in fluctuating lift and drag forces in the wake region. Analysing turbulence spectra is crucial for understanding wind patterns and conditions, providing valuable insights into the fluctuating nature of wind speeds and turbulence levels over time.

Figure 4.16 shows the turbulence spectra between wind mast 1 (located outside the field) and wind mast 4 (innermost mast within the field) at heights of 4 m and 7 m. The data is filtered to isolate periods when the heliostat field is tracked or untracked to assess their respective impacts on the turbulence spectra. The limit fore the filter was based on the heliostats basic TA with an additional safety factor of 2 to also filter for very low tracking angles.

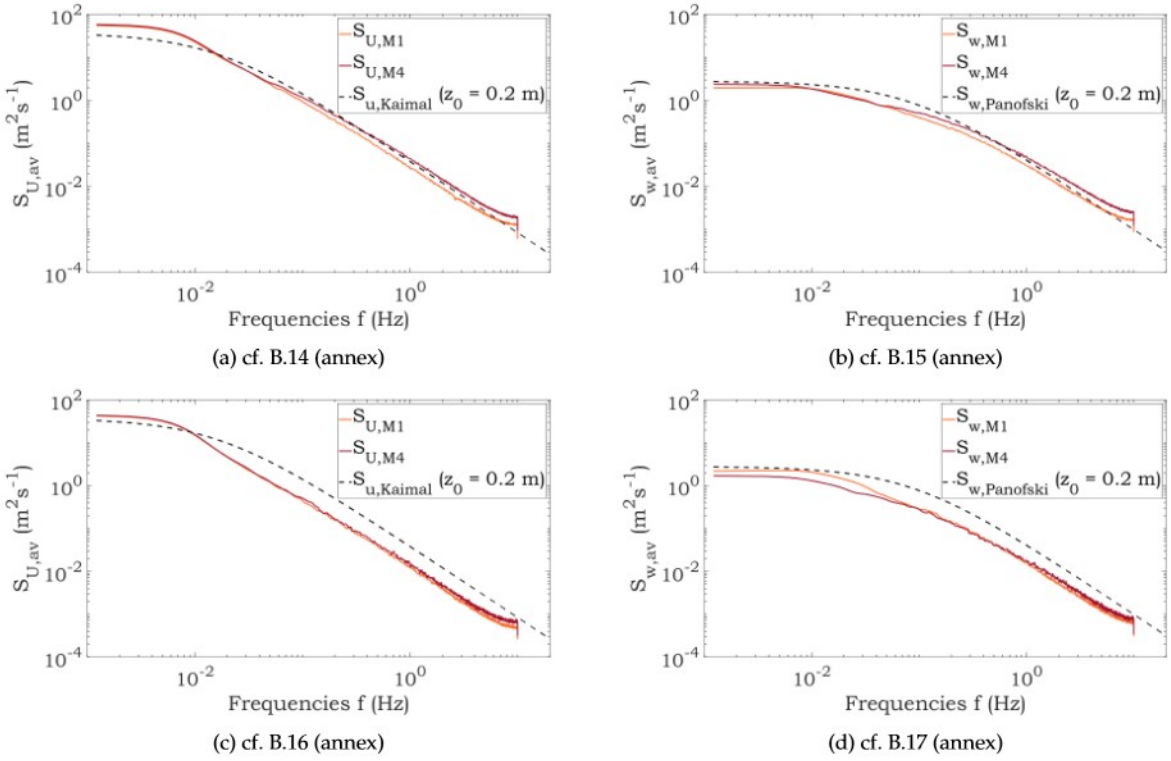

(a) cf. B.14 (annex)

(b) cf. B.15 (annex)

(c) cf. B.16 (annex)

(d) cf. B.17 (annex)

Fig. 4.16: Averaged Turbulence Spectra S at wind mast 1 and wind mast 4 in 7 m height for the combined horizontal wind component S_U (left: a and c) and vertical wind component S_w (right: b and d) for times with tracked (top: a and b) and untracked (bottom: c and d) heliostat field during the measured period of 2023-02-15 to 2023-05-31.

The turbulence spectra are notably higher during heliostat field operation times (see fig. 4.16, top) compared to when the heliostats are in stow (fig. 4.16, bottom). This trend is consistent across all wind components, although it is more pronounced in horizontal wind speeds (cf. fig. 4.16, left) than in the vertical wind component (fig. 4.16, right). Especially in the higher frequency range, starting at frequencies of 10^{-2} Hz, the turbulence spectrum is more pronounced under tracked field conditions compared to stow, indicating that fewer larger vortexes reach the inside of the heliostat field.

Further it can be seen, that the differences between the turbulence spectra measured at wind mast 4 and wind mast 1 are larger during time when the heliostats have been tracked than when they have been in stow position for frequencies above around 10^{-1} Hz. This indicates a change in vortex propagation in frequency ranges of the spectral gap as well as in the micro-meteorological spectrum caused by the tracked heliostats.

This corresponds not only with the data observed so far, but also with the expectations of heliostats standing within the winds' direction and thus hindering its progression within the field by serving as obstacles, just as it could be observed in the previous chapter 4.2.5.

4.3.3 Impact on Aerodynamic Effects

The influence of the heliostats' tracking status on wind pattern, particularly on wind speed U, was extensively examined using the impact analysis method outlined in chapter 3.3.3. It relates the change in the wind pattern normalized to the outermost wind mast 1 between two measurement points in the course of the field to the total target area of the heliostats over the observed path. The total target area, meaning the sum of all heliostats that lie in the measurement line between the two measurement points defined by the wind mast locations. Thus, the impact analysis calculates the percentage de- or increase of the observed wind parameter per square meter of the heliostats surface area that is targeted by the wind.

During the evaluation period analysed from February 15th to May 31st 2023, only data were considered in which the wind direction ranged between 227° and 237°, therefore aligning with the measurement line of the wind masts. Due to data gaps at wind mast 3, only the data from M1, M2, and M4 were evaluated during the following analysis. Since the measurement height of 4 m exactly matches the stow height of the heliostats, the measurement uncertainties would have been too large in this dataset. Therefore, data from anemometers at a height of 7 m were used for the evaluations.

Considering the direct proportionality of wind speed and wind load on the heliostat, the upcoming discussion will primarily focus on the parameter wind speed and how it is impacted by the heliostat target area – and with this by the tracking status.

The impact was calculated for every relevant timestamp, while differentiating between each heliostat regarding their individual tracking status. To gain better understanding of the underlying characteristics of the calculated impact, it was juxtaposed with individual parameters important for the calculation of the impact, mainly the target area as calculated in chapter 3.3.2 and 3.3.3 and the wind speed.

Figure 4.17 compares the results from the impact analysis carried out for wind speeds between 227° and 237° during the period of February 15th to May 31st 2023. It shows the impact Υ of the heliostats between M1 and M4 plotted in form of a scatter plot against the reference wind speed U at wind mast 1 in 7 m height. The shown data was assigned a third value in form of the measurement lines' target area TA_{ML}.

There is no direct correlation noticeable between U and Υ, the impact on the wind speed ranges from $+1\,\%m^{-2}$ to $-2.5\,\%m^{-2}$ irrespective of the corresponding wind speeds, which range from very low wind speeds near $0\,ms^{-1}$ to $10\,ms^{-1}$.

However, the TA_{ML} for each data points show a correlation with the impact. It can be seen that data points with higher target area TA_{ML} correspond to lower impacts. This correlation is expected, as it is a result of the mathematics behind the calculation of the impact where $\Upsilon \sim \frac{1}{TA}$.

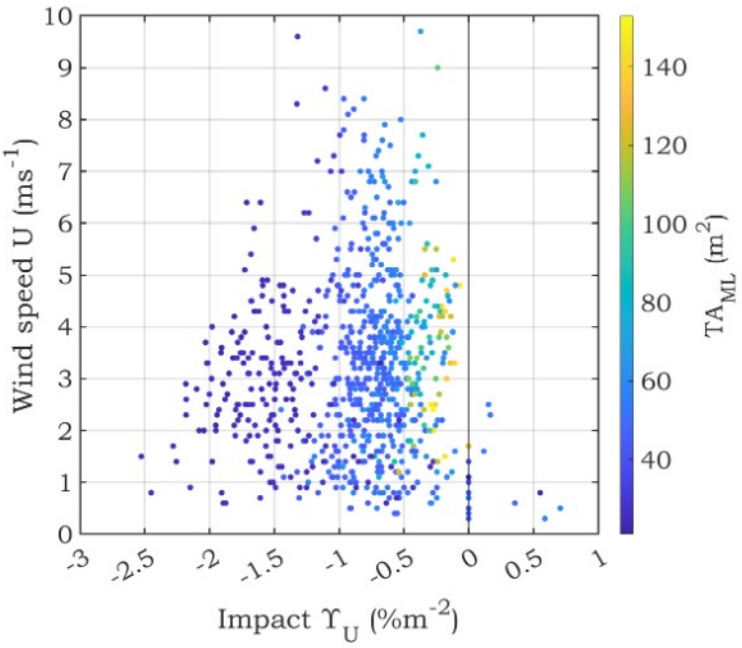

Fig. 4.17: Comparison of the results from the impact analysis carried out for wind directions between 227° and 237° during the measured period of 2023-02-15 to 2023-05-31. The plot shows the calculated impact Υ for the whole field between M1 and M4 juxtaposed with the reference wind speed U at wind mast 1 in 7 m height. The colorbar visualised the calculated heliostat target area at each data point.

For the evaluation visualised in fig. 4.17, all data points have been analysed regardless of the heliostats tracking status, since the status was already considered in the form of TA_{ML}.

In figure 4.18a the parameters U and TA_ML are exchanged and it shows the impact Υ compared against the total target area TA_{ML} with the wind speed U added as a third parameter in form of a value-assigned colour scheme. For completeness sake, the tracking status is not filtered in this specific evaluation and the complete data set is presented.

In fig. 4.18a it can be seen, that a cluster of data points lie within TA_{ML} of 22 m^2 and 27 m^2. These data points represent times when the heliostats within the measurement line have been in stow position and only the heliostat mounting structure (poles etc.) are considered within the TA_{ML}. The reason for this TA_{ML} range is that for some data points, single heliostats have been not completely in stow position (azimuth angle equal to 0°), but their azimuth angles ranged between 1-2°. Data points with TA_{ML} lower than 27 m^2 are therefore from now on excluded from the analysis to prevent a falsification of the results and also because the actual goal is to analyse the *tracking* impact, which is why stowed heliostats are less relevant for this specific evaluation.

Further, data points with wind speeds of less than 3 ms^{-1} have been excluded in fig. 4.18b. This has been done because the measurement accuracy for low wind speeds decreases according to the specifications of the anemometer and also because these low wind speeds are less relevant for this analysis.

The comparison shows the expected multiplicative inverse correlation between the two parameters Υ and TA_{ML}. The correlation can roughly be approximated by

$$TA_{ML} = -\frac{1}{20 \cdot (\Upsilon - 0.1)} + 12 \tag{33}$$

as a trend line that is also shown in fig. 4.18b. Consequently, the (absolute) impact is lower for higher target areas, while lower target areas exhibit higher (absolute) impacts.

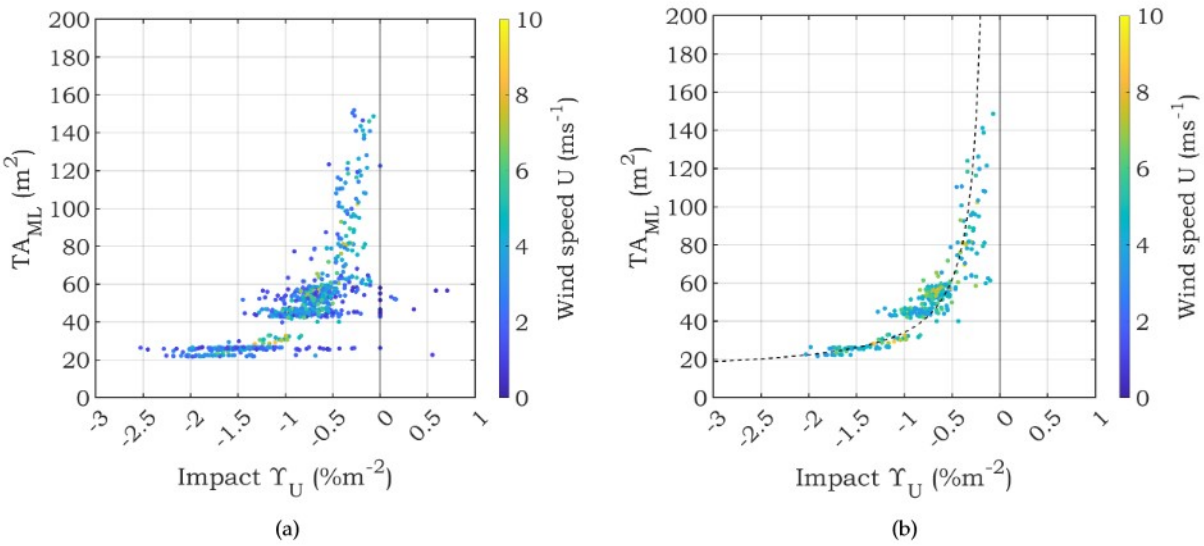

Fig. 4.18: Comparison of the results from the impact analysis carried out for wind directions between 227° and 237° during the measured period of 2023-02-15 to 2023-05-31. The plot shows the calculated impact Υ for the heliostats within the measurement line between M1 and M4 juxtaposed with the calculated heliostat target area TA_{ML}. The parameter of the reference wind speed U at wind mast 1 in 7 m height is added in form of the assigned colour. Fig. 4.18a shows the complete data set while in 4.18b, data points with TA_{ML} of less than 22 m^{-2} and U less than 3 ms^{-1} are excluded.

During the evaluation period from February 15th to May 31st, 2023, only data falling within the wind direction range of 227° to 237° at reference wind mast 1 at a height of 7 m were considered, aligning with the measurement line of the wind masts. For the final presentation of the summarized results, stow periods and times with wind speeds < 3 ms^{-1} were excluded due to their detrimental influence on the impact analysis accuracy.

The evaluation of the impact analysis of the heliostats on wind pattern was not only carried out along the whole measurement line between M1 and M4, but also for the measurements at M2 and M3. Due to data gaps at wind mast 3, the analysis focused solely on data from M1, M2, and M4 (equalling heliostat rows 0.5, 2.5 and 8.5).

In fig. 4.19, the impact of the heliostat field on wind speed and turbulence intensity versus the heliostat row is shown. It can be seen that the impact on U and I behave in a way contrasting each other. The average impact on wind speed Υ_U is -0.7 %m^{-2} over the course of the whole measurement line within the heliostat field, which means that the wind speed decreases on

average by 0.7 % per square meter of heliostat surface area. At the same time, the impact Υ_I on turbulence intensity I is on average 0.75 %m^{-2}.

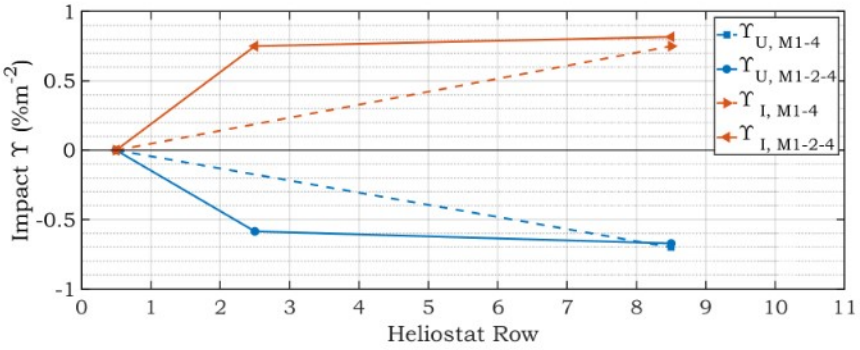

Fig. 4.19: Comparison of the results from the impact analysis carried out for wind directions between 227° and 237° during the measured period of 2023-02-15 to 2023-05-31. The plot shows the heliostats' impact on U and I over the course the heliostat rows for data with $U > 3\,\mathrm{ms}^{-1}$ and $TA_{ML} > 22\,\mathrm{m}^{-2}$.

For both cases it can be seen that the largest share of the change in wind pattern is taking place within the first two heliostat rows between wind mast 1 and wind mast 2, indicating that the impact of heliostats on wind pattern is not distributed evenly throughout the heliostat field. It rather seems as if the first heliostat rows act as a wind fence by being responsible for the majority of the influence on wind pattern.

These findings could also be reproduced in wind tunnel studies as carried out by Peterka et al [13]. There, the influence of fences located not only on the edges of the field but also within was investigated. The study showed that mean wind loads on heliostats could be reduced up to 30 % of the loads of isolated heliostats. [13] In a wind tunnel experiment conducted by Emes et al. in a study in 2021, it was shown that perimeter mesh fences could reduce peak loads by as much as 50 % [15]. The study emphasized the necessity of conducting a thorough analysis on an actual heliostat field rather than relying on a scaled-down wind tunnel model [15].

4.4 Comparison of Anemometer and LiDAR Measurements

In the last step, the 2D measurement data of the two LiDAR scanners are evaluated with regard to the anemometer measurements. The LiDAR data has been compared to the anemometer measurements at wind mast 1 (outside of heliostat field) and in 10 m height to validate the plausibility of the LiDAR data set (cf. chapter 3.4). In chapter 4.4.1, the averaged time periods during which the heliostat field has been tracked within the measurement line of the anemometers as well as the averaged stow times are analysed to observe possible 2D effects of the heliostat field on wind pattern. Finally, in chapter 4.4.2 the LiDAR data is discussed in selected two-dimensional plots.

4.4.1 Tracking Influence on Wind Pattern of LiDAR Data

As this thesis aims to evaluate the tracking impact of heliostats, times are selected when winds originate from the south-west, aligning with the measurement line (wind directions between 227° and 237°). The wind masts are positioned between different heliostat rows, representing the heliostat field configuration. The data set is divided into the two specific conditions of the heliostat field, tracked and in stow. The distinction between a tracked and stowed heliostat field was made by dividing the data set in accumulated TA_{ML} of more or less than 2 times it's TA_B, a value that was found to be reliable by extensive evaluation of the data.

In the comparison between LiDAR and anemometer data, the grid points nearest to the wind masts are identified. Said grid points are documented in Table 4.6. Averages are then calculated for these listed grid points to facilitate further data processing in the context of comparison with anemometer data. It's worth noting that for wind mast 1, the actual grid points are approximately 6 meters away from the physical wind mast due to data disturbances caused by the mast's presence at its exact location.

Table 4.6: Grid points nearest the four wind masts.

mast 1	mast 2	mast 3	mast 4
57, 84, 85	314, 315, 362, 363	978, 979, 1036	1235, 1272, 1273

Figure 4.20 illustrates the normalized horizontal wind speed across the heliostat field relative to wind mast 1. The data includes anemometer measurements from all four wind masts at heights of 4 m and 7 m, while for LiDAR data collected at 10 m height, grid points representing the wind mast positions are selected.

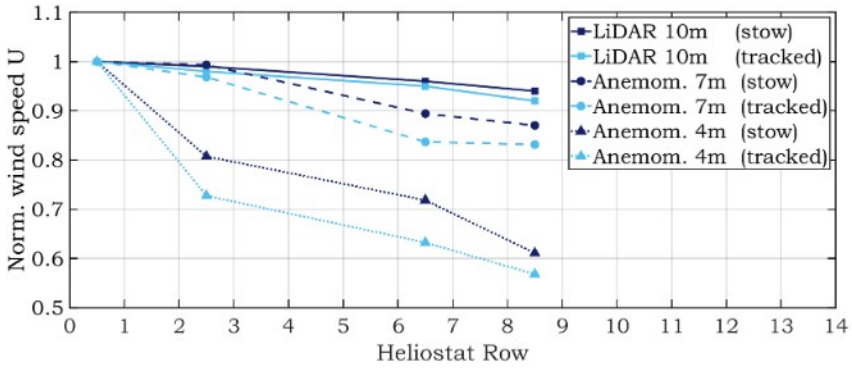

Fig. 4.20: To wind mast 1 normalized horizontal wind speed over the heliostat field, represented in form of heliostat rows. The wind masts are positioned in-between rows. Data given for wind masts 1 – 4 in 4 m and 7 m height with LiDAR data matching the masts' positions in 10 m height. The complete data set between 2023-02-15 to 2023-05-31 was allocated to tracked and stow conditions and then each set averaged.

The figure clearly shows a reduction in wind speed across the heliostat field. LiDAR data indicates a decrease of approximately 6 % in stow and 8 % when the heliostat field is tracked, whereas anemometer readings show wind speed reductions of about 13 % and 17 % at a height of 7 m depending on the heliostats tracking status. In 4 m height the wind speed decreases by about 39 % for stow condition and up to 42 % when the heliostat field is tracked. The heliostat tracking status has a pronounced impact on the progression of wind speed within the heliostat field.

It can be seen that the variation in wind speed U across the heliostat field is less pronounced above the upper edge of the heliostats (7 m if the heliostat is oriented vertically) than in lower heights above ground. As a result, the wind deceleration is generally less pronounced in LiDAR data, which are performed in a height of around 10 m above ground, showing a more gradual decline. This can also generally be attributed to fewer obstacles impeding airflow at higher heights above the ground, leading to smoother wind speed reductions over the area.

4.4.2 Two-Dimensional Analysis of the LiDAR Data

The following subchapter discusses the change in wind pattern using LiDAR data to map wind speed changes across the entire field in two dimensions. This approach enables the observation of the phenomenon not only during south-west winds, as previously analysed, but also during west and north-west winds. In figure 4.21 the according average horizontal wind speed in 10m height above ground derived for the LiDAR data for April 13th at 15:40 h can be seen. At this time, the wind direction was prevailingly from 251°. It can be seen that the average wind speed was highest in the south-western part of the heliostat field and lower in the north-eastern part. A gradual decrease in wind speed with respect along the wind direction axis can be observed.

Figure 4.22 shows the tracking status of the heliostats at the same time, visualised in form of the target area $TA_{\%}$ attributed to the individual heliostats in form of the color scheme. It can be seen that the tracking status of the heliostats in fig. 4.22 aligns with the wind speed changes observed in the heliostat field in fig. 4.21. The heliostat surface areas mostly targeted by the wind are positioned at the south-western side of the heliostat field, which is the area in which the biggest decrease of U can be seen in fig. 4.21.

In the field depicted in 4.21, two noticeable data areas of low wind speeds are evident – one near wind mast 1 and another on the south-eastern side of the field (see dark blue areas in fig. 4.21). These phenomena occur due to obstructions in the path of LiDAR scanner 1, located north-east of the heliostat field, leading to incomplete measurements by this scanner. Consequently, only the data from scanner 2 remains available for wind data calculations. Because the wind direction aligns nearly perpendicularly to the beam scanner from scanner 1, this situation results in very low radial wind speeds in the collected data.

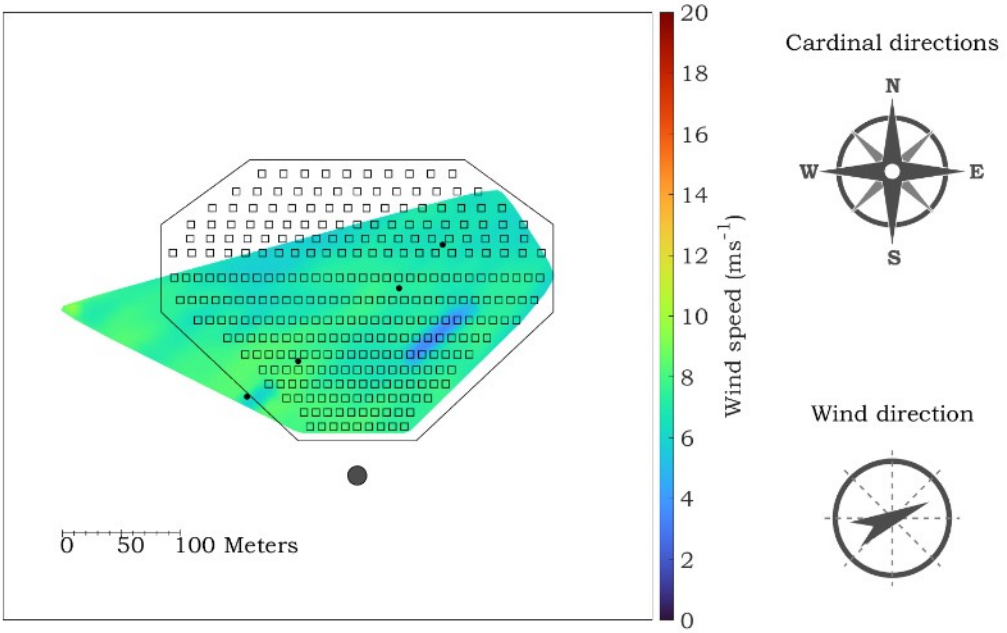

Fig. 4.21: Exemplary two-dimensional field plot showing LiDAR data for a operational day with south-western wind (2023-04-13 15:40 h). The target area *TA* as colour of the surface plot, showing that the tracked heliostats work as a wind fence over the course of the field along the wind direction of 251°.

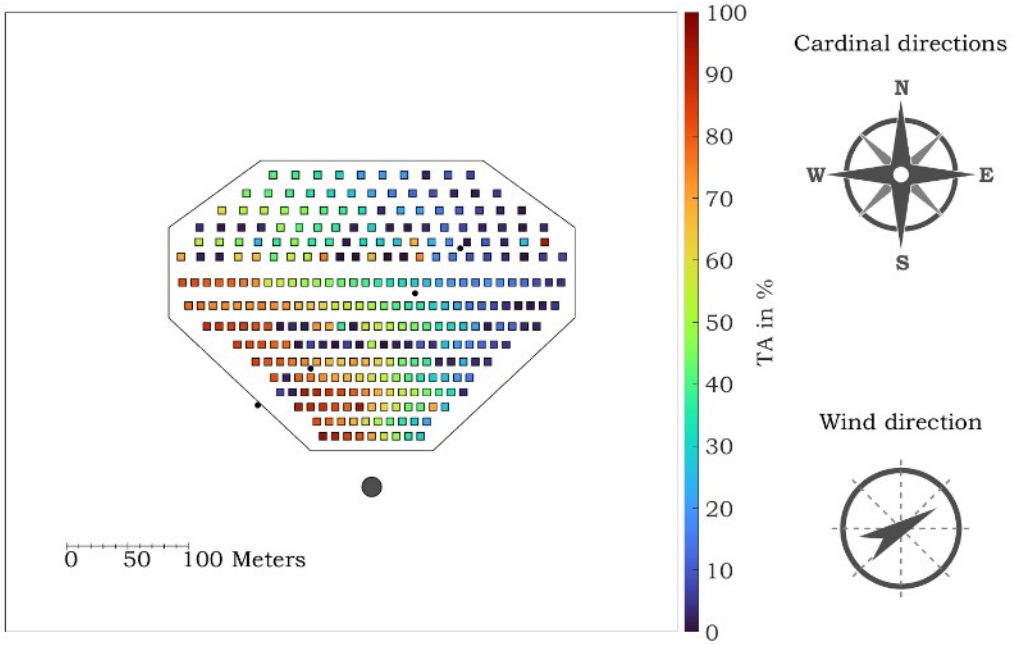

Fig. 4.22: Exemplary two-dimensional field plot showing LiDAR data for a operational day with western wind (2023-04-13 15:40 h). The wind speed is visualised as the colour of the surface plot, showing the decrease of the wind speed over the course of the field along the wind direction of 251°.

Figure 4.23 shows the two-dimensional plotted LiDAR data for May 26th 2023 at 14:30 h when the prevailing wind direction was 89° (eastern winds). It can be seen, that U increases from the north-east to the south-west of the heliostat field.

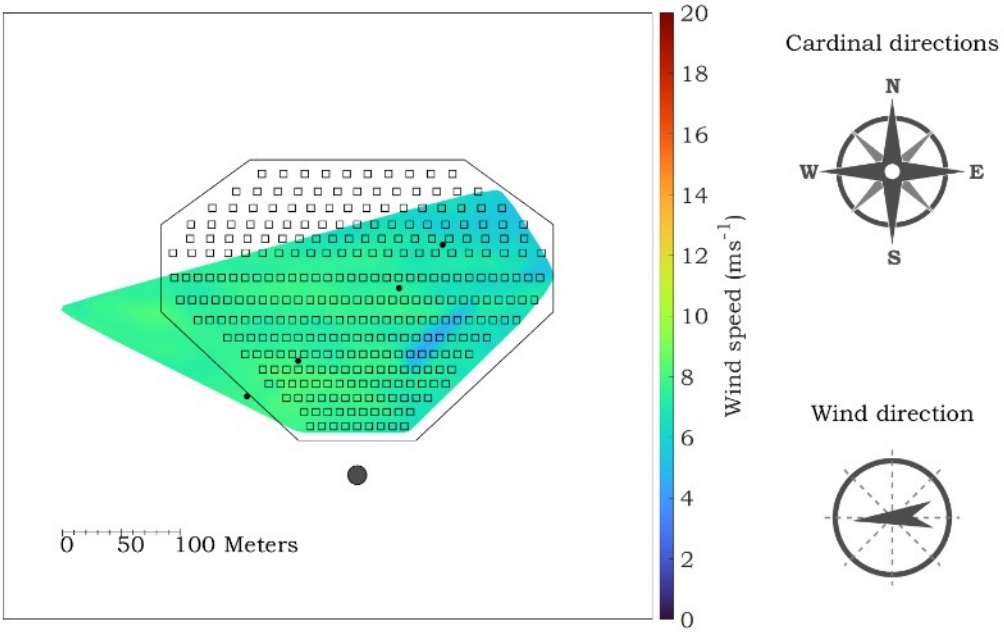

Fig. 4.23: Exemplary two-dimensional field plot showing LiDAR data for a day with east wind (2023-05-26 14:30 h). The wind speed is shown via the colour of the surface plot, visualising the wind fencing effect with the unexpectedly low wind speed on the eastern side of the field with its gradual increase over the course of the field.

Examining the surrounding environment reveals a probable explanation for this phenomenon. The reduced wind speed during east winds is likely attributed to the presence of the Parabolic Trough DISS situated directly to the east of the CESA-I heliostat field (see fig. 4.24). This structure replicates the wind hindrance and velocity reduction effect observed at the outset of the heliostat field under various wind directions.

Fig. 4.24: Picture of the Parabolic Trough DISS at CIEMAT'S PSA. The tower of the CESA-I power plant can be seen in the background [73].

The wind shadow effect attributed to an obstacle can be substantiated by instances of southern winds. Figure 4.25 shows the 2D wind speed on February 23rd 2023 at 15:10 h with a wind direction of 205° (southern wind). It can be seen in fig. 4.25 that the solar tower of the CESA-1 facility casts a wind shadow on the heliostat field, confirming the observed effect.

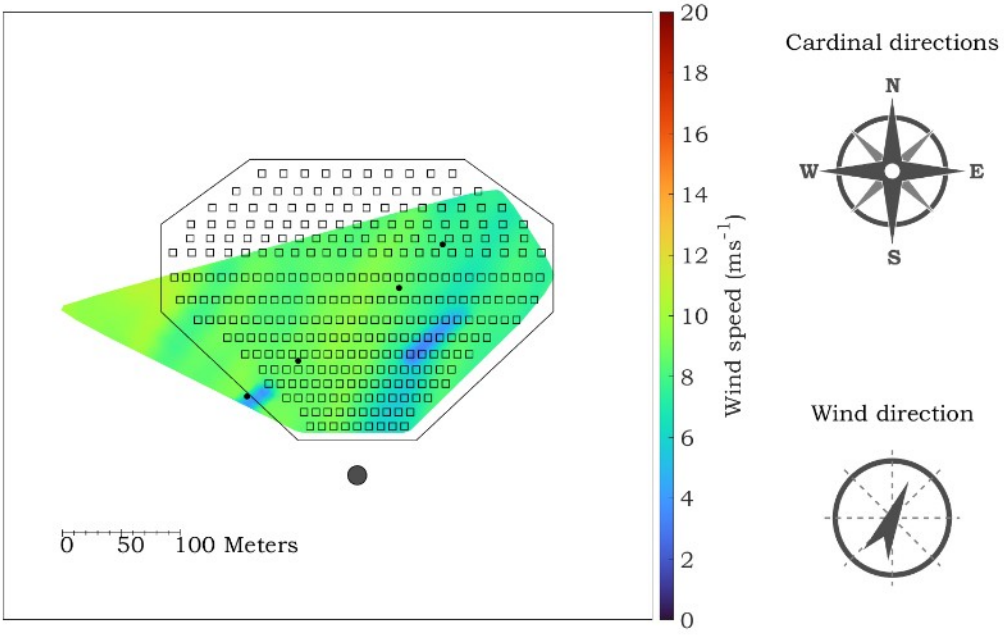

Fig. 4.25: Exemplary two-dimensional field plot showing LiDAR data for a day with south wind (2023-02-23 15:10 h). The average wind speed is rather high for most of the field, excluding a small but longish strip on the right half of the field that aligns with the wind direction. The effect is caused by the solar tower shielding the heliostat field.

The length of the wind shadow also serves as an indicator of the obstacle's height. While the solar tower produces a substantial impact due to its considerable height, the parabolic trough stands at only 6 meters tall. Despite this being nearly the tracked heliostats height, the parabolic trough is located further away. This results in a diminishing effect, allowing wind speeds to gradually recover towards the west.

5 Conclusion

In concluding the thesis, this chapter revisits and assesses the conducted research, offering a comprehensive overview of the obtained results. It also discusses the limitations encountered during the study and presents recommendations for future research.

5.1 Summary

This master's thesis conducted a comprehensive analysis of wind speed measurement data in a heliostat field of a solar tower power plant. During the measurement campaign between February 15th and May 31st 2023, wind measurements were carried out using nine temporally high resolved ultrasonic anemometers, measuring with 4 Hz or 20 Hz and two or three wind components, respectively. The anemometers were distributed along a measurement line of four wind masts across the heliostat field in south-western direction in two different heights of 4 m and 7 m. At the wind mast 1 located outside of the heliostat field, an additional anemometer in 10 m height above ground has been installed. Simultaneously, two LiDAR scanners measured in two dimensions the wind speed at 10 m height above ground with a spacial resolution of around 3 m by scanning over the heliostat field. All data set have been also downsampled to 10 min averages.

The data have been preprocessed to ensure the quality and completeness of the data and to validate it, which was a prerequisite for further data analysis. In this context, the wind direction of the anemometer data were validated. Further, the area of each heliostat within the field as a function of the orientation of the heliostat perpendicular to the wind was derived. With this parameter, the impact of the heliostat orientation on wind pattern within the heliostat filed could be analysed. Additionally, the two-dimensional LiDAR wind speed measurements have been compared to the anemometer data at the LiDAR grid points in which the according wind masts have been located.

The study then investigated various influencing factors and their effects on wind behaviour. The analysis algorithms and methods were performed using the programming environment Matlab, resulting in the development of over several thousand lines of program code. Specifically, general wind pattern like the diurnal course, frequency distribution, wind gusts, wind turbulence intensity and wind roses were implemented and calculated using Matlab. Additionally, the turbulence spectra of the wind components were evaluated. A detailed impact analysis was carried out, where the impact of the heliostats tracking status on wind pattern was analysed. Finally, the anemometer measurements were compared to the LiDAR data.

The main wind direction at the test site of the measurement campaign is south-west, aligning with the south-western measurement line in which the anemometer wind masts are located. The second prevailing wind direction are easterly wind. Pronounced diurnal courses were observed at all wind masts with lower wind speeds during the night and higher average wine

speeds during day time. During the evaluation, trends in wind pattern could be observed in both vertical direction caused by different heights as well as horizontally over the heliostat field. The average wind speed outside of the heliostat field has been 3.26 ms^{-1} in 10 m height above ground, 3.06 ms^{-1} in 7 m and 2.63 ms^{-1} in 4 m between February 15th and May 31, 2023. Considering only time periods with south-westerly winds, the average measured horizontal wind speed at wind mast 1 (outside of the heliostat field in the South-West) accounted for 2.95 ms^{-1} and 3.26 ms^{-1} in 4 m and 7 m height, respectively. The average wind speed decreased to 1.86 ms^{-1} in 4 m and 2.69 ms^{-1} in 7 m height above ground at wind mast 4, which was the wind mast located within the heliostat field in the North-East.
Wind gusts show a similar behaviour at all wind masts and heights above ground and are on average approximately 60 % higher than the corresponding average wind speeds.
The average turbulence intensities have been measured on wind mast 1 between February 15th and May 31 2023, to be 25.81 %, 26.89 % and 28.14 % in 10 m, 7 m and 4 m height above ground, respectively. Considering only time periods with south-westerly winds, the average turbulence intensities have been 26.89 % in 7 m and 28.14 % in 4 m height at wind mast 1. In the inner heliostat field at wind mast 4, the average turbulence intensity increased to 31.15 % and 34.01 % in 7 m and 4 m height, respectively. While the average wind speed decreases both with lower heights above ground and within the heliostat field, the average turbulence intensity increases, respectively.
Analysing the turbulence spectra at each wind mast, it could be found that the turbulence spectra over all measured frequencies are higher at both wind mast 1 and wind mast 4 during time periods when the heliostats within the measurement line have been tracking the sun compared to when they have been in stow position. It can also be seen that the difference between the turbulence spectra measured at wind mast 4 and wind mast 1 for frequencies above about 10^{-1} is greater when the heliostats were tracked than when they were in the rest position. This indicates a change in the vortex propagation in frequency ranges of the spectral gap as well as in the micro-meteorological spectrum caused by the tracked heliostats.

Considering the heliostat tracking orientation, is has been found that decrease of the average wind speed and the increase of the average turbulence intensity is dependent on the tracking status of the heliostats within the wind mast measurement line. One exemplary day on which the heliostats within the measurement line were in stow position and one when the heliostats have been tracking the sun have been compared. It could be seen that the average wind speed and gust decreased with heliostat row in 4 m while in 7 m the decrease was less pronounced when the heliostats have been in stow position. Consecutively, the average turbulence intensity increased with heliostat row in 4 m, while the increase was relatively less in 7 m height. On the contrary, both the decrease in wind speed and gust as well as the increase in turbulence intensity with heliostat row have been present in a much more pronounced manner also in 7 m height above ground on the exemplary day on which the heliostats have been tracked. A detailed analysis reveals that the major impact of the tracked heliostats on wind pattern is concentrated on the first three heliostat rows, indicating that the first rows of heliostats act like wind fences

and reduce wind loads on heliostats in the inner rows of the field.

The comparison of the LiDAR and anemometer measurements showed a good alignment between both data sets. Looking at one exemplary time when the heliostat field has been partly tracked, a good agreement between the measured two-dimensional wind speed over the complete heliostat field derived by the two LiDAR scanners and the expected wind pattern over the heliostat field could be found. Additionally, wind shading effects from surrounding structures like the nearby solar trough installation or the solar tower could be visualized with the analysis of the two-dimensional LiDAR data set. The LiDAR data therefore confirm the fence-effect by surrounding obstacles which reduce wind speed within the heliostat field.

5.2 Outlook

This thesis contributes to understanding the complex dynamics of wind flows in heliostat fields of solar tower power plants and provides approaches for optimizing heliostat design to possibly save investment costs. The findings of this thesis will be provided to an associated project partner of DLR who is performing concepts and designs of structures, like concentrating solar power heliostats. Using the achieved results, the heliostat design could be optimized to adapt for possible lower average wind speeds and therefore lower wind loads in the inner heliostat field in comparison to the outer heliostat field, considering also the analysed turbulence conditions within the heliostat field. The analysis of spatially and temporally resolved wind measurements within a real heliostat field based on several months of wind measurements using ultrasonic anemometers and innovative LiDAR scanners makes it possible to estimate the cost-saving potential of wind-optimized heliostats. Since the measurement campaign presented here was carried out in a rather small CESA-1 heliostat field at CIEMAT's Plataforma Solar de Almeria, it is conceivable that a further measurement campaign could be carried out in a larger heliostat field in the future. In addition, an analysis of the wind load distribution is also interesting for other solar technologies. For example, in the field of agrivoltaics (term for the simultaneous use of land for agriculture and solar power). In agrivoltaic systems in which high-mounted photovoltaic modules are installed over an agricultural area, high investments due to the usage of steel for the mounting structure influence the overall profitability of such systems. The knowledge of wind loads in different parts of such an agrivoltaic power plant could therefore also reduce investment costs and promote the implementation of agrivoltaic solutions within the solar energy market. Last but not least, it is planned to publish the acquired results in a journal paper. Further, it is planned to present the results at the international conference of concentrating solar technologies SolarPACES.

References

[1] IRENA. *Rebewable Energy Statistics 2019*. Abu Dhabi, 2019.

[2] Sankalp Kumar, Aviral Agarwal, and Anil Kumar. "Financial viability assessment of concentrated solar power technologies under Indian climatic conditions". In: *Sustainable Energy Technologies and Assessments* 43 (2021), p. 100928. ISSN: 22131388. DOI: 10.1016/j.seta.2020.100928.

[3] Kasra Mohammadi and Hossein Khorasanizadeh. "The potential and deployment viability of concentrated solar power (CSP) in Iran". In: *Energy Strategy Reviews* 24 (2019), pp. 358–369. ISSN: 2211467X. DOI: 10.1016/j.esr.2019.04.008.

[4] Rahul Bhattacharjee and Subhadeep Bhattacharjee. "Viability of a concentrated solar power system in a low sun belt prefecture". In: *Frontiers in Energy* 14.4 (2020), pp. 850–866. ISSN: 2095-1701. DOI: 10.1007/s11708-020-0664-5.

[5] Mark Mehos et al. *Concentrating Solar Power Gen3 Demonstration Roadmap*. Ed. by National Renewable Energy Labaoratory. Golden, CO, 2017. DOI: 10.2172/1338899.

[6] Peter Heller, ed. *The performance of concentrated solar power (CSP) systems: Analysis, measurement and assessment*. Woodhead Publishing series in energy. Duxford, Cambridge, MA, and Kidlington: Elsevier, 2017. ISBN: 978-0-08-100447-0. URL: http://www.sciencedirect.com/science/book/9780081004470.

[7] O. Achkari and A. El Fadar. "Latest developments on TES and CSP technologies – Energy and environmental issues, applications and research trends". In: *Applied Thermal Engineering* 167 (2020), p. 114806. ISSN: 13594311. DOI: 10.1016/j.applthermaleng.2019.114806.

[8] Wenjin Ding and Thomas Bauer. "Progress in Research and Development of Molten Chloride Salt Technology for Next Generation Concentrated Solar Power Plants". In: *Engineering* 7.3 (2021), pp. 334–347. ISSN: 20958099. DOI: 10.1016/j.eng.2020.06.027.

[9] Ming Liu et al. "Review on concentrating solar power plants and new developments in high temperature thermal energy storage technologies". In: *Renewable and Sustainable Energy Reviews* 53 (2016), pp. 1411–1432. ISSN: 1364-0321. DOI: 10.1016/j.rser.2015.09.026.

[10] Caitlin Murphy et al. *The Potential Role of Concentrating Solar Power within the Context of DOE's 2030 Solar Cost Targets*. 2019. DOI: 10.2172/1491726.

[11] A. Pfahl, M. Buselmeier, and M. Zaschke. "Wind loads on heliostats and photovoltaic trackers of various aspect ratios". In: *Solar Energy* 85.9 (2011), pp. 2185–2201. ISSN: 0038092X. DOI: 10.1016/j.solener.2011.06.006.

[12] Andreas Pfahl. "Wind Loads on Heliostats and Photovoltaic Trackers". Dissertation. Eindhoven: Technische Universiteit Eindhoven, 2018.

[13] J. A. Peterka et al. *Wind load reduction for heliostats*. US, 1986. DOI: 10.2172/5556580.

[14] Kristina Blume. "Acceptance Test for Heliostats to Quantify Wind-Induced Tracking Deviations". Dissertation. Aachen: Rheinisch-Westfälische Technische Hochschule Aachen, 2022.

[15] Matthew Emes et al. "A review of static and dynamic heliostat wind loads". In: *Solar Energy* 225 (2021), pp. 60–82. ISSN: 0038092X. DOI: 10.1016/j.solener.2021.07.014.

[16] Azadeh Jafari et al. "Wire mesh fences for manipulation of turbulence energy spectrum". In: *Experiments in Fluids* 62.2 (2021). ISSN: 0723-4864. DOI: 10.1007/s00348-021-03133-7.

[17] J. Sment and C. K. Ho. "Wind Patterns over a Heliostat Field". In: *Energy Procedia* 49 (2014), pp. 229–238. ISSN: 18766102. DOI: 10.1016/j.egypro.2014.03.025.

[18] IRENA. *Rebewable Power Generation Costs in 2020*. Abu Dhabi, 2021.

[19] Thomas Mancini, ed. *Catalog of Solar Heliostats*. 2000.

[20] Scott Jones et al. *Heliostat cost reduction study*. 2007. DOI: 10.2172/912923.

[21] Rakesh Singhai, Harender Sinhmar, and N. D. Banker. "Effect of Aspect Ratio of Heliostat on Cost of Energy from Solar Power Tower Plants". In: *Arabian Journal for Science and Engineering* 45.2 (2020), pp. 877–890. ISSN: 2193-567X. DOI: 10.1007/s13369-019-04105-0.

[22] Thomas Mancini et al. *Power Tower Technology Roadmap and cost reduction plan*. 2011. DOI: 10.2172/1011644.

[23] H. L. Zhang et al. "Concentrated solar power plants: Review and design methodology". In: *Renewable and Sustainable Energy Reviews* 22 (2013), pp. 466–481. ISSN: 1364-0321. DOI: 10.1016/j.rser.2013.01.032.

[24] R. P. Merchán et al. "High temperature central tower plants for concentrated solar power: 2021 overview". In: *Renewable and Sustainable Energy Reviews* 155 (2022), p. 111828. ISSN: 1364-0321. DOI: 10.1016/j.rser.2021.111828.

[25] Maria Simona Răboacă et al. "Concentrating Solar Power Technologies". In: *Energies* 12.6 (2019), p. 1048. DOI: 10.3390/en12061048.

[26] Abdul Hai Alami et al. "Concentrating solar power (CSP) technologies: Status and analysis". In: *International Journal of Thermofluids* 18 (2023), p. 100340. ISSN: 26662027. DOI: 10.1016/j.ijft.2023.100340.

[27] Scott Madden. *Revisiting the California Duck Curve: An Exploration of Its Existence, Impact, and Migration Potential*. 2016. URL: https://www.solarwakeup.com/wp-content/uploads/2016/10/Revisiting-the-Duck-Curve_Article.pdf.

[28] Hiyam Farhat and Coriolano Salvini. "New lifing criterion for land-based gas turbines in flexible operation mode". In: *Energy Reports* 8 (2022), pp. 379–385. ISSN: 23524847. DOI: 10.1016/j.egyr.2022.01.061.

[29] CAISO. *Renewables and emissions report: Monthly Renewable Performance Report: Apr 2021*. Folsom. CA, 2021. URL: https://www.caiso.com/market/Pages/ReportsBulletins/RenewablesReporting.aspx.

[30] Hongji Yang et al. "Exploiting the operational flexibility of a concentrated solar power plant with hydrogen production". In: *Solar Energy* 247 (2022), pp. 158–170. ISSN: 0038092X. DOI: 10.1016/j.solener.2022.10.011.

[31] Farkhondeh Jabari. *Integration of Clean and Sustainable Energy Resources and Storage in Multi-Generation Systems: Design, Modeling and Robust Optimization*. Cham: Springer International Publishing AG, 2020. ISBN: 3030424200. URL: https://ebookcentral.proquest.com/lib/kxp/detail.action?docID=6273626.

[32] Mirei Isaka. *Water Desalination Using Renewable Energy: Technology Brief*. Ed. by IEA and IRENA. 2012.

[33] Fabio Maria Aprà et al. "Overview of the Enablers and Barriers for a Wider Deployment of CSP Tower Technology in Europe". In: *Clean Technologies* 3.2 (2021), pp. 377–394. DOI: 10.3390/cleantechnol3020021.

[34] Albert Boretti, Stefania Castelletto, and Sarim Al-Zubaidy. "Concentrating solar power tower technology: present status and outlook". In: *Nonlinear Engineering* 8.1 (2019), pp. 10–31. ISSN: 2192-8010. DOI: 10.1515/nleng-2017-0171.

[35] Dario Pescador. "La Plataforma Solar de Almeria: Espejos y sol contra el cambio climatico". In: *Quo: Gigantes de la ciencia* (26.01.2023). URL: https://quo.eldiario.es/gigantes/q2302891190/visita-a-la-plataforma-solar-de-almeria/.

[36] Dennis Mackenzie. *An Overview of Heliostats and Concentrating Solar Power Tower Plants*. Ed. by National Renewable Energy Labaoratory. Golden, CO, 2022.

[37] Lorenzo Pisani et al. "Multi-tower heliostat field optimization by means of adiabatic quantum computer". In: *Solar Energy* 263 (2023), p. 111893. ISSN: 0038092X. DOI: 10.1016/j.solener.2023.111893.

[38] J. García-Ferrero et al. "Brayton technology for Concentrated Solar Power plants: Comparative analysis of central tower plants and parabolic dish farms". In: *Energy Conversion and Management* 271 (2022), p. 116312. ISSN: 01968904. DOI: 10.1016/j.enconman.2022.116312.

[39] David Barlev, Ruxandra Vidu, and Pieter Stroeve. "Innovation in concentrated solar power". In: *Solar Energy Materials and Solar Cells* 95.10 (2011), pp. 2703–2725. ISSN: 09270248. DOI: 10.1016/j.solmat.2011.05.020.

[40] Guangdong Zhu et al. "HelioCon: A roadmap for advanced heliostat technologies for concentrating solar power". In: *Solar Energy* 264 (2023), p. 111917. ISSN: 0038092X. DOI: 10.1016/j.solener.2023.111917.

[41] Zhiyong Wu et al. "An experimental and numerical study of the gap effect on wind load on heliostat". In: *Renewable Energy* 35.4 (2010), pp. 797–806. ISSN: 09601481. DOI: 10.1016/j.renene.2009.09.009.

[42] Sainath A. Waghmare and Bhalchandra P. Puranik. "Analysis of tracking characteristics of a heliostat field using a graphical ray tracing procedure". In: *e-Prime - Advances in Electrical Engineering, Electronics and Energy* 6 (2023), p. 100354. ISSN: 27726711. DOI: 10.1016/j.prime.2023.100354.

[43] WMO. *Guide to instruments and methods of observation*. Vol. 8. WMO. Geneva: World Meteorological Organization, 2014. ISBN: 978-92-63-10008-5.

[44] ICAO. *Units of measurement to be used in air and ground operations: International standards and recommended practices*. 5th ed. Annex 5 to the Convention on International Civil Aviation. Montréal: International Civil Aviation Organization, 2010. ISBN: 978-92-9231-512-2.

[45] AIAA, ed. *AIAA Guidance, Navigation, and Control Conference*. Reston, Virigina: American Institute of Aeronautics and Astronautics, 2011. ISBN: 978-1-60086-952-5. DOI: 10.2514/MGNC11.

[46] Stuart K. Grange. *Technical note: Averaging wind speeds and directions*. Auckland, New Zealand, 2014.

[47] Ding Xi-bo et al. "Measurement algorithm of two-dimensional wind vector using ultrasonic transducers". In: *TELKOMNIKA Indonesian Journal of Electrical Engineering* 11.1 (2012), pp. 517–524.

[48] MathWorks. *MATLAB: Four-quadrant inverse tangent (in degrees)*. Natick, Massachusetts, United States, 2024. URL: https://de.mathworks.com/help/matlab/ref/atan2d.html.

[49] Erik Lundtang Petersen et al. "Wind power meteorology: Part I: climate and turbulence". In: *Wind Energy* 1 (1998), pp. 25–45.

[50] Juan Felipe Vasquez Arango. "Dynamische Windlasten auf Heliostaten". PhD thesis. RWTH Aachen University, 2016. DOI: 10.18154/RWTH-2016-12225.

[51] Claës Dyrbye and Svend Ole Hansen. *Wind loads on structures*. Chichester: Wiley, 1997. ISBN: 0471956511. URL: http://www.loc.gov/catdir/description/wiley032/96030346.html.

[52] Erich J. Plate, ed. *Engineering meteorology: Fundamentals of meteorology and their application to problems in environmental and civil engineering*. Vol. 1. Studies in wind engineering and industrial aerodynamics. Amsterdam: Elsevier, 1982. ISBN: 0444419721.

[53] J. C. Kaimal et al. "Spectral characteristics of surface–layer turbulence". In: *Quarterly Journal of the Royal Meteorological Society* 98.417 (1972), pp. 563–589. ISSN: 0035-9009. DOI: 10.1002/qj.49709841707.

[54] A. M. Yaglom. "The Structure Of Atmospheric Turbulence. By J.L. L UMLEY and H. A. P ANOSKY . Interscience, 1964. 239 pp. 72s". In: *Journal of Fluid Mechanics* 32.2 (1968), pp. 415–416. ISSN: 0022-1120. DOI: 10.1017/S0022112068220815.

[55] Thomas Foken. *Angewandte Meteorologie: Mikrometeorologische Methoden*. 3. Auflage. Berlin and Heidelberg: Springer Spektrum, 2016. ISBN: 978-3-642-25524-3. DOI: 10.1007/978-3-642-25525-0. URL: http://www.springer.com/.

[56] Fernando Puente León. *Messtechnik: Grundlagen, Methoden und Anwendungen*. 11. Auflage. Berlin: Springer Vieweg, 2019. ISBN: 978-3-662-59766-8. DOI: 10.1007/978-3-662-59767-5.

[57] Hans-Rolf Tränkler and Gerhard Fischerauer. *Das Ingenieurwissen: Messtechnik*. Berlin and Heidelberg: Springer Vieweg, 2014. ISBN: 978-3-662-44029-2.

[58] Claus Weitkamp, ed. *Lidar: Range-resolved optical remote sensing of the atmosphere*. Vol. 102. Springer series in optical sciences. New York, NY: Springer, 2005. ISBN: 978-0-387-40075-4. URL: http://www.loc.gov/catdir/enhancements/fy0662/2004052454-d.html.

[59] Gary G. Gimmestad and David W. Roberts, eds. *Lidar Engineering*. Cambridge University Press, 2023. ISBN: 9781139014106. DOI: 10.1017/9781139014106.

[60] Ulla Wandinger. "Introduction to Lidar". In: *Lidar*. Ed. by Claus Weitkamp. Vol. 102. Springer series in optical sciences. New York, NY: Springer, 2005, pp. 1–18. ISBN: 978-0-387-40075-4. DOI: 10.1007/0-387-25101-4{\textunderscore}1.

[61] Lukas Pauscher et al. "An Inter-Comparison Study of Multi- and DBS Lidar Measurements in Complex Terrain". In: *Remote Sensing* 8.9 (2016), p. 782. DOI: 10.3390/rs8090782.

[62] Christina Stawiarski et al. "Scopes and Challenges of Dual-Doppler Lidar Wind Measurements—An Error Analysis". In: *Journal of Atmospheric and Oceanic Technology* 30.9 (2013), pp. 2044–2062. ISSN: 0739-0572. DOI: 10.1175/JTECH-D-12-00244.1.

[63] Rob K. Newsom et al. "Turbine–scale wind field measurements using dual–Doppler lidar". In: *Wind Energy* 18.2 (2015), pp. 219–235. DOI: 10.1002/we.1691.

[64] Lukas Deuerlein. "Implementation of a Dual-Doppler LiDAR Reconstruction Algorithm for Measuring and Evaluating the Wind Field above a Heliostat Field". Master Thesis. Kassel: Groningen, 30.11.2023.

[65] CIEMAT. *Plataforma Solar de Almeria: Overview*. Tabernas, 2023. URL: https://www.psa.es/en/gen/index.php.

[66] CIEMAT. *Central Receiver Facilities: CESA*. Tabernas, 2024. URL: https://www.psa.es/en/facilities/central_receiver/cesa1.php.

[67] Google Earth. *"Plataforma Solar de Almeria"*. 2024. URL: https://earth.google.com/web/@37.09502214,-2.3579511,502.09197006a,1680.11821868d,35y,0h,0t,0r.

[68] WindSonic. *Datasheet: 1405-PK-021D*. Ed. by Gill Instruments. URL: https://gillinstruments.com/wp-content/uploads/2022/08/WindSonic-1405-027-iss-8.pdf.

[69] WindMaster. *Datasheet: 1590-PK-020/W*. Ed. by Gill Instruments. URL: https://gillinstruments.com/wp-%20content/uploads/2022/08/WindMaster-iss7-Datasheet.pdf.

[70] Vaisala. *Wind Cube Datasheet: 200S*. URL: https://www.vaisala.com/sites/default/files/documents/WEA-MET-WindCube-Scan-Lidar-Product-Spotlight-B212058EN-A.pdf.

[71] Campbell Scientific. *CR1000X: Measurement and Control Datalogger: Product Manual*. 2024.

[72] IEC 61400-1. *Wind energy generation systems - Part 1: Design requirements*. 2019.

[73] CIEMAT. *Parabolic Trough Facilities: DISS*. Tabernas, 2022. URL: https://www.psa.es/en/facilities/parabolic_trough/diss.php.

List of Figures

List of Tables

A Appendix

Overview of the Matlab-Codes Generated and Used

The following codes have been implemented using Matlab.

- correction of the wind direction calculation
- validation of the preprocessing as stated in the thesis
- adjusting of and expanding on algorithms for the calculation, evaluation and visualisation of wind pattern (wind speed, wind gust, turbulence intensity, diurnal pattern, frequency distributions, wind roses, 6h-moving averages, comparison of single wind components among others)
- preprocessing and processing of the tracking data the tracking data
- validation of the processed data
- development of a method to calculate the heliostats target area and its implementation in form of algorithms
- development of a method ot establish the heliostats' impact on wind parameters and its implementaion in form of algorithms
- visualisation of the evaluated data
- creating a scaled-down 2D plot of the CESA-I heliostat field, adjustable to have data assigned to it
- processing and evaluating the LiDAR data
- writing codes to compare LiDAR and anemometer data

The Matlab code created in the context of the thesis is submitted electronical on a storage device.

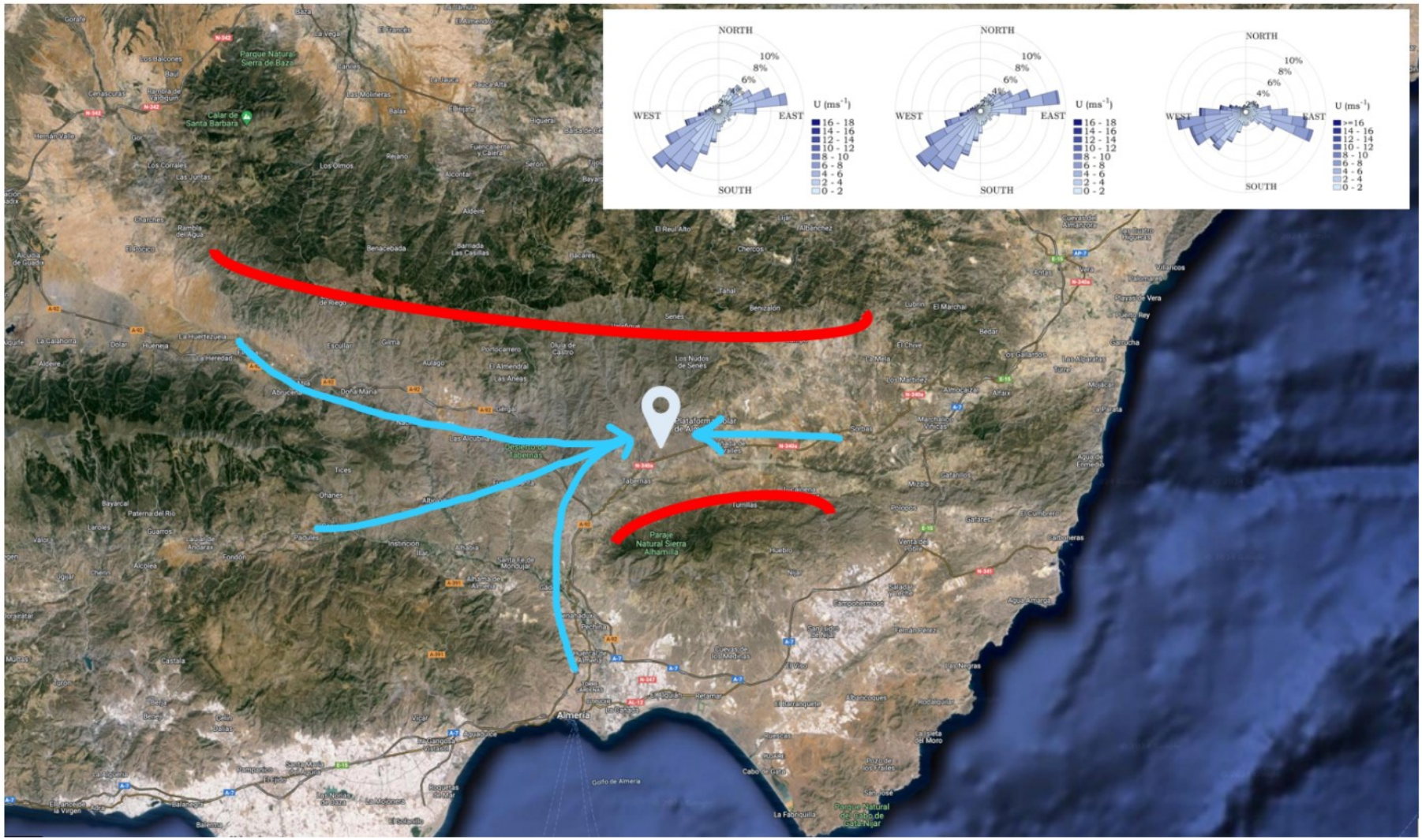

Fig. A.1: Overview of the topology surrounding the Plataforma Solar de Almeria. Mountains in the north and south of the test site CESA-I block the wind directions, leaving the south-western and eastern tunnel for main wind directions. Picture adapted from [67].

B Turbulence Spectra Plots

The following plots of the turbulence spectra are added to enable a more detailed few of the graphs without disturbing the flow of the thesis. The figures can be divided into following categories.

Graph 1 + 2: **Validation of the horizontal wind components similarity**
Turbulence spectra of all horizontal wind components at all wind masts. Differentiation between 4 m and 7 m height.

Graph 3 – 7: **General Depiction with Kaimal/Panowski**
Averaged turbulence spectra at wind mast 1 and wind mast 4. Differentiation between the three heights (4 m, 7 m and 10 m). and the wind component (S_U and S_w).

Graph 8 + 9: **Vertical Influence Analysis**
Turbulence spectra of all at wind mast 1 in all three heights (4 m, 7 m and 10 m). Differentiation between vertical and horizontal turbulence spectra S_U and S_w.

Graph 10 – 13: **Horizontal Influence Analysis**
Turbulence spectra at wind mast 1 and wind mast 4 in 7 m height. Differentiation between vertical and horizontal turbulence spectra S_U and S_w.

Graph 13 – 16: **Tracking Influence Analysis**
Turbulence spectra at wind mast 1 and wind mast 4 in 7 m height. Differentiation between vertical and horizontal turbulence spectra and the tracking status of the heliostat field.

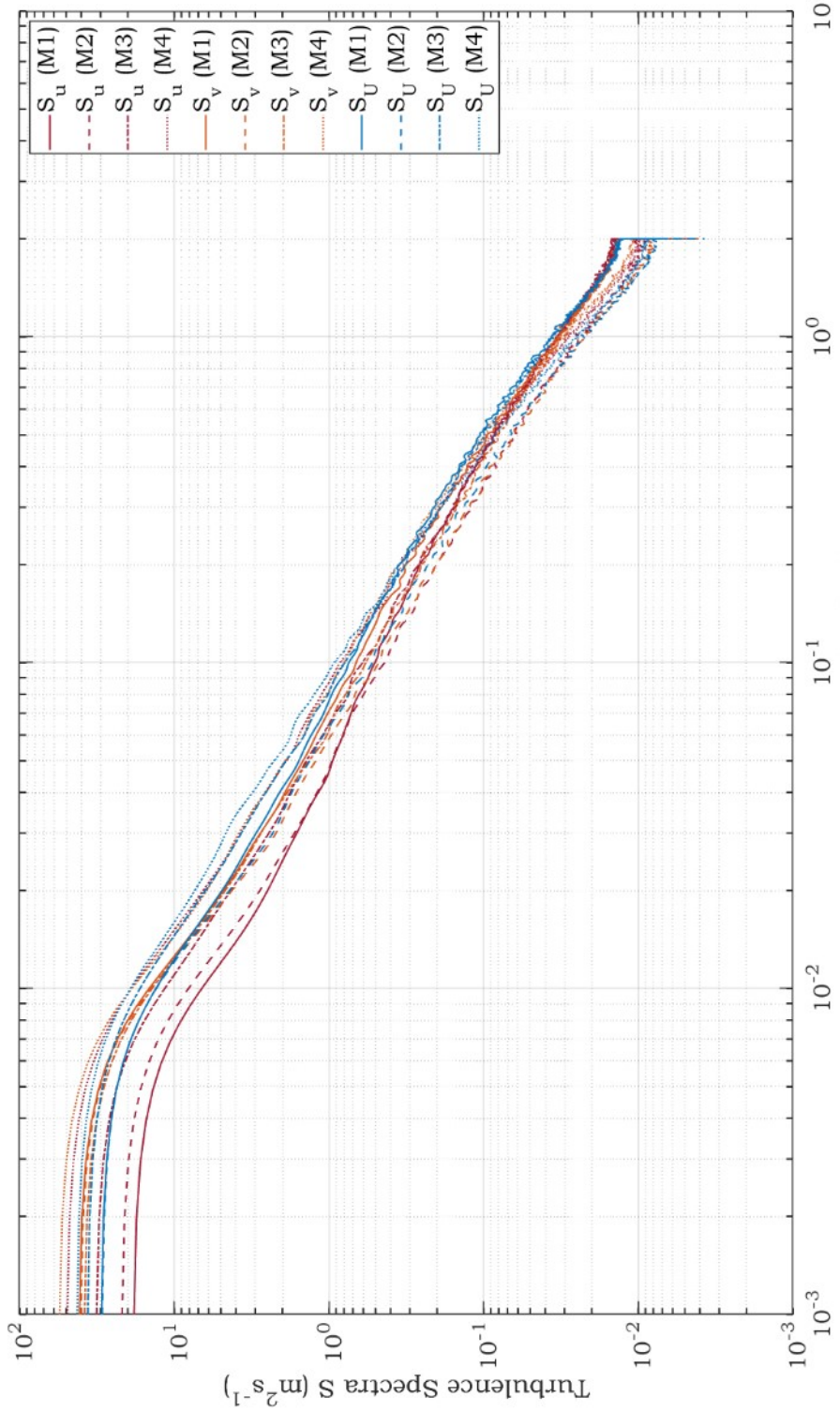

Fig. B.2: Averaged Turbulence Spectra S for the horizontal wind components S_u and S_v as well as the combined horizontal wind component S_U in 4 m height for the measured period of 2023-02-15 to 2023-05-31.

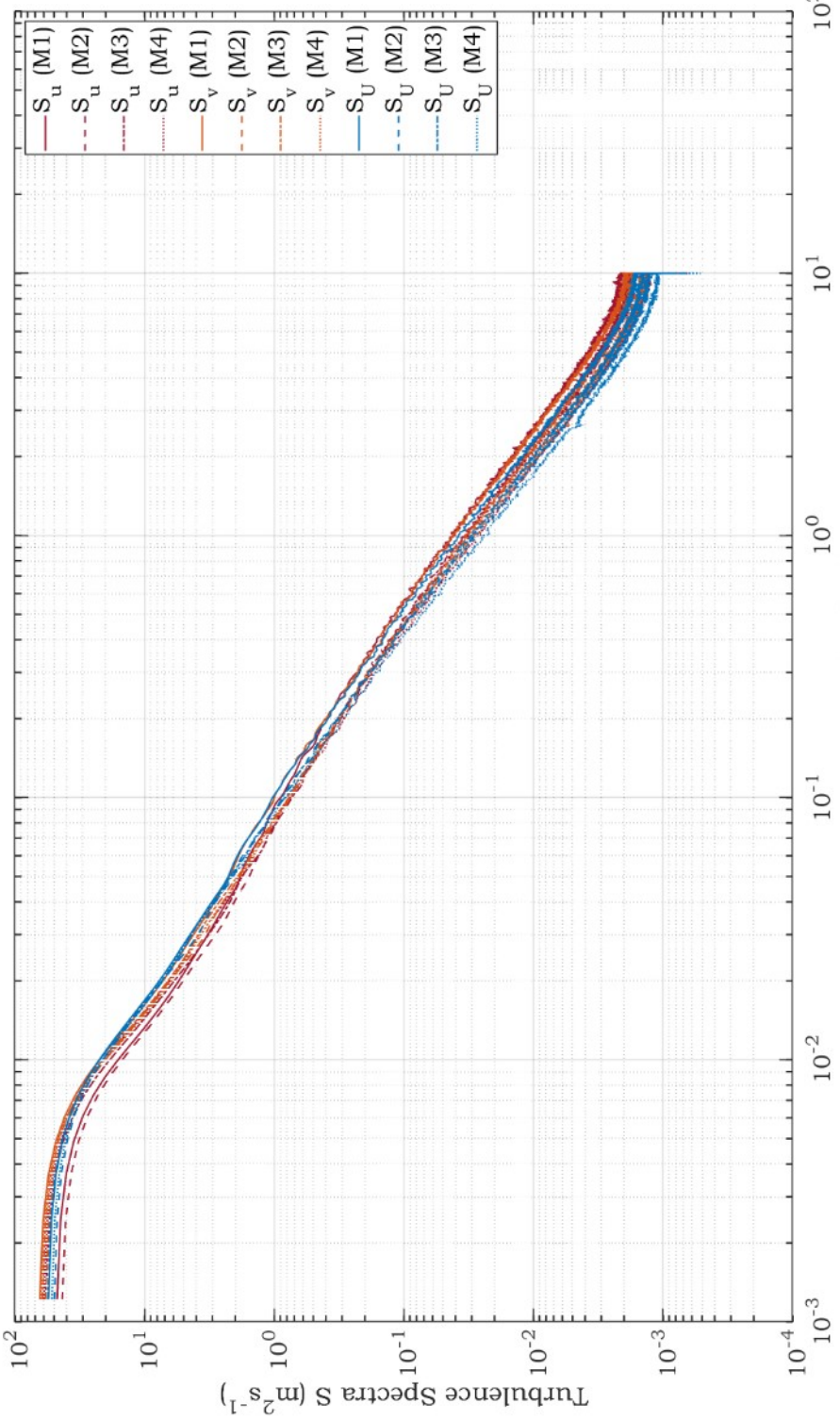

Fig. B.3: Averaged Turbulence Spectra S for the horizontal wind components S_u and S_v as well as the combined horizontal wind component S_U in 7 m height for the measured period of 2023-02-15 to 2023-05-31.

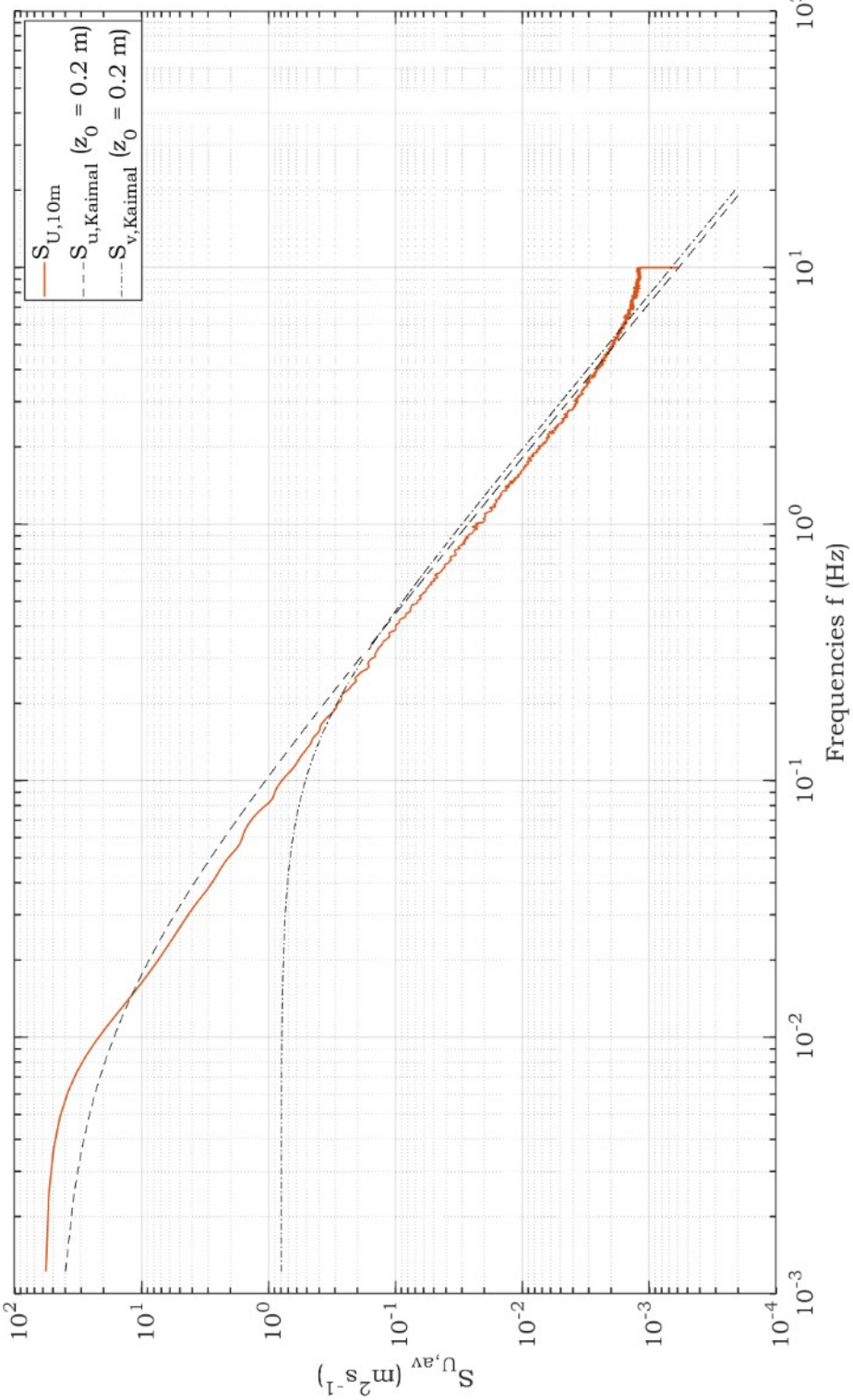

Fig. B.4: Averaged Turbulence Spectra S for the combined horizontal wind component S_U in 10 m height for the measured period of 2023-02-15 to 2023-05-31. Figure 4.7a enlarged.

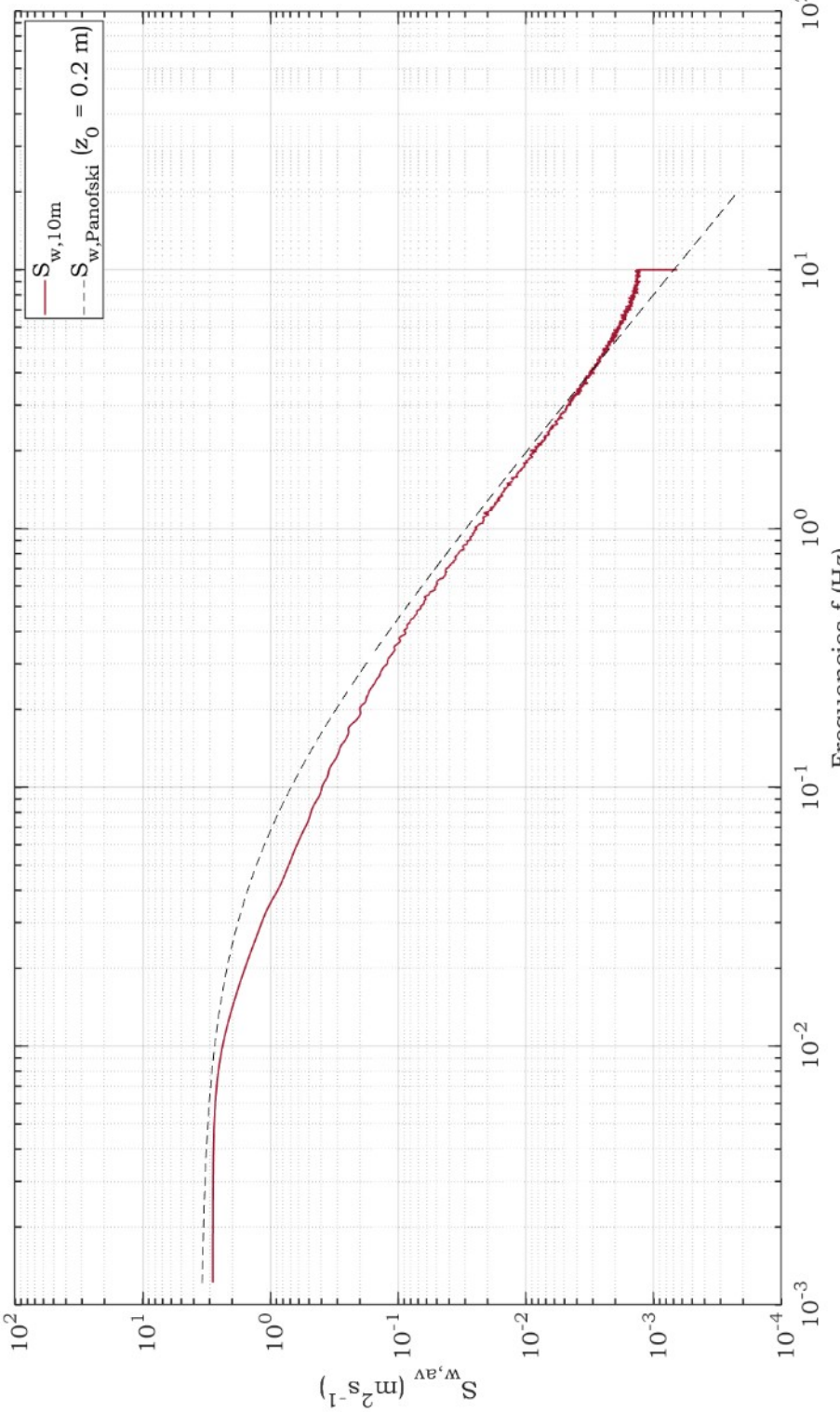

Fig. B.5: Averaged Turbulence Spectra S for the vertical wind component S_w in 10 m height for the measured period of 2023-02-15 to 2023-05-31. Figure 4.7b enlarged.

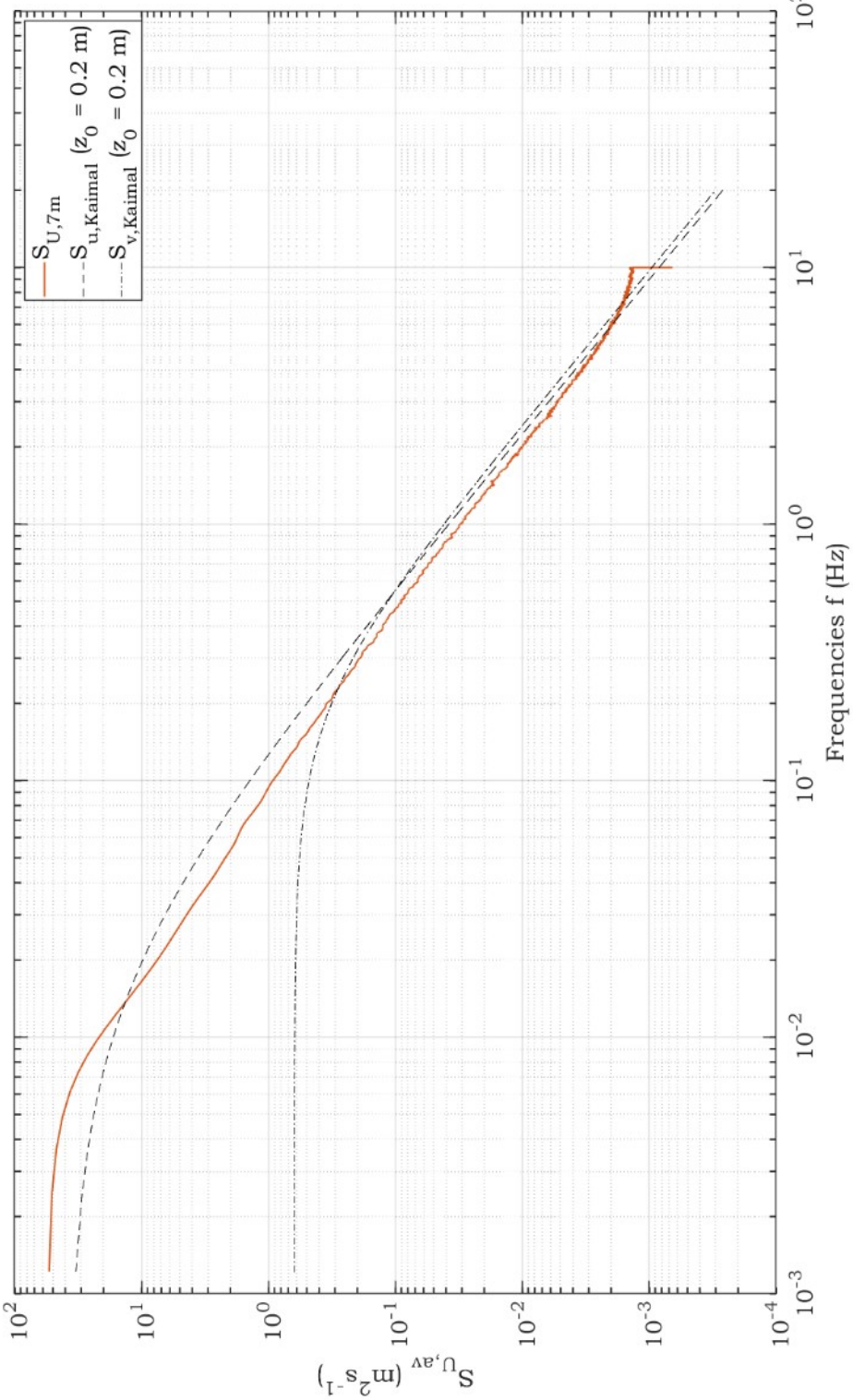

Fig. B.6: Averaged Turbulence Spectra S for the combined horizontal wind component S_U in 7 m height for the measured period of 2023-02-15 to 2023-05-31. Figure 4.7c enlarged.

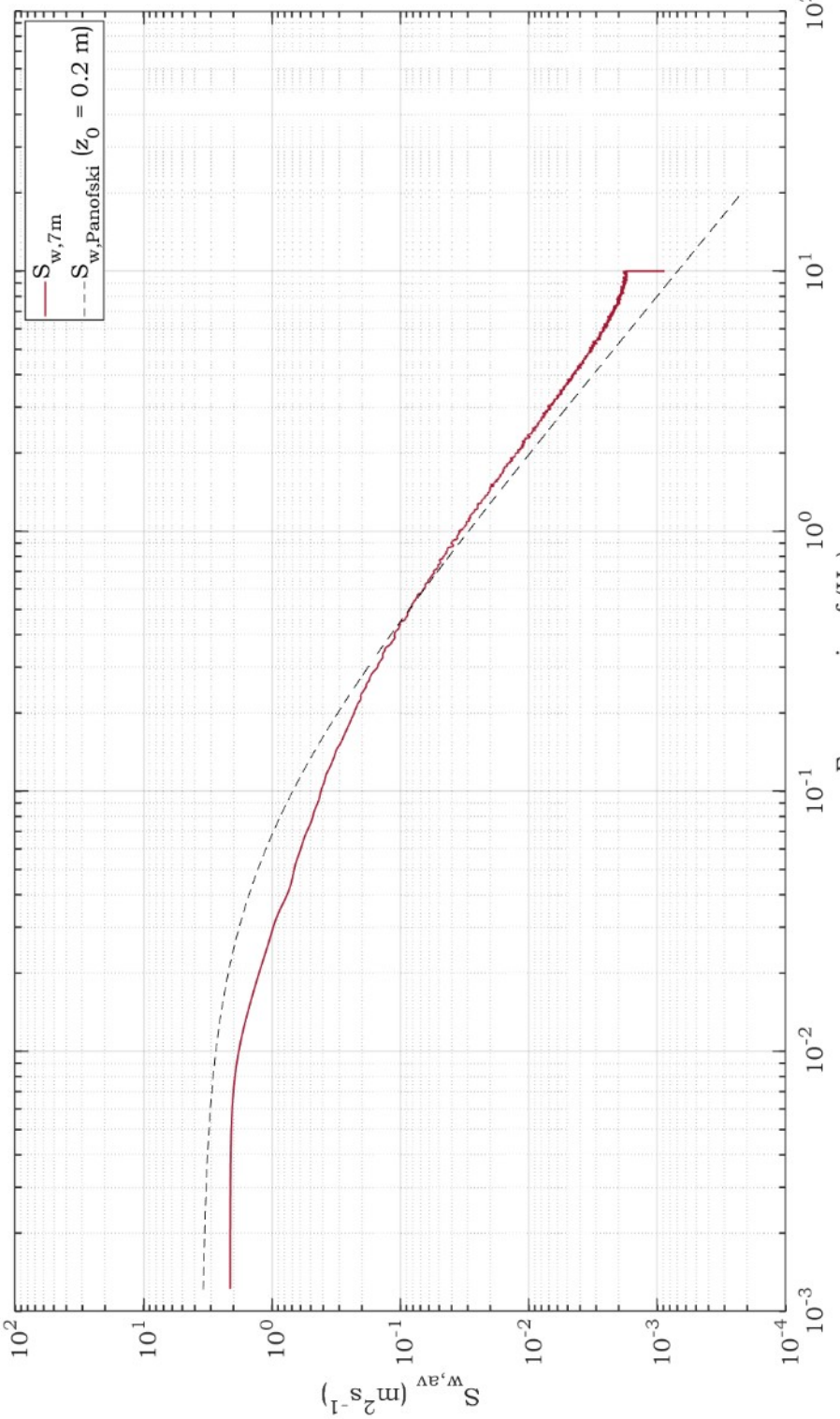

Fig. B.7: Averaged Turbulence Spectra S for the vertical wind component S_w in 7 m height for the measured period of 2023-02-15 to 2023-05-31. Figure 4.7d enlarged.

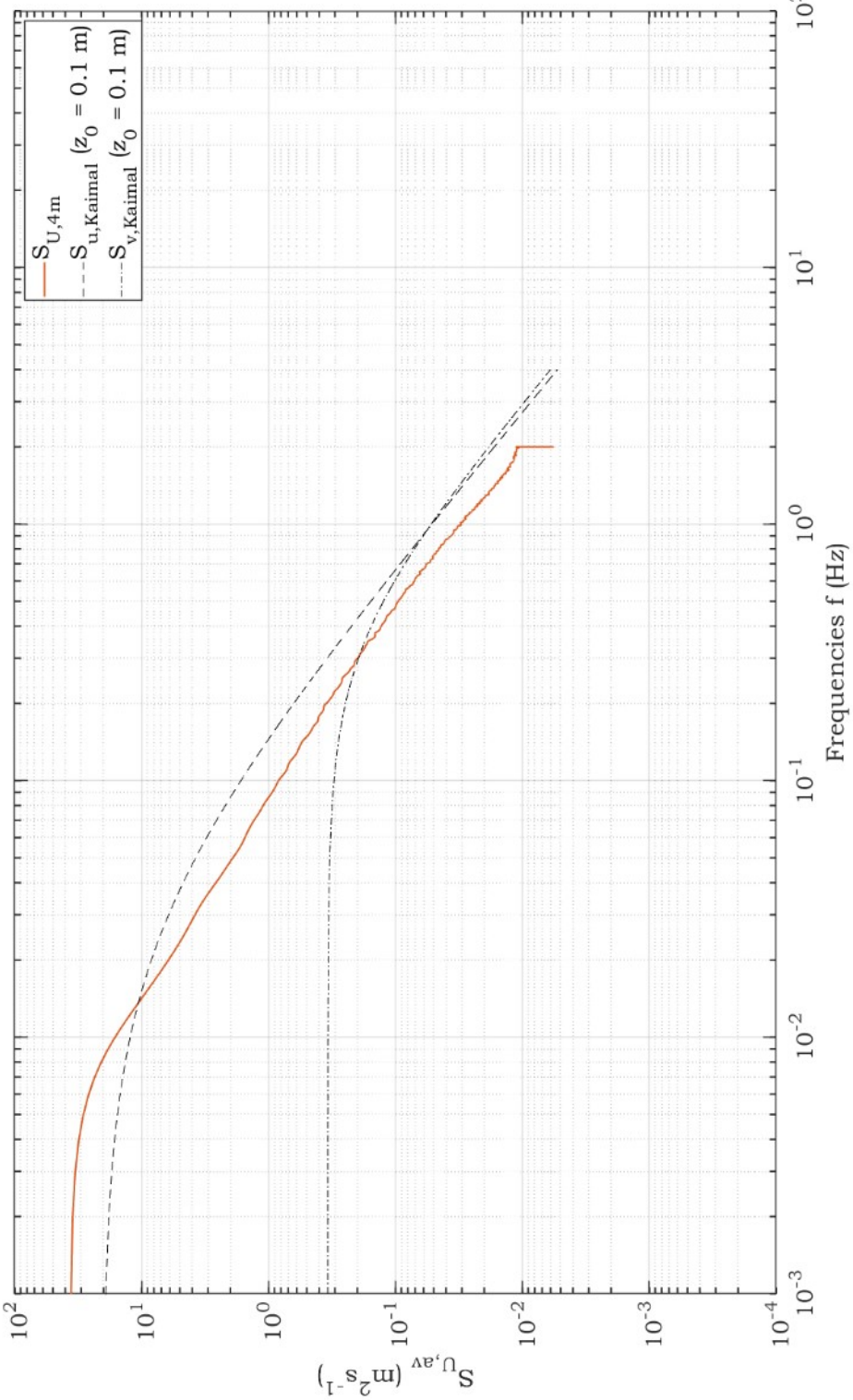

Fig. B.8: Averaged Turbulence Spectra S for the combined horizontal wind component S_U in 4 m height for the measured period of 2023-02-15 to 2023-05-31. Figure 4.7e enlarged.

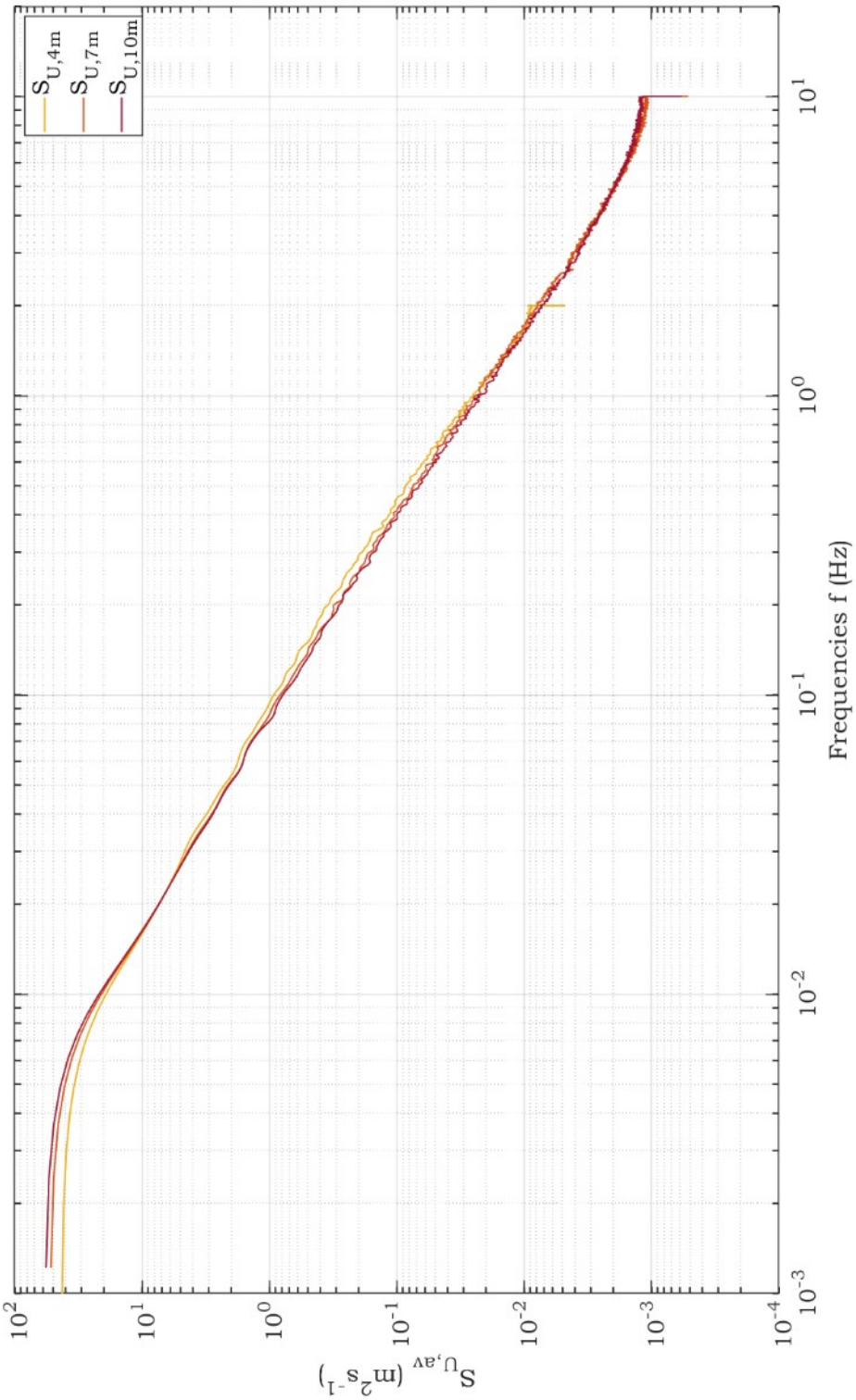

Fig. B.9: Averaged Turbulence Spectra S for the combined horizontal wind component S_U in different heights 4 m, 7 m and 10 m for the measured period of 2023-02-15 to 2023-05-31. Figure 4.8a enlarged.

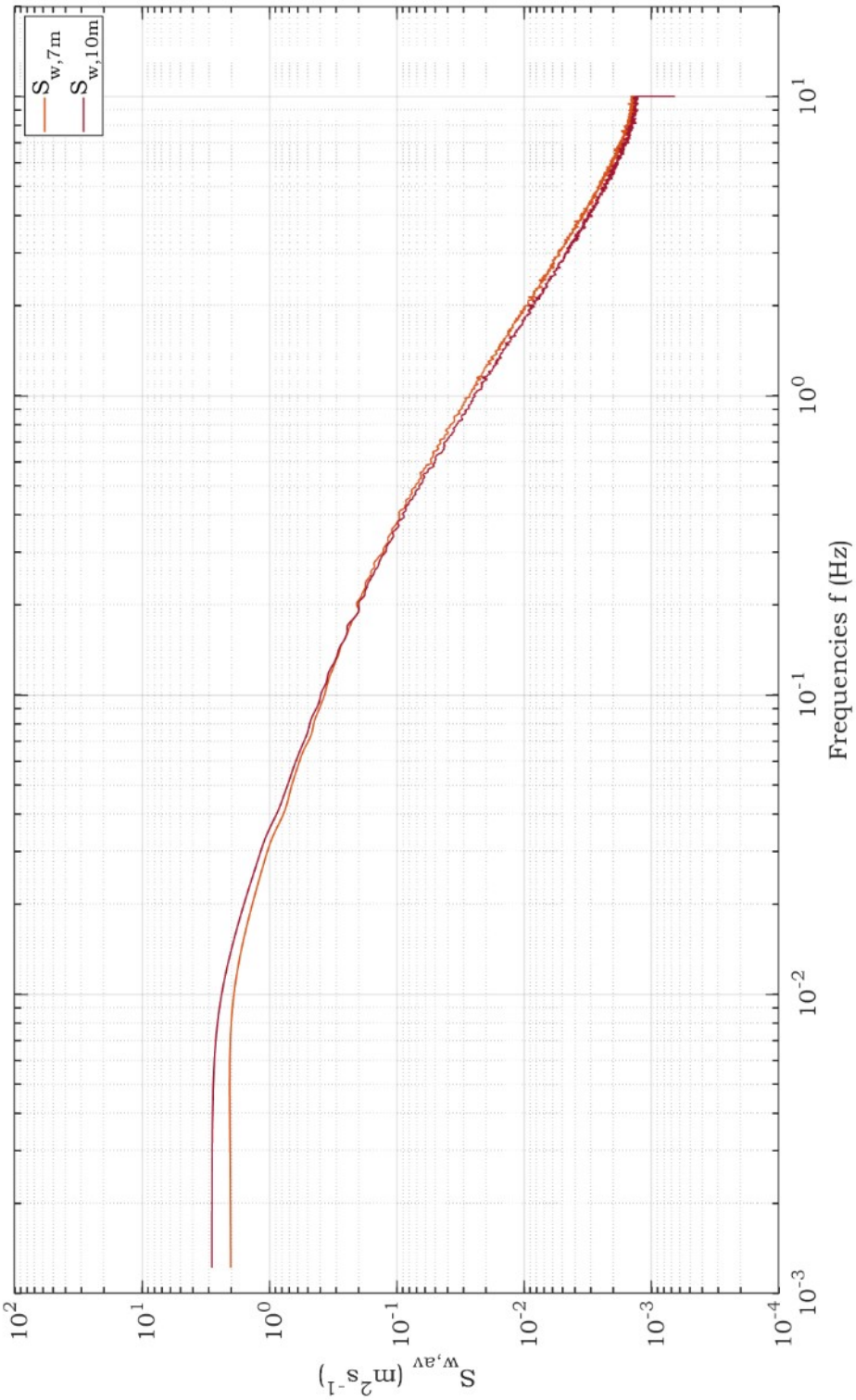

Fig. B.10: Averaged Turbulence Spectra S for the vertical component S_w in different heights 4 m, 7 m and 10 m for the measured period of 2023-02-15 to 2023-05-31. Figure 4.8b enlarged.

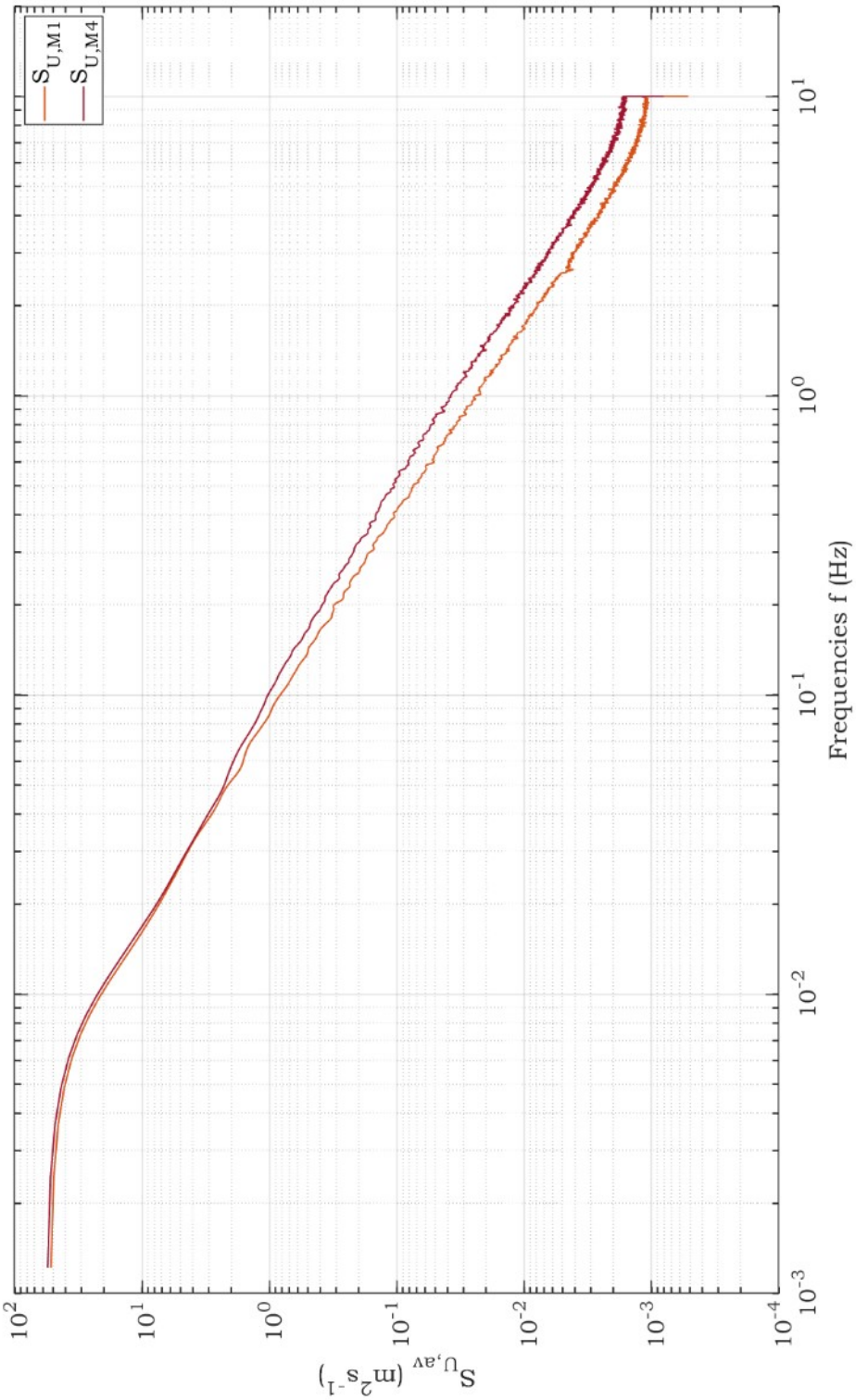

Fig. B.11: Averaged Turbulence Spectra S at wind mast 1 and wind mast 4 for the combined horizontal wind component S_U in 7 m height for the measured period of 2023-02-15 to 2023-05-31. Figure 4.14a enlarged.

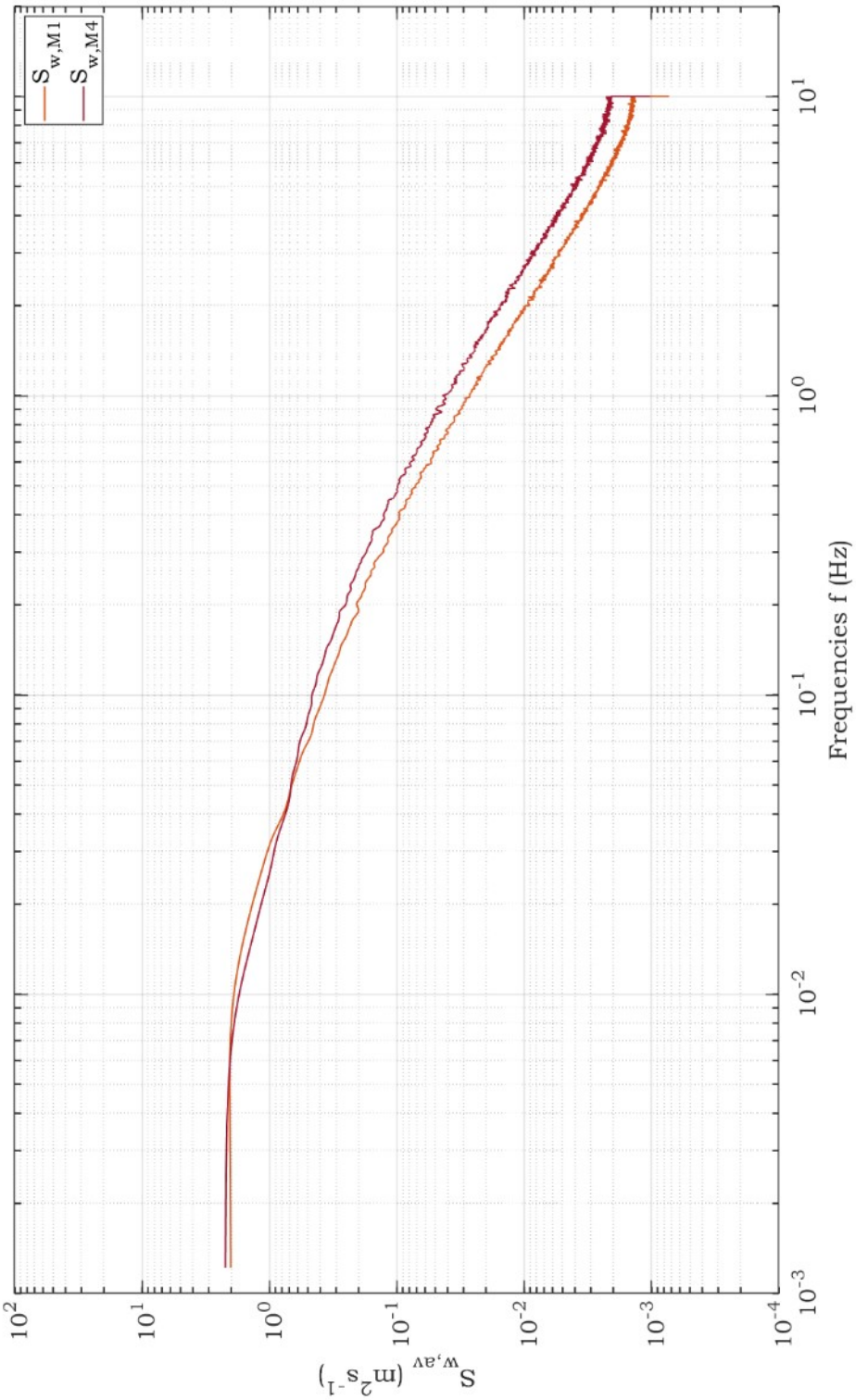

Fig. B.12: Averaged Turbulence Spectra S at wind mast 1 and wind mast 4 for the vertical wind component S_w 7 m height for the measured period of 2023-02-15 to 2023-05-31.
Figure 4.14b enlarged.

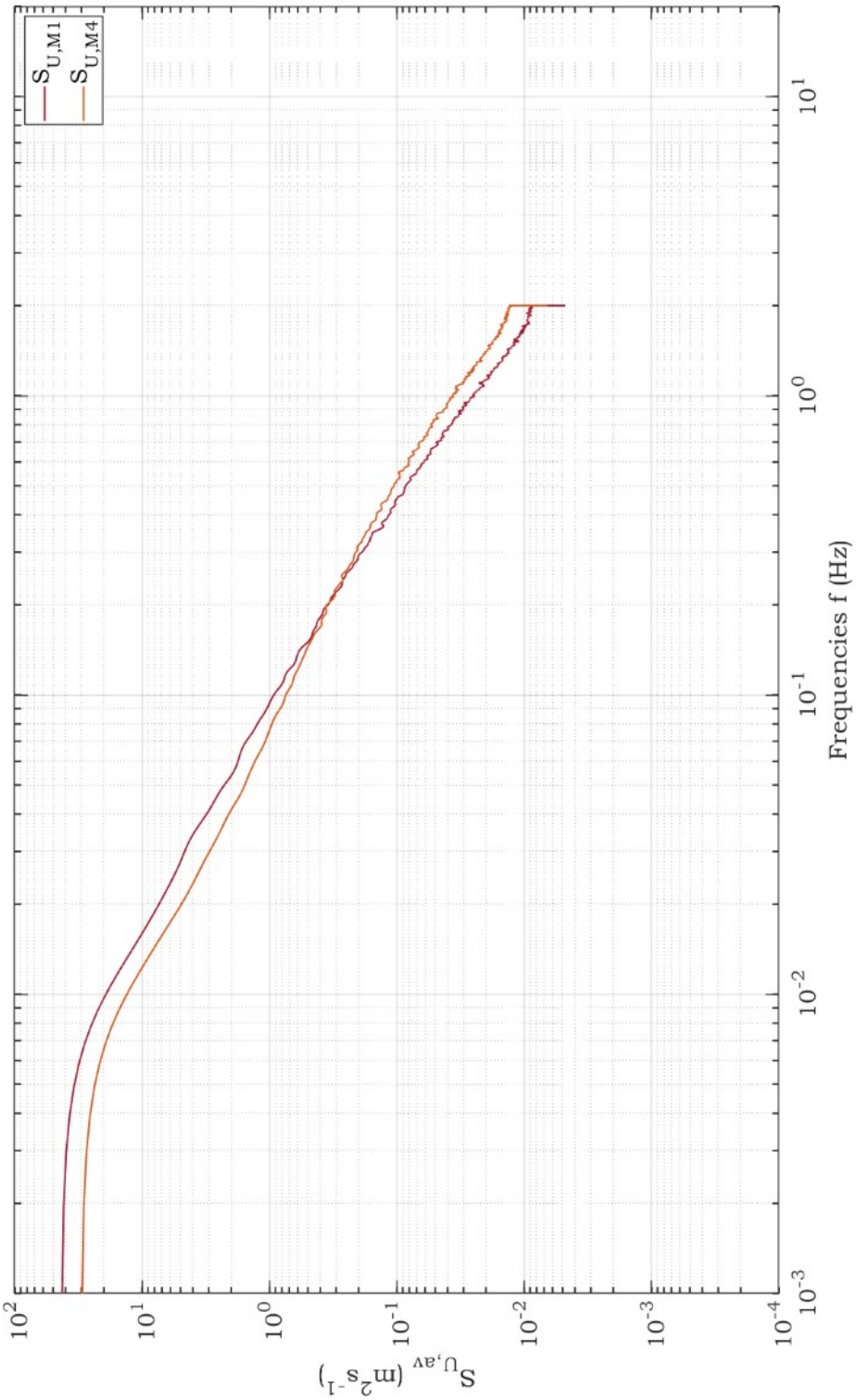

Fig. B.13: Averaged Turbulence Spectra S at wind mast 1 and wind mast 4 for the combined horizontal wind component S_U in 4 m height for the measured period of 2023-02-15 to 2023-05-31. Figure 4.14c enlarged.

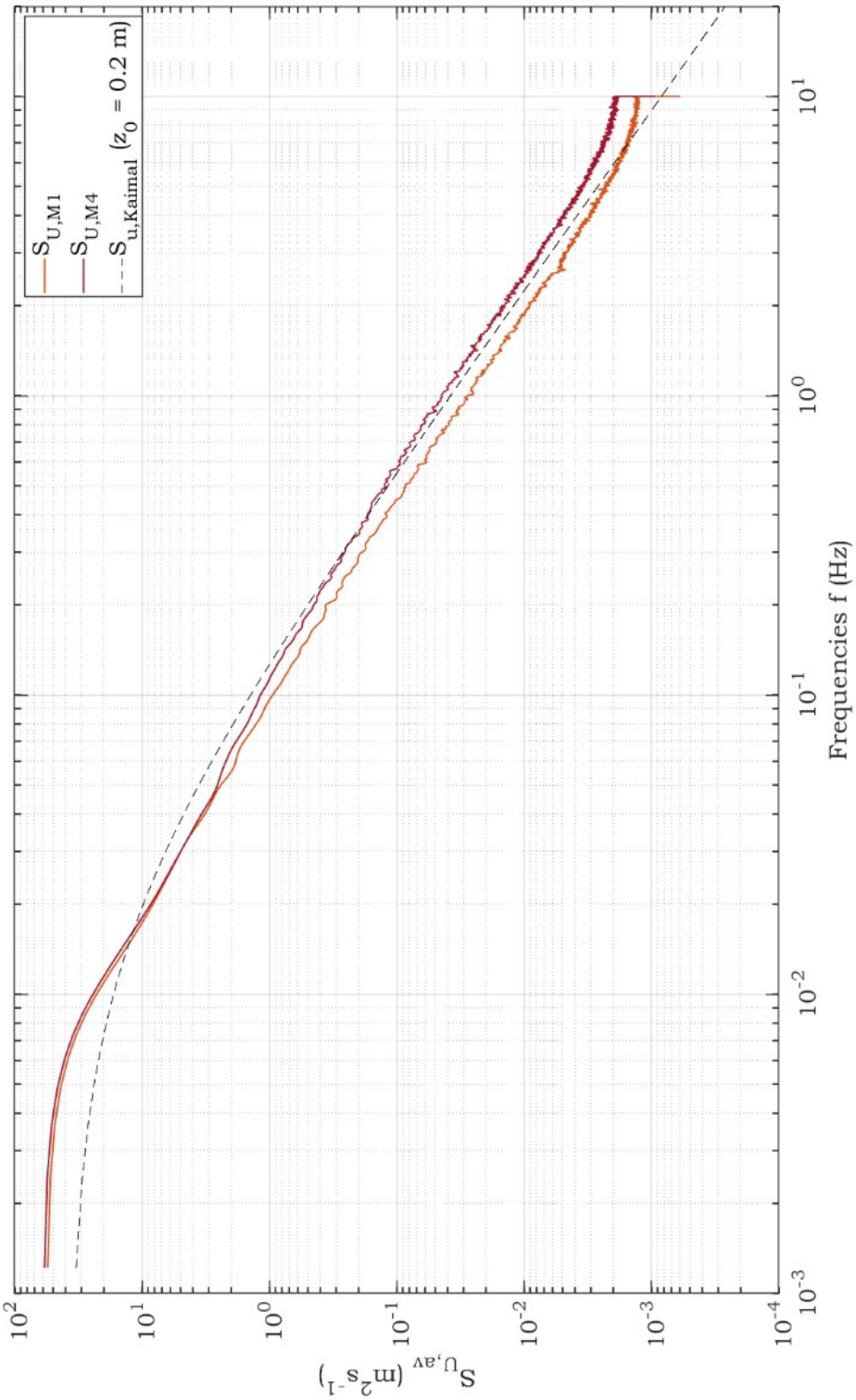

Fig. B.14: Averaged Turbulence Spectra S at wind mast 1 and wind mast 4 in 7 m height for the combined horizontal wind component S_U for times with tracked heliostat field during the measured period of 2023-02-15 to 2023-05-31. Figure 4.16a enlarged.

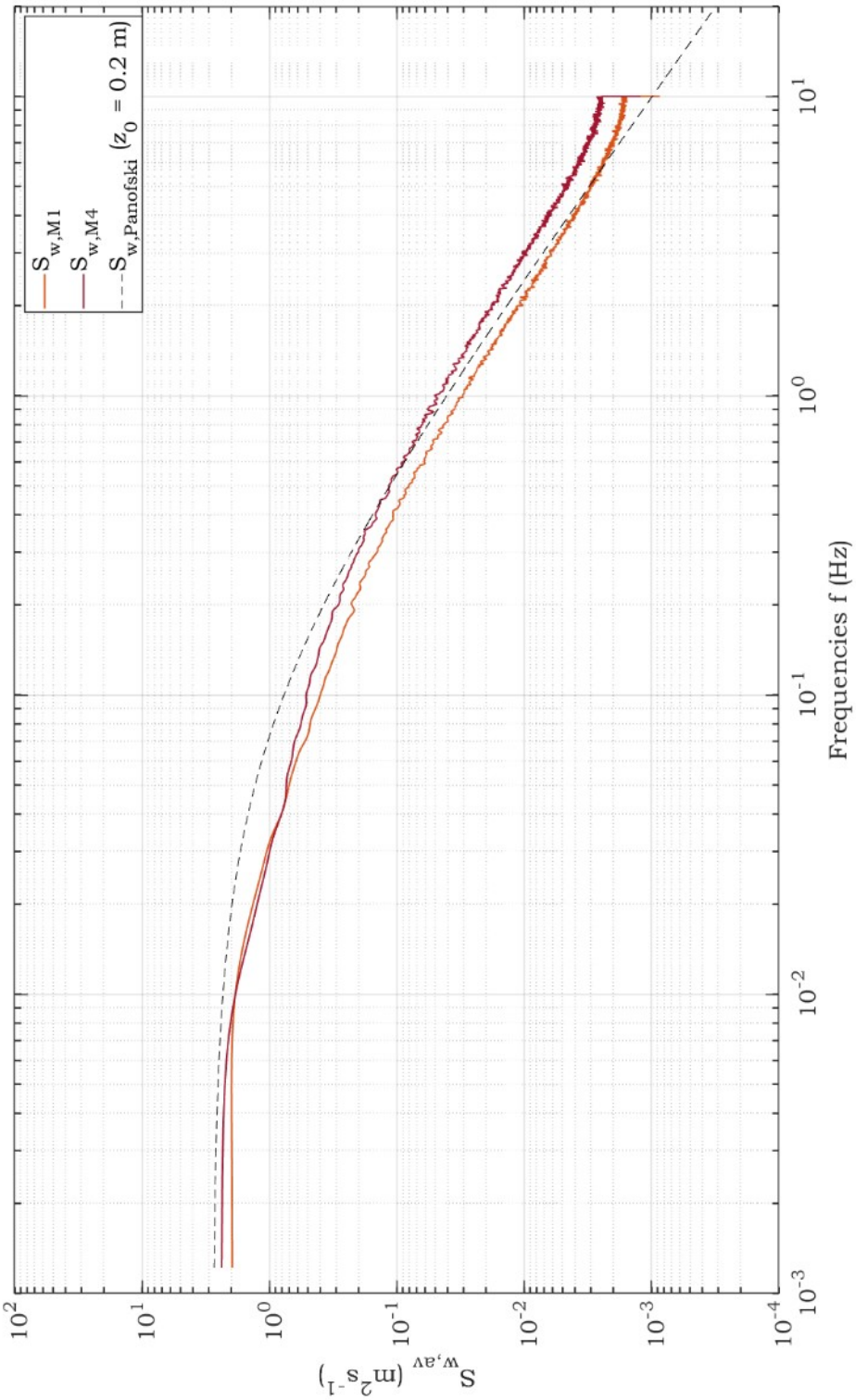

Fig. B.15: Averaged Turbulence Spectra S at wind mast 1 and wind mast 4 in 7 m height for the vertical wind component S_w for times with tracked heliostat field during the measured period of 2023-02-15 to 2023-05-31. Figure 4.16b enlarged.

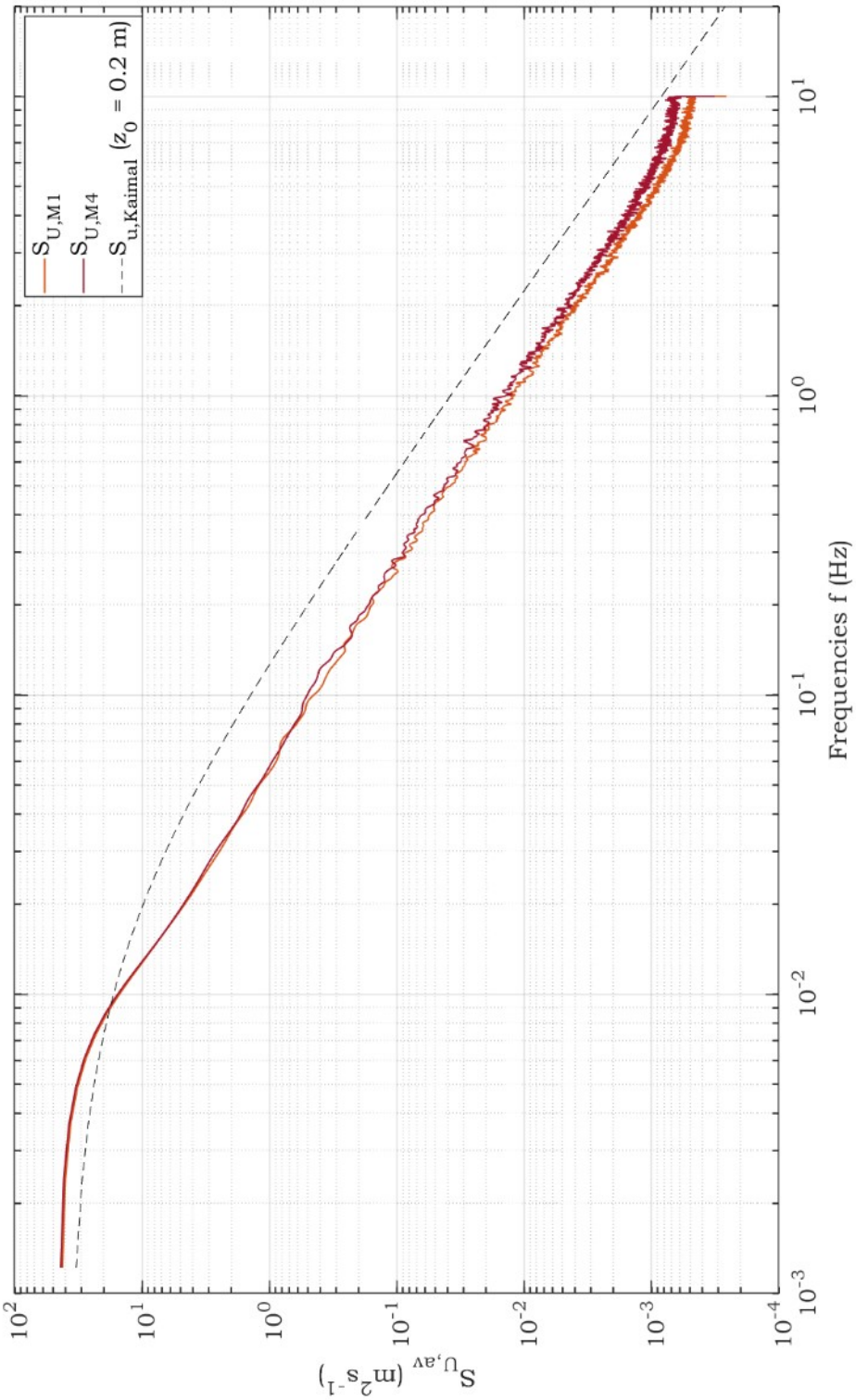

Fig. B.16: Averaged Turbulence Spectra S at wind mast 1 and wind mast 4 in 7 m height for the combined horizontal wind component S_U for times with heliostat field in stow during the measured period of 2023-02-15 to 2023-05-31. Figure 4.16c enlarged.

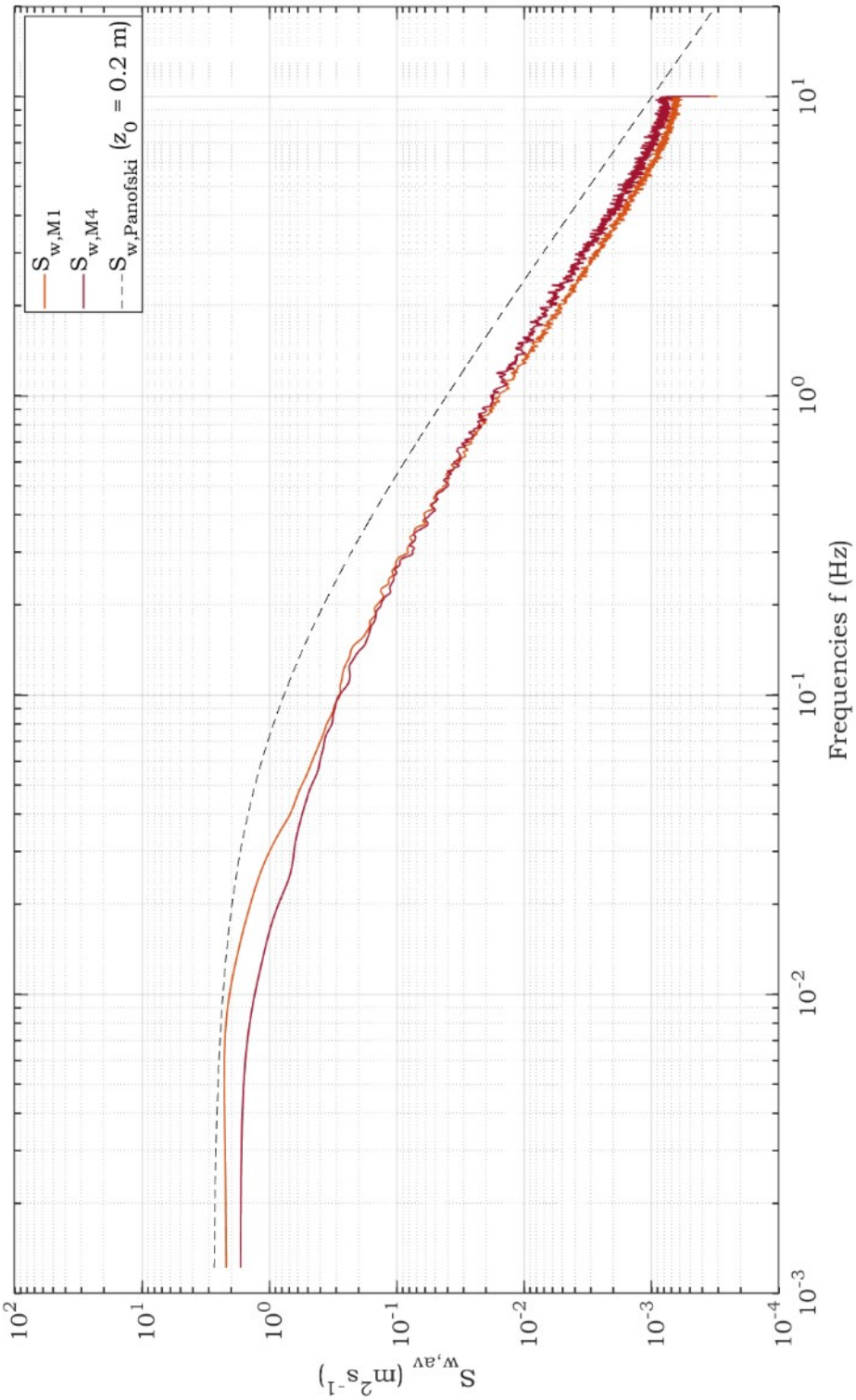

Fig. B.17: Averaged Turbulence Spectra S at wind mast 1 and wind mast 4 in 7 m height for the vertical wind component S_w for times with heliostat field in stow during the measured period of 2023-02-15 to 2023-05-31. Figure 4.16d enlarged.